Nano particle cleaning with a low pressure jet flow

Blom, S.

Award date:
2019

Nano Particle Cleaning with a Low Pressure Jet Flow

Public Version

Report on a Master's research project carried out at ASML,
March 2018 - December 2018

Author
S. Blom

Report Number
R-1954-A

Supervisor ASML
S.F. De Vries

Supervisor TU/e
G.J.F. Van Heijst

January 18, 2019

Preface

This report is the result of my graduation project at ASML (Advanced Semiconductor Materials Lithography), the final stage of my Master Applied Physics at the Eindhoven University of Technology (TU/e). I choose to perform a fluid dynamics related research in a progressive technical company. Through Professor GertJan van Heijst his business network, we found a suitable project at ASML.

ASML is the world's leading provider of lithography systems for the semiconductor industry. In 1965, Gordon Moore predicted that the number of transistors in a dense integrated circuit doubles about every two years. In order to increase the number of transistors, they have to become smaller and smaller. Today, structures of 13 nm can be printed. Shrinking these structures more and more drives technology to the limit. With over 20.000 employees and more than 80 facilities worldwide, ASML is gigantic and still growing. Because of this extensiveness in employees, facilities, and developments ASML focusses on a close cooperation: internally, and with the customers and suppliers worldwide.

Building on Moore's law, Extreme Ultra Violet (EUV) light is currently used in the newest machines of ASML. However, this EUV light and the extremely small scales that have to be printed result in many practical issues. EUV light is absorbed by almost everything, so the light has to travel through vacuum and mirrors are applied to focus the light. Furthermore, the smallest particles in the scanner like dust and skin flakes can cause significant distortions. During the research project, I have analyzed how cleaning the most critical area in the scanner could eliminate these small particles. During this research various low-pressure jet flows are studied to clean this critical environment in the most effective way. These jets are simulated using StarCCM+, and during this research I learned to work with this software and to critically assess the results. The problems I faced had mostly to do with the non-availability of research, and the hard imagination in the low-pressure regime. Which physical laws can be applied in this regime? Are the simulation results correct? are questions that I have asked myself continuously. Discussing my assumptions and simulation results with experts, made it possible to tackle most of the problems reflected in my conclusions and recommendations.

During this research I learned a lot about simulating flows and the physics in the low-pressure regime. In addition, I have experienced how physics is applied in the field, and how it is to work in a progressive company like ASML. For that, I want to thank everyone who made it possible to do my graduation project within ASML, and helped me during the research. Especially, I want to thank Sjoerd de Vries, who has been my supervisor at ASML and professor GertJan van Heijst in his role as the supervisor on behalf of TU/e. Furthermore, I want to thank Pieter Aarts for the general guidance during my studies and my graduation project. Finally, a warm thank you goes to my family and girlfriend who supported me unconditionally during the course of my study.

Abstract

With ASML's Extreme Ultra Violet (EUV) photolithographic systems chip-patterns with a resolution of 13 nm are printed. Extremely small particles can cause problems in the printing process. The systems use light to transfer an geometric pattern from a photomask, which is called the reticle, to a light-sensitive chemical resist. So it is critical to keep the reticle and the reticle environment clean from (small) particles. In this report the dynamics of a jet flow parallel to a surface is studied to better understand the cleaning of the reticle environment. To release small particles from a surface, slip flow is needed, which is present at low pressures. Jets that are formed at different pressures and flowrates are studied in this report. In the low-pressure regime many interesting flow features are observed. Free molecular, and slip flow will be discussed to simulate the flows and to describe the drag force on small particles. As a result of higher pressures, locally the transition from laminar to turbulent flow is observed and discussed. The most important conclusion from this research is that the best particle release using a low-pressure parallel jet is not achieved at extreme low pressures, as was originally assumed at ASML. Local turbulence, existing at higher pressures, in combination with slip flow is the key to achieve optimum particle release.

Contents

Chapter 1

Introduction

In ASML's newest photolithographic systems (NXE) Extreme Ultra Violet (EUV) light is used to print chip-patterns with a resolution of 13 nm. These features are so small, that even the smallest particles (like dust, skin flakes, or metals) can cause problems in the printing process. Since EUV light is absorbed very easily, the light should travel through vacuum, and mirrors are used to focus the light. To minimize the number of defects, the vacuum part of the machine should be as clean as possible. This is done by building the machine with clean parts. However, some particles will always be present. When these particles reach the critical surfaces, like the wafer (on which the chip is printed) or the reticle (consists the printed pattern) this results in defective chips.

A particle on the reticle results in a defect in every field on every wafer. Every printed chip will not work and the reticle should be cleaned. The loss in yield of manufactured chips can cost the customer millions. This report focuses on the prevention of reticle defects by flushing. Flushing is a cleaning action which is used to clean the critical area around the reticle after the scanner has been assembled, such that the added contamination during assembly can be removed. It can also be used as a corrective action when defectivity issues arise or as a regularly repeated cleaning action.

To protect the reticle during production from contamination, it has been proposed to use a low-pressure H_2 flow that is created using a nozzle below the reticle. (In section 3.1 the area of interest is discussed in more detail, reticle = critical surface, REMA blades = contaminated surface). This is the mean reason of the parallel orientation of the nozzle with respect to the reticle. This nozzle may be used to flush the reticle environment between production as well. For this purpose XCDA (eXtreme Clean Dry Air) and a sacrificial reticle may be used. Analyzing the particles on the sacrificial reticle before and after the flush can tell how effective the flush has been. For the reticle defectivity the REMA blades are of special interest, because these blades are the closest surfaces to the reticle. Furthermore, the blades move through the EUV light and plasma during production, so loose particles on the blades can be released and result in reticle defects.

Based on the Rock'n'roll model (Henry and Minier, 2014) (Figure 1.1) it is assumed that if a particle under influence of the gas flow starts moving, it can be released by a collision with a large asperity. The drag force moment should be higher than the adhesion force moment for the particle to start moving.

The adhesion force has a high variability and the distribution of adhesion forces of the particles on the surface is very difficult to predict. As explained in section 2.4, it depends on the particle and surface properties and the specific configuration of the particle on the surface. It is also affected by very small scale roughness parameters that are typically unknown. Furthermore, the release is also influenced by the variations in moments. Flushing tests have shown that particles down to 50 nm are being released. The particles that are being released are only a small portion of the particles actually present, so only the most loosely attached particles are released. These particles are also the most likely to cause defects during operation. In Figure 1.2 a sketch of a

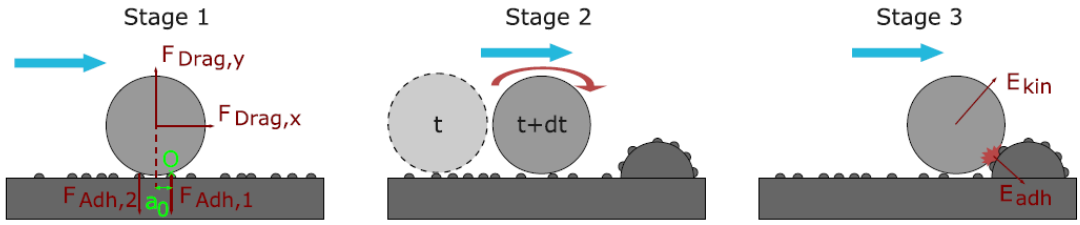

(a) Set into motion (b) Rolling or sliding (c) Rocking

Figure 1.1: *(a) particle is set in motion as result of the force moments. (b) particle is moving and can gain or lose kinetic energy as result of the varying adhesion and drag forces along the particles trajectory. (c) particle is colliding with a large asperity and is released if the instantaneous longitudinal kinetic energy is higher than the adhesion potential energy. (picture and explanation from Henry and Minier (2014))*

typical adhesion force distribution is shown. The goal is to release particles upto a higher adhesion force than the particles that can be released during production.

The main focus of this study will be the drag force as result of the low-pressure gas flow. Initially the largest drag force on small particles at a surface was expected at very low pressures, because of the high wall velocities in the low-pressure regime. Injecting gas with a high flowrate at very low pressure seems a logical way to release the most particles. As a result of the injected gas the pressure will increase, which is assumed to be positive for the transport of particles. Then the flowrate is decreased and the pressure will drop again. These steps may be repeated, which results in the pulsating flush sequence that has been proposed as the most efficient.

The main goal of this research is to understand how the best particle release using a low-pressure gas flow can be obtained. Needed are: the gas flow solutions for different cases, and an expression to couple these results to a drag force on particles on a wall. As a starting point a flush sequence as proposed above (varying background pressure and flowrate) is simplified and simulated transiently to get more in depth insights in the flushing performance. From the results preliminary conclusions are derived and these are used as input to optimize the way of flushing.

In this research the most important dimensionless quantities are the Knudsen number and the Reynolds number. To determine the flow regime, continuum, free molecular or in between, the Knudsen number is calculated as $Kn = \frac{\lambda}{L}$, where λ is the mean free path of the gas molecules, and L the critical length scale of the geometry. The mean free path is calculated as $\lambda = \frac{k_B T}{\sqrt{2}\pi P \sigma^2}$, with k_B the Boltzmann constant, T the temperature, P the absolute pressure, and σ the collision diameter, which is 362.1 pm for XCDA. In this research two Knudsen numbers are needed: one for the geometry (Figure 3.1), and one for the particles. Following Lockerby et al. (2005) the channel

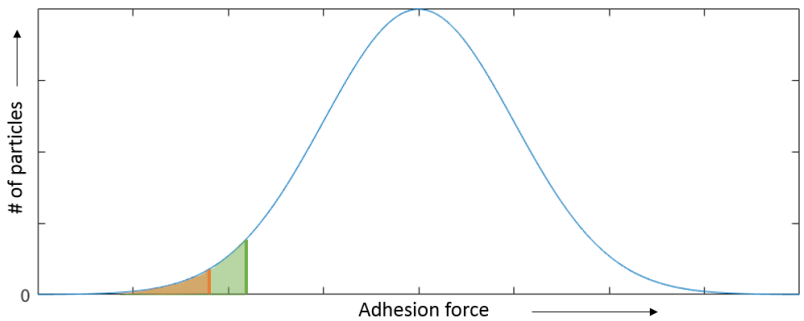

Figure 1.2: *A sketch of the adhesion force distribution. The particles in the orange area can cause problems during operation. During flushing particles with a higher adhesion force are tried to remove, for example the green area.*

Knudsen number is $Kn = \frac{2\lambda}{w}$ with w the width of the channel, and for the particle $Kn_p = \frac{2\lambda}{d_p}$ with d_p the particle diameter. In this study $Kn < 1$, so a continuum approach in combination with wall slip can be used to simulate the flow. $Kn_p \gg 1$, so to calculated the drag on the particles a free molecular approach is needed. The Reynolds number is calculated with $Re = \frac{\rho u L}{\mu}$, where ρ is the density, u is the velocity, L is the critical length scale, and μ is the dynamic viscosity. The width of a channel is typically used to calculate the Reynolds number. When this values becomes larger turbulence can occur. To analyze the flush performance computational fluid dynamics is used to simulate flow fields. In this project the software StarCCM+ is used and depending on the Reynolds number, laminar or turbulence models are used.

The theoretical background of the drag force and the models that are used to simulate flow fields, are discussed in chapter 2. Chapter 3 discusses the geometry, the models, and the corresponding mesh that is used to do the simulations. Furthermore, a proposed flush sequence together with the way of analyzing is presented. Chapter 4 shows the results of the flush sequence plus the results for higher pressures. Finally, the conclusions and recommendations are presented in chapter 5.

Chapter 2

Theoretical background

The ultimate goal of this study is to calculate the total force and force moment on particles during flushing. The two important forces at scanner conditions during flushing are the drag and adhesion force.

In section 2.1 the governing equations that are used to perform the simulations in StarCCM+ are discussed. The relation between the flow profiles and the drag force on spherical particles is discussed in section 2.3. The adhesion force for two different surface particle configurations is derived in section 2.4. Finally, a supersonic jet will be discussed: this is a specific flow feature that occurs at large pressure differences, which is usually the case in this study.

2.1 Governing equations

In the Introduction, the Knudsen number for the geometry is calculated because of the low value the fluid motion can be described as a continuum. Three types of conservation laws are needed to solve the problem: the continuity, the momentum, and the energy equations. In this report the Einstein summation convention is used to write these equations. The conservation laws are derived in subsection 2.1.1. For high Reynolds number these equations can solve turbulence when the grid size is taken infinitely small. This is computationally not feasible, so turbulence models should be used. In subsection 2.1.2 four basic equations for averaged turbulence will be derived. To close the turbulence problem, a fifth equation is needed. Two options will be discussed in subsection 2.1.3 and 2.1.4.

2.1.1 Laminar

The first important equation is the continuity equation. This relation is based on the conservation of mass. When there is not a source in the problem, we can write the continuity equation in differential form as follows

$$\frac{\partial \rho}{\partial t} + \frac{\partial}{\partial x_j}(\rho u_j) = 0, \tag{2.1}$$

where ρ is the density, $(x_1, x_2, x_3) = (x, y, z) = \mathbf{x}$ is the position vector, and $(u_1, u_2, u_3) = (u, v, w) = \mathbf{u}$ is the velocity vector.

A same relation can be defined for the momentum of the flow. Since momentum is a vector three equation are needed, one for each dimension (x, y, z). Conservation of momentum can be written as

$$\frac{\partial}{\partial t}(\rho u_i) + \frac{\partial}{\partial x_j}(\rho u_i u_j) = \text{Forces}. \tag{2.2}$$

The only way to gain more or less momentum is by adding force: this can be a body forces, like gravity, or surface forces, like stresses on the surface of a fluid element. In the problem

that is studied in this report, there are no body forces that affect the flow. The geometry is oriented horizontally and the density is varying slightly so the influence of gravity is negligible. However, surface forces play an important role, these can be divided into surface normal forces, i.e. pressure, and surface tangential forces, i.e. shear. When the surface forces are included, the following relation can be derived

$$\frac{\partial}{\partial t}(\rho u_i) + \frac{\partial}{\partial x_j}(\rho u_i u_j) + \frac{\partial p}{\partial x_j} - \frac{\partial}{\partial x_j}\tau_{ij} = 0, \tag{2.3}$$

where p is the pressure and τ_{ij} is the viscous stress tensor. The stress tensor can be written as

$$\tau_{ij} = \mu s_{ij} = \mu\left(\left(\frac{\partial u_i}{\partial x_j} + \frac{\partial u_j}{\partial x_i}\right) - \frac{2}{3}\frac{\partial u_k}{\partial x_k}\delta_{ij}\right), \tag{2.4}$$

with μ the dynamic viscosity, s_{ij} the strain-rate tensor, and δ the Kronecker delta. These equations can be used to derive exact solutions for a laminar and turbulent channel flow. This is done in section 7.5 (Appendix), since these solutions did not occur in the simulations the derivation is moved to the Appendix.

The last conservation law is the energy (E) equation. This equation has a same form as (2.2), however now the forces are translated in terms of work. Furthermore, an additional term of work by conduction is added. In formulas:

$$\frac{\partial(\rho E)}{\partial t} + \frac{\partial}{\partial x_j}(\rho u_j E) = \text{Work done by Forces} + \text{Conduction}. \tag{2.5}$$

Adding the relations of work done by the surface forces and the conduction result in

$$\frac{\partial}{\partial t}(\rho E) + \frac{\partial}{\partial x_j}(\rho u_j E) + \frac{\partial}{\partial x_j}(u_j p) - \frac{\partial}{\partial x_j}(u_i \tau_{ij}) + \frac{\partial}{\partial x_j} q_j = 0, \tag{2.6}$$

with $(q_1, q_2, q_3) = \mathbf{q}$ the heat flux, and $E = e_s + \frac{1}{2}u^2$ the sum of the sensible energy $e_s = C_v T$, (with C_v the specific heat at constant volume) and the kinetic energy. To close the system a equation of state is used, in this report the ideal gas law will be used,

$$p = \rho R T, \tag{2.7}$$

with R is the universal gas constant. StarCCM+ solves these equations in integral form numerically for small volume elements. StarCCM+ also makes use of a couple of gas kinetic relations, for the thermal conductivity, the dynamic viscosity, and specific heat, but these relations will be out of the scope of this report. In section 3.3 the models that are chosen in StarCCM+ are mentioned. These relations are also used for the turbulence models, which will be derived below.

2.1.2 Turbulent

It is computational not efficient to simulate the exact Navier-Stokes equations on a grid with very small grid size, therefore averaged turbulence models are used to get insight in the turbulent flow behavior. Four basic conservation laws of time averaged quantities are used. These are the continuity, the momentum, the energy, and the turbulent kinetic energy equations. To derive these equations, (2.1), (2.3), and (2.6) are used. In these equations decomposed fields are substituted, and the whole equations are time averaged. For ρ and p standard time averaged compositions are substituted, like $p = \overline{p} + p'$, with $\overline{p}$ the time averaged pressure and p' the fluctuating part. For u_i and E a density weighted time averaged decomposition is used, like $E = \widetilde{E} + E''$, with $\widetilde{E}$ the Favre averaged part and E'' the fluctuating part with respect to the Favre average. In section 7.1 (Appendix) more information about the averaging is presented and an extensive derivation of the conservation relations is presented. This results in the following continuity equation

$$\frac{\partial \overline{\rho}}{\partial t} + \frac{\partial}{\partial x_i}(\overline{\rho}\widetilde{u_i}) = 0. \tag{2.8}$$

For the averaged momentum equation, the following is derived

$$\frac{\partial}{\partial t}(\overline{\rho}\widetilde{u_i}) + \frac{\partial}{\partial x_j}(\overline{\rho}\widetilde{u_i}\widetilde{u_j}) = -\frac{\partial \overline{p}}{\partial x_i} + \frac{\partial}{\partial x_j}(\widetilde{\tau_{ij}} + \overline{\tau''_{ij}} - \overline{\rho u''_i u''_j}). \tag{2.9}$$

The total energy results in

$$\frac{\partial}{\partial t}(\overline{\rho}\widetilde{E}) + \frac{\partial}{\partial x_j}(\overline{\rho}\widetilde{u_j}\widetilde{E}) + \frac{\partial}{\partial x_j}(\widetilde{u_j}\overline{p}) = \frac{\partial}{\partial x_j}(\widetilde{u_i}\widetilde{\tau_{ij}} - \widetilde{u_i}\overline{\rho u''_i u''_j}) + \frac{\partial}{\partial x_j}(-q_{l_j} - q_{t_j}), \tag{2.10}$$

with $\widetilde{E} = \widetilde{e} + \frac{1}{2}\widetilde{u_i}\widetilde{u_i} + k$, where $k = \frac{1}{2}\frac{\overline{\rho u''_i u''_i}}{\overline{\rho}}$ is the turbulent kinetic energy. Furthermore q_{l_j} and q_{t_j} are respectively the molecular and the turbulent heat flux, these can expressed as $q_{l_j} = -\frac{\mu C_p}{Pr_l}\frac{\partial \widetilde{T}}{\partial x_i}$ and $q_{t_j} = -\frac{\mu_t C_p}{Pr_t}\frac{\partial \widetilde{T}}{\partial x_j}$, where $Pr_{(l,t)}$ and $\mu_{(t)}$ are the Prandtl number and the viscosity, for the molecular and turbulent part, more information can be found in Asproulias (2014).

When the decomposed fields (as described above) are substituted in (2.3), and the result is multiplied by u''_i and time averaged, a relation for the turbulent kinetic energy can be derived. The result is

$$\begin{aligned}\frac{\partial}{\partial t}(\overline{\rho}k) + \frac{\partial}{\partial x_j}(\overline{\rho}\widetilde{u_j}k) = &-\overline{\rho u''_i u''_j}\frac{\partial \widetilde{u_i}}{\partial x_j} - \overline{\tau_{ij}\frac{\partial u''_i}{\partial x_j}} + \frac{\partial}{\partial x_j}(\overline{\tau_{ij}u''_i}) \\ &- \frac{\partial}{\partial x_j}\left(\overline{\rho u''_j \frac{1}{2}u''_i u''_i} + \overline{p' u''_j}\right) + \overline{p'\frac{\partial u''_i}{\partial x_i}} - \overline{u''_i}\frac{\partial \overline{p}}{\partial x_i}.\end{aligned} \tag{2.11}$$

In (2.9), (2.10) and (2.11) more complex averaged terms are presented, these terms will be discussed now. The first one is $-\overline{\rho u''_i u''_j}$, which is known as the Reynolds-stress tensor which can modeled using an eddy-viscosity assumption that result in $-\overline{\rho u''_i u''_j} = \mu_t \widetilde{s_{ij}} - \frac{2}{3}\overline{\rho}k\delta_{ij}$, with μ_t the turbulent viscosity estimated with a turbulence model. In the turbulent kinetic energy equation the terms $\overline{\tau_{ij}u''_i}$ and $-\overline{\rho u''_j \frac{1}{2}u''_i u''_i}$ can be modeled as $\overline{\tau_{ij}u''_i} - \overline{\rho u''_j \frac{1}{2}u''_i u''_i} = \left(\mu + \frac{\mu_t}{\sigma_k}\right)\frac{\partial k}{\partial x_i}$. The pressure diffusion $\frac{\partial}{\partial x_j}(\overline{p'u''_j})$, the pressure dilatation $\overline{p'\frac{\partial u''_i}{\partial x_i}}$, and the pressure work $\overline{u''_i}\frac{\partial \overline{p}}{\partial x_i}$ can be neglected (see Asproulias (2014)). The rate of dissipation is determined by $\overline{\rho}\epsilon = \overline{\tau_{ij}\frac{\partial u''_i}{\partial x_j}}$. Using these relations, (2.11) can be written as

$$\frac{\partial}{\partial t}(\overline{\rho}k) + \frac{\partial}{\partial x_j}(\overline{\rho}\widetilde{u_j}k) = -\overline{\rho u''_i u''_j}\frac{\partial \widetilde{u_i}}{\partial x_j} - \overline{\rho}\epsilon + \frac{\partial}{\partial x_j}\left(\mu + \frac{\mu_t}{\sigma_{k'}}\frac{\partial k}{\partial x_j}\right), \tag{2.12}$$

where $\frac{1}{\sigma_{k'}}$ is depending on the model that is used to close the system. Equation (2.8), (2.9), (2.10), and (2.12) and the averaged ideal gas law,

$$\overline{p} = \overline{\rho}R\widetilde{T}, \tag{2.13}$$

are the basis of the turbulence models. Now an extra equations is needed to close the system. In the next subsections, two models will be discussed. One makes use of the conservation of rate of dissipation $k-\epsilon$, and the other one makes use of the conservation of the specific rate of dissipation $k-\omega$ in combination with $k-\epsilon$.

2.1.3 $k-\epsilon$ turbulence model

To close the system that is described above, an extra equation is needed. In the $k-\epsilon$ model a transport equation for the rate of dissipation is proposed. The standard $k-\epsilon$ model is described by Launder and Sharma (1974), where $\frac{1}{\sigma_{k'}} = \sigma_{k2} = 1.0$ is used. In this subsection a simplified form of the ϵ-equation is used, i.e. the near wall behavior corrections are neglected. For a more extensive description, Asproulias (2014) is recommended. In subsection 4.2.1 the extensive model is used to do the $k-\epsilon$ simulations. The simplified transport equation for rate of dissipation is

$$\frac{\partial}{\partial t}(\overline{\rho}\epsilon) + \frac{\partial}{\partial x_j}(\overline{\rho}\widetilde{u_j}\epsilon) = -\overline{\rho u_i'' u_j''}C_{\epsilon 1}\frac{\epsilon}{k}\frac{\partial \widetilde{u_i}}{\partial x_j} - C_{\epsilon 2}\overline{\rho}\frac{\epsilon^2}{k} + \frac{\partial}{\partial x_j}\left(\left(\mu + \frac{\mu_t}{\sigma_\epsilon}\right)\frac{\partial \epsilon}{\partial x_j}\right), \tag{2.14}$$

where the eddy viscosity is

$$\mu_t = C_\mu \overline{\rho}\frac{k^2}{\epsilon}. \tag{2.15}$$

In these relations the constants are, $C_\mu = 0.09$, $\sigma_\epsilon = 1.3$, $C_{\epsilon 1} = 1.44$, and $C_{\epsilon 2} = 1.92$ (see Georgiadis et al. (2006)).

2.1.4 SST (Menter) $k-\omega$ turbulence model

The $k-\epsilon$ model as described in subsection 2.1.3 performs well in a highly free turbulent flow. Normally the $k-\omega$ model (based on specific turbulent kinetic dissipation) has problems with simulating free stream turbulence, but it works better in the near wall region, which is the area of interest in this study. The shear stress transport (SST) $k-\omega$ model combines $k-\epsilon$ and $k-\omega$, using a blending function to get the best result in the free stream and the wall area. As is described in Kostić et al. (2017) and Brown (2011) it can also deal with supersonic flows, which will exist in most of the simulations that are done in this report. In the $k-\omega$ model (2.12) is written in terms of ω, using $\omega = \frac{\epsilon}{\beta^* k}$ ($\beta^* = C_\mu$) resulting in

$$\frac{\partial}{\partial t}(\overline{\rho}k) + \frac{\partial}{\partial x_j}(\overline{\rho}\widetilde{u_j}k) = -\overline{\rho u_i'' u_j''}\frac{\partial \widetilde{u_i}}{\partial x_j} + \overline{\rho}\beta^*\omega k + \frac{\partial}{\partial x_j}\left(\mu + \sigma_{k1}\mu_t\frac{\partial k}{\partial x_j}\right), \tag{2.16}$$

with $\sigma_{k1} = 0.85$. If the exact transformation from (2.12) is used the constant σ_{k1} would be replaced by σ_{k2}, the result is

$$\frac{\partial}{\partial t}(\overline{\rho}k) + \frac{\partial}{\partial x_j}(\overline{\rho}\widetilde{u_j}k) = -\overline{\rho u_i'' u_j''}\frac{\partial \widetilde{u_i}}{\partial x_j} + \overline{\rho}\beta^*\omega k + \frac{\partial}{\partial x_j}\left(\mu + \sigma_{k2}\mu_t\frac{\partial k}{\partial x_j}\right). \tag{2.17}$$

The transport equation of the specific dissipation is given by

$$\frac{\partial}{\partial t}(\overline{\rho}\omega) + \frac{\partial}{\partial x_j}(\overline{\rho}\widetilde{u_j}\omega) = -\overline{\rho u_i'' u_j''}\gamma_1\frac{\omega}{k}\frac{\partial \widetilde{u_i}}{\partial x_j} - \beta_1\overline{\rho}\omega^2 + \frac{\partial}{\partial x_j}\left((\mu + \sigma_{\omega 1}\mu_t)\frac{\partial \omega}{\partial x_j}\right), \tag{2.18}$$

with $\beta_1 = 0.0750$, $\sigma_{\omega 1} = 0.5$, and $\gamma_1 = \frac{\beta_1}{\beta^*} - \sigma_{\omega 1}\frac{\kappa^2}{\sqrt{\beta^*}}$, with $\kappa = 0.41$. To make a combination between the two models, (2.14) is transformed in terms of ω (see section 7.2 (Appendix)), resulting in

$$\begin{aligned}\frac{\partial}{\partial t}(\overline{\rho}\omega) + \frac{\partial}{\partial x_j}(\overline{\rho}\widetilde{u_j}\omega) = &-\overline{\rho u_i'' u_j''}\gamma_2\frac{\omega}{k}\frac{\partial \widetilde{u_i}}{\partial x_j} - \beta_2\overline{\rho}\omega^2 + \frac{\partial}{\partial x_j}\left((\mu + \sigma_{\omega 2}\mu_t)\frac{\partial \omega}{\partial x_j}\right) \\ &+ \frac{2}{k}\left(\mu + \frac{\overline{\rho}k}{\omega}\sigma_{\omega 2}\right)\frac{\partial k}{\partial x_j}\frac{\partial \omega}{\partial x_j} + \frac{\omega}{k}\frac{\partial}{\partial x_j}\left((\sigma_{\omega 2} - \sigma_{k2})\mu_t\frac{\partial k}{\partial x_j}\right).\end{aligned} \tag{2.19}$$

In (2.19) the last term and the cross-diffusion term times μ can be neglected as is stated in Menter (1993). Neglecting these terms results in the following expression for the transformed $k-\epsilon$ model

$$\begin{aligned}\frac{\partial}{\partial t}(\overline{\rho}\omega)+\frac{\partial}{\partial x_j}(\overline{\rho}\widetilde{u_j}\omega) &= -\overline{\rho u_i'' u_j''}\gamma_2\frac{\omega}{k}\frac{\partial \widetilde{u_i}}{\partial x_j}-\beta_2\overline{\rho}\omega^2 \\ &\quad+\frac{\partial}{\partial x_j}\left((\mu+\sigma_{\omega 2}\mu_t)\frac{\partial \omega}{\partial x_j}\right)+2\overline{\rho}\sigma_{\omega 2}\frac{1}{\omega}\frac{\partial k}{\partial x_j}\frac{\partial \omega}{\partial x_j},\end{aligned} \tag{2.20}$$

with $\beta_2 = 0.0828$, $\sigma_{\omega 2}=\frac{1}{\sigma_\epsilon}=0.0856$, and $\gamma_2=\frac{\beta_2}{\beta^*}-\frac{\sigma_{\omega 2}\kappa^2}{\sqrt{\beta^*}}$. When (2.18) and (2.20) are compared, an additional cross-diffusion term in (2.20) is found. To make a combination (2.16) and (2.18) are multiplied by F_2, and (2.17) and (2.20) by $(1-F_2)$. Then the multiplications of (2.16) and (2.18) are added, and the same is done for (2.17) and (2.20). This results in

$$\frac{\partial}{\partial t}(\overline{\rho}k)+\frac{\partial}{\partial x_j}(\overline{\rho}\widetilde{u_j}k)=-\overline{\rho u_i'' u_j''}\frac{\partial \widetilde{u_i}}{\partial x_j}+\overline{\rho}\beta^*\omega k+\frac{\partial}{\partial x_j}\left(\mu+\sigma_k\mu_t\frac{\partial k}{\partial x_j}\right), \tag{2.21}$$

and

$$\begin{aligned}\frac{\partial}{\partial t}(\overline{\rho}\omega)+\frac{\partial}{\partial x_j}(\overline{\rho}\widetilde{u_j}\omega) &= -\overline{\rho u_i'' u_j''}\gamma\frac{\omega}{k}\frac{\partial \widetilde{u_i}}{\partial x_j}-\beta\overline{\rho}\omega^2 \\ &\quad+\frac{\partial}{\partial x_j}\left((\mu+\sigma_\omega\mu_t)\frac{\partial \omega}{\partial x_j}\right)+2\overline{\rho}(1-F_1)\sigma_{\omega 2}\frac{1}{\omega}\frac{\partial k}{\partial x_j}\frac{\partial \omega}{\partial x_j}.\end{aligned} \tag{2.22}$$

In this model the constants $(\beta, \sigma_k, \sigma_\omega)$ can be calculated using

$$\phi = F_1\phi_1+(1-F_1)\phi_2, \tag{2.23}$$

where ϕ is one of these constants. In Menter (1993) is described how F_1 is calculated.

2.2 Wall slip

The low pressure conditions in the scanner result in relatively large mean free paths of the gas molecules. Locally the Knudsen number becomes higher, resulting in a slip flow. To solve flow fields using the continuum equations, the Maxwell slip condition is used Lockerby et al. (2004). This slip relation results in the best bulk solution, which is the area of interest for most physicists. The wall velocity derived by Maxwell is

$$u_{wall}=\frac{2-\sigma_T}{\sigma_T}\lambda\left.\frac{\partial u}{\partial y}\right|_{y=0}, \tag{2.24}$$

with $\frac{2-\sigma_T}{\sigma_T}\lambda=\delta$ the slip length, where σ_T is the tangential momentum accommodation factor and λ is the mean free path.

A very thin layer close to the wall, referred to as the Knudsen layer, is not described well by the Navier-Stokes solution in combination with Maxwell slip, see Figure 2.1a. The effect is only locally at the wall and does not change the overall flow profile. Although the Kundsen layer is very thin (in the order of the mean free path of the gas) it can have an influence on the particles that have to be released, since these are typically much smaller than the mean free path. Solving the problem of the Knudsen layer is hard and out of the scope of this report. For a better explanation Lockerby et al. (2005) can be used. This paper used the solutions of the kinetic theory, direct simulation Monte Carlo (DSMC), higher-order Continuum-fluid equations, and Navier-Stokes equations for Kramer's problem (Mismatch between Navier-Stokes solutions and real velocity profile). The results of the kinetic theory and DSMC are assumed to be correct because they simulate the actual interactions between the molecules. In Figure 2.1b is shown that

the Augment Burnet solution is in best correspondence with these results. This solution is given by

$$u(y) = -\frac{\tau}{\mu}\left(y + \lambda\sqrt{\frac{2}{\pi}}\frac{2-\sigma_T}{\sigma_T} + \frac{7}{10\sqrt{3\pi}}\lambda\left(1 - e^{-\frac{\sqrt{3\pi}y}{\lambda}}\right)\right), \tag{2.25}$$

with

$$-\frac{\tau}{\mu} = \left.\frac{\partial u}{\partial y}\right|_{y\to\infty}. \tag{2.26}$$

In Figure 2.1b the solution of the Navier-Stokes equation is derived using the wall function approach as described in Lockerby et al. (2004). Although, this result in the best wall velocity, this is not resulting in the best bulk solution, normally the Maxwell slip is used to solve the flow. The comparison of (2.25) at $y = 0$ and the Maxwell slip condition results in

$$u_{w,Kn} = \sqrt{\frac{2}{\pi}}u_{w,M}, \tag{2.27}$$

with $u_{w,Kn}$ and $u_{w,M}$, the wall velocities following the Knudsen layer and the Maxwell slip. So if the Maxwell slip velocity is used to calculate the drag on very small particles this is overestimated with a factor $\sqrt{\frac{\pi}{2}}$.

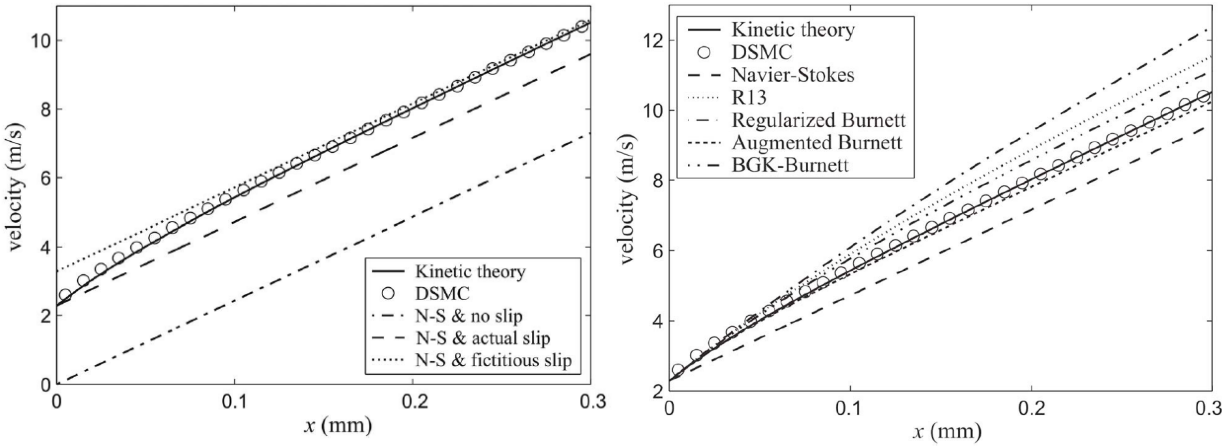

Figure 2.1: *(a) Actual velocity (Kinetic theory and DSMC), and three Navier-Stokes solutions using no slip, Maxwell slip (fictitious slip) and actual slip. (b) Different velocity profiles for different approaches of Kramer's problem. For the Navier-Stokes solution the relation of the real slip ($\delta = \lambda\sqrt{\frac{2}{\pi}}\frac{2-\sigma_T}{\sigma_T}$) is used. (both figures from Lockerby et al. (2005)).*

2.3 Drag force

In chapter 1 the Rock and Roll model is discussed. Assumed in this model is that a moving particle will be released from the surface, by hitting an asperity. In this subsection different models for drag force for different situations will be discussed. A combination between these models will be used to describe the drag force on particles under scanner conditions.

2.3.1 Atmospheric pressure

For very low Reynolds and Knudsen numbers Stokes derived an expression for the drag on spherical objects. The expression is derived using the exact solution of the Navier-Stokes equation for this

case. The result of this derivation is (see Bailey et al. (2005))

$$F_{drag} = 3\pi\mu d_p U, \tag{2.28}$$

with μ the dynamic viscosity, d_p the particle diameter, and U the relative velocity of the particle with respect to the flowfield.

2.3.2 Low pressure

When the pressure decreases, the particle Knudsen number increases. When it becomes much larger than one, The flow around the particle will not behave as a continuum anymore but will behave as a free molecular flow. A description of the flow as Stokes derived is completely wrong. However the formula for the drag force is not completely worthless. Ebenezer Cunningham derived an empirical correction factor as a function of the Knudsen number. Including this correction factor, the drag force for all Knudsen numbers is given by (see Bailey et al. (2005))

$$F_{drag} = 3\pi\mu d_p \frac{U}{C_C}, \tag{2.29}$$

with,

$$C_C = 1 + Kn_p(a + be^{-\frac{c}{Kn_p}}), \tag{2.30}$$

where Kn_p is the particle Knudsen number, and a, b, and c are constants depending on the gas. In this study N_2 is used which is comparable with XCDA and thus with air. The values for air are $a = 1.165$, $b = 0.483$, and $c = 0.997$ (see Kim et al. (2005)).

2.3.3 Particle close to wall at atmospheric pressure

Both subsections above are describing the drag force for a uniform velocity field. However the flow field close to a wall, will normally result in a gradient in the velocity profile. At atmospheric pressure this situation is studied a lot in the past. Chaoui and Feuillebois (2003) derived a correction factor as function of the distance from the wall to the center of the sphere. The relation (2.28) will become

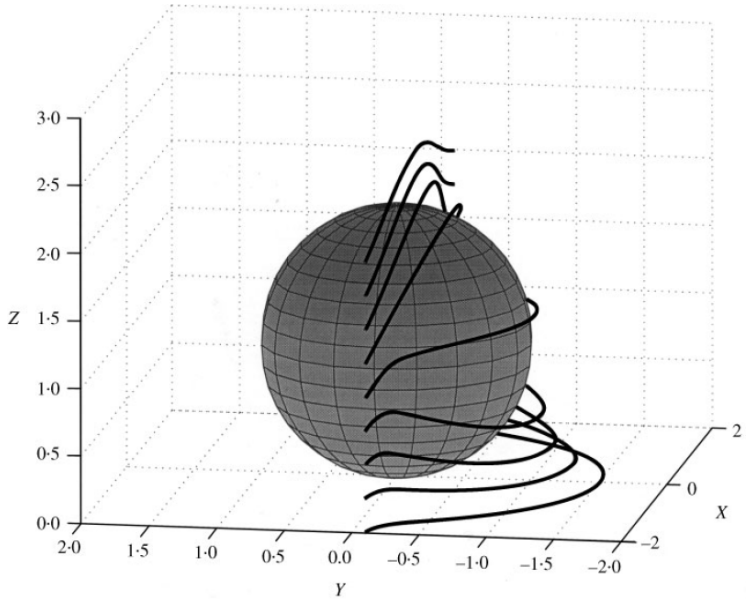

Figure 2.2: *Streamlines around a sphere in presence of a wall (Figure from Chaoui and Feuillebois (2003)).*

$$F_{drag} = 3\pi\mu d_p f(l) l G, \tag{2.31}$$

where G is the velocity gradient, l is the distance from the center of the particle to the wall, and $f(l)$ is given by

$$f = \sum_{i=0}^{N} g_i \left(\frac{\frac{1}{2}d_p}{l} \right)^i, \tag{2.32}$$

with g_i coefficients (see Chaoui and Feuillebois (2003)). When l in (2.32) is $\frac{1}{2}d_p$, f becomes 1.7009, and if $l \gg \frac{1}{2}d_p$, f trends towards 1. The wall limits the freedom of the fluid to move around the particle and therefore the flowfield is distorted and more focused on the particle which results in a larger drag force. In Figure 2.2 the effect of the wall on the streamlines is shown.

2.3.4 Particle close to wall at low pressure

Since the pressure in the scanner is very low, a Cunningham correction factor should be implemented in (2.31). The low pressure will also result in a slip velocity along the wall, which is given by $u_{wall} = \delta \frac{\partial u}{\partial u}$, where δ is the slip length as described in section 2.2. To make a combination between the two correction factors described in the two subsections above, a fictional wall at distance δ is assumed, as shown in Figure 2.3. Now the total relation becomes

$$F_{drag} = 3\pi\mu d_p \frac{f(l) l G}{C_C} = 3\pi\mu d_p \frac{f(\delta + \frac{1}{2}d_p)(\delta + \frac{1}{2}d_p) G}{C_C}, \tag{2.33}$$

which is probably the best approach. Although, this result seems the best approximation, for the global analysis a simplified relation will be used to get a good approximation for a wider range of particle sizes. In the next section this simplified relation will be derived.

2.3.5 Simplified drag froce

C_c in (2.33) can be simplified to $C_C = Kn_p(a + b)$ for high Knudsen numbers (this can be seen in Figure 7.18 (Appendix)), which is typically the case at scanner conditions. Using the relation for Kn_p and the mean free path, C_C can be written as

$$C_C = \frac{2\lambda}{d_p}(a + b) = \frac{\sqrt{2} K_B T}{\pi d_p P \sigma^2}(a + b). \tag{2.34}$$

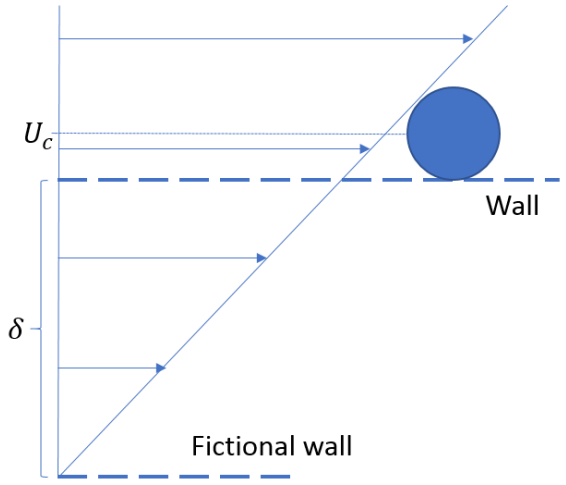

Figure 2.3: *The fictional wall approach as a result of the slip velocity at low pressures*

For the scanner conditions, δ is typically much larger than $\frac{1}{2}d_p$ resulting in $f(\delta+\frac{1}{2}d_p)$ approaching 1 and $\delta + \frac{1}{2}d_p \approx \delta$, and δG can be seen as the wall velocity U_W. All these assumptions result in the following relation

$$\frac{F_{drag}}{d_p^2} = \frac{3\pi^2 \mu P \sigma^2 U_W}{\sqrt{2} K_B T (a+b)}. \tag{2.35}$$

These assumptions make it possible to find an expression that is independent of the particle diameter, of course this is only valid for small particles. This relation will be used to calculate the normalized drag force on the critical surface.

2.4 Adhesion force

In this section, two different configurations of particles and walls will be analyzed. Under flushing conditions the concentration of H_2O is very low, and the particles are not charged. So the Van der Waals force is the dominating force for the particle adhesion, which is based on the interaction energy between a particular wall and particle. In section 7.6 (Appendix), the adhesion force for a sphere-wall and a sphere-sphere interaction are derived. The adhesion forces are given by

$$F_{sphere,wall}(D) = \frac{\pi^2 C \rho_1 \rho_2 R}{6D^2} = \frac{AR}{6D^2}, \tag{2.36}$$

and

$$F_{sphere,sphere}(D) = \frac{\pi^2 C \rho_1 \rho_2}{6D^2}\left(\frac{R_1 R_2}{R_1 + R_2}\right) = \frac{A}{6D^2}\left(\frac{R_1 R_2}{R_1 + R_2}\right), \tag{2.37}$$

where A is the Hamaker constant, which is constant for a specific sphere wall combination, depending on the atom densities of the materials. These two simple expressions are used to build up more complex configurations, using spherical asperities on the wall and particle. In this section two cases will be discussed. The first one is the a perfectly spherical particle close to a wall with two sizes of asperities (Figure 2.4), and the second one is a sphere with two sizes of asperities close to the same wall (Figure 2.5).

The first case is derived by Rabinovich et al. (2000b) and the relation is derived by summing the interaction forces between a flat wall and the spherical particle, a sphere and the spherical particle, and a smaller sphere and the spherical particle. The result can be written as

$$F_{Rab} = \frac{A}{6}\left(\frac{R_p}{(D + H_{p,l} + H_{p,s})^2} + \frac{r_{p,l}}{(D + H_{p,s})^2} + \frac{r_{p,s}}{D^2}\right). \tag{2.38}$$

In the second case, two asperity sizes on the particle will be considered as well, this is done by LaMarche et al. (2017). A same approach is used, but now the particle can be subdivided in three small spheres, resulting in $2 \times 3 = 6$ more terms. The result can be written as

$$\begin{aligned} F_{LaMarche} =& \frac{A}{6}\left(\frac{R_p}{(D + H_{p,l} + H_{p,s} + H_{w,s} + H_{w,l})^2} + \frac{R_p r_{w,l}}{(R_p + r_{w,l})(D + H_{p,l} + H_{p,s} + H_{w,s})^2}\right. \\ &+ \frac{R_p r_{w,s}}{(R_p + r_{w,s})(D + H_{p,l} + H_{p,s})^2} + \frac{r_{p,l}}{(D + H_{p,s} + H_{w,s} + H_{w,l})^2} \\ &+ \frac{r_{p,l} r_{w,l}}{(r_{p,l} + r_{w,l})(D + H_{p,s} + H_{w,s})^2} + \frac{r_{p,l} r_{w,s}}{(r_{p,l} + r_{w,s})(D + H_{p,s})^2} \\ &\left. + \frac{r_{p,s}}{(D + H_{w,s} + H_{w,l})^2} + \frac{r_{p,s} r_{w,l}}{(r_{p,s} + r_{w,l})(D + H_{w,s})^2} + \frac{r_{p,s} r_{w,s}}{(r_{p,s} + r_{w,s}) D^2}\right). \end{aligned} \tag{2.39}$$

This seems as a very complex equation, but it is nothing more than the sum of all simple wall-sphere or sphere-sphere interactions.

Using Atomic Force Microscopy (AFM), a surface map can be provided, this map contains the height of the surface at a given positions. These maps are typically characterized with a the Root Mean Square (RMS) of the roughness height ($rms_{i,j}$) and the wavelength ($\lambda_{i,j}$). The heights and radii in (2.38) and (2.39) can be expressed in these two variables using

$$r_{i,j} = \frac{\lambda_{i,j}^2}{32 k_1 rms_{i,j}} \tag{2.40}$$

and

$$H_{i,j} = k_1 rms_{i,j}. \tag{2.41}$$

These relations are derived by Rabinovich et al. (2000b), and the constant k_1 is given by, $k_1 = 1.817$. This makes it possible to get a general adhesion force between the wall and the particle. Depending on the roughness of the particle and surface, it can be decided if (2.38) suffices, or that (2.39) is needed to describe the configuration in an acceptable way. There is variation in surface-particle configuration and so there will be a distribution of adhesion forces and moments. Since this study focuses on the drag force on the particle as a result of flow, the distribution will not be discussed. Based on flushing tests and surface cleanliness data it is known that only the tail of the distribution is removed, i.e. only the most loose particles are removed. However, removing these particles from the system will make sure that these are not released during production, which results in a positive effect of flushing on the systems defectivity performance.

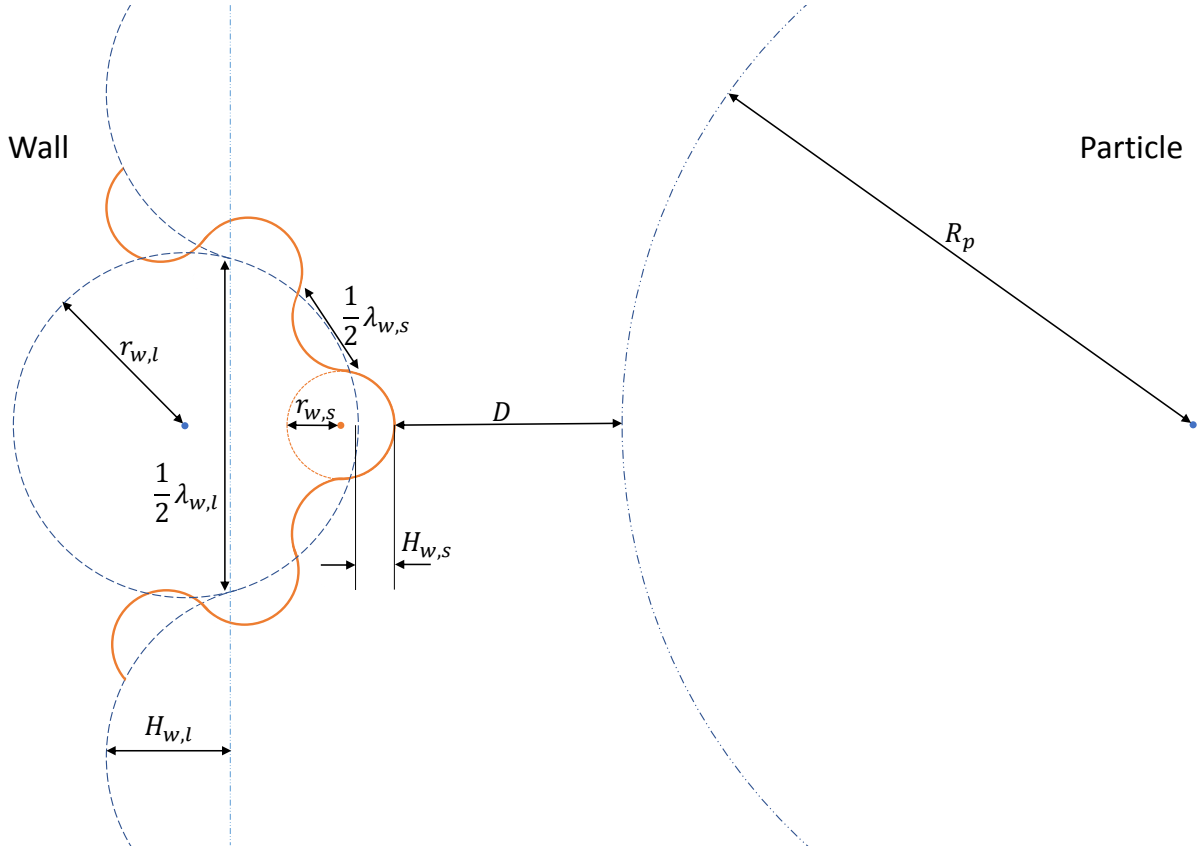

Figure 2.4: *Perfect sphere close to a wall with two asperity sizes.*

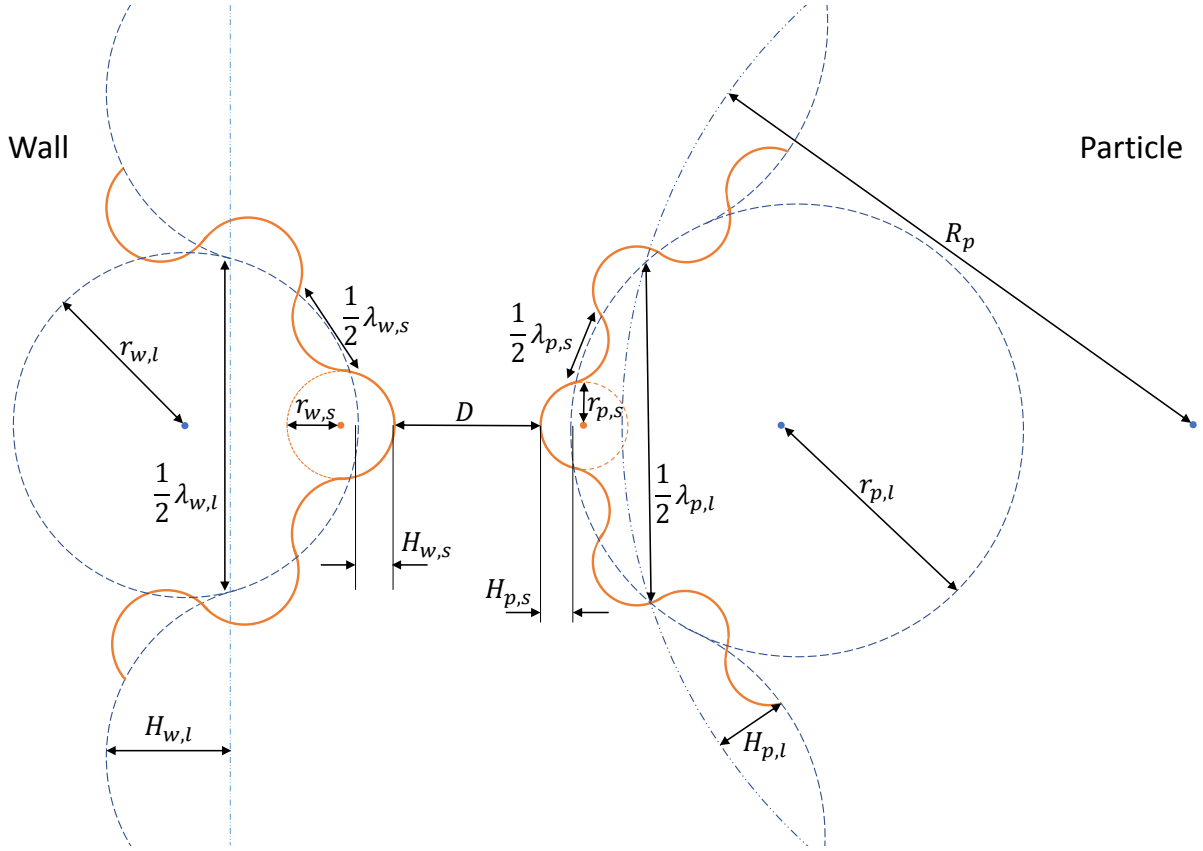

Figure 2.5: *Sphere with two asperity sizes close to a wall with two asperity sizes.*

2.5 Supersonic jet

Cleaning the critical surfaces with a gas flow through the nozzle (see Figure 3.1) is the main interest of this report. A fixed gas flowrate is injected through the nozzle with a significantly high supply pressure. The small dimension of the nozzle can result in a large pressure build-up in the nozzle. If the pressure inside the nozzle is much higher than outside the nozzle, a supersonic jet will form. This means that the gas moves faster than the speed of sound (c), typically described with the Mach number $Ma = v_{gas}/c > 1$. In Figure 2.6 the structure of an underexpanded round jet is shown. In Powell (1988) the minimum pressure ratio between the reservoir (p_0) and the ambient pressure (p_a) to get an underexpanded supersonic jet is calculated. This relation is

$$\frac{p_0}{p_a} = \left(\frac{\gamma+1}{2}\right)^{\frac{\gamma}{\gamma-1}}, \tag{2.42}$$

with γ the ratio of specific heats of a gas. In this report nitrogen is used as gas, with $\gamma = 1.4$, resulting in $p_0/p_a = 1.893$. When the ratio becomes higher than 1.893 the gas will reach velocities higher than the speed of sound at the end of the nozzle. When this is the case expansion fans will form at the orifice. These fans are build up from expansion waves, these waves reach until the boundary of the jet, so Ma becomes smaller than 1. Outside the jet the pressure is the constant ambient pressure p_a, so the expansion waves are reflected as compression waves, which will form together a shock wave. The shock will reach the jet Boundary, and the same as at the orifice will occur. So expansion fans will form, and everything repeats. The final result is an infinitely long chain of shock cells. When the gas is not inviscid, the mixing region around the jet boundary will shrink the shock cells further down stream. The mach value at which the flow is completely expanded to the background pressure is given by (Powell, 1988)

$$Ma_{fe} = \left(\frac{2}{\gamma - 1}\right)^{\frac{1}{2}} \left(\left(\frac{p_0}{p_a}\right)^{\frac{\gamma-1}{\gamma}} - 1\right)^{\frac{1}{2}}. \tag{2.43}$$

The length of the first shock cell normalized by the diameter of the orifice is derived by Prandtl (1904), and is

$$\Delta_1 = 1.2\sqrt{\frac{p_0}{p_a} - 1.9}. \tag{2.44}$$

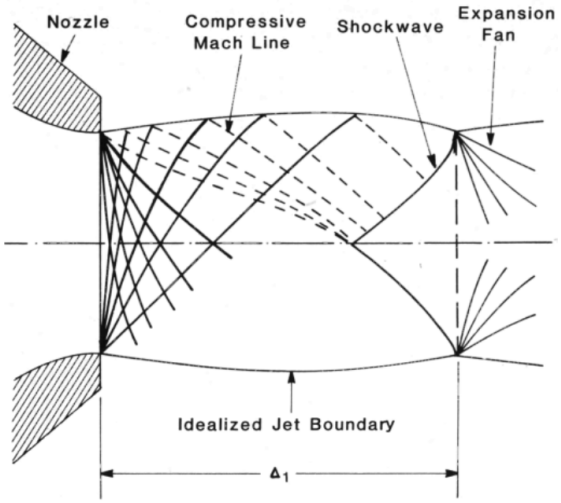

Figure 2.6: *Structure of an underexpanded sonic jet. This picture is valid for an inviscid gas, for viscous gasses a mixing region around the jet boundary will be present. On the left hand side of the nozzle, a large reservoir with constant pressure is present. (Picture from Powell (1988)).*

Chapter 3

Method

As a starting point the area of interest will be discussed in section 3.1. For this area a simple 2-dimensional geometry together with the mesh that is used is presented. In section 3.2, the proposed flush sequence will be subdivided in different intervals, to perform an analysis on every interval. When the total sequence is analyzed, other pressures will be tried as well, to fully understand the critical flow behavior. From that rules for an optimum flushing recipe can be defined. The models and the input that are used to execute the simulations in StarCCM+ will be discussed in section 3.3.

3.1 Area of interest

One of the most critical areas in the scanner is the Reticle Mini Environment (RME). The critical surface (reticle) that holds the pattern which is to be printed, is located here. The EUV light is completely in focus when it hits the critical surface. Small particles can stick to the critical surface, and will influence the light that is reflected, resulting in defective printed chips. The idea of flushing is removing and transporting particles away from the critical areas using a gas flow. Simulating the gas flow can give insight in the flushing performance. The whole vacuum of the scanner is about 5 cubic meters, which makes simulations computational very expensive. When transient effects will be simulated, as in this research, simulations for the whole scanner become computational not feasible. So a simplified model is needed to perform representing simulations.

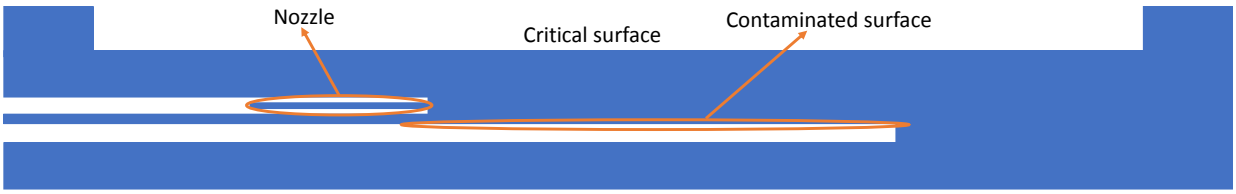

Figure 3.1: *A simplified cross section of the RME (colored part), the hardware is indicated with the white parts.*

When we move normal to the cross section in the RME (Figure 3.1), the geometry will not change much. The geometry of the nozzle indicates that we can assume that it is producing a plane jet. Because of the non-changing geometry and the plane jet a 2-dimensional approach can be useful. Figure 3.2 shows the simplified 2-dimensional model and the mesh that is used. The contaminated surface that is shown in Figure 3.1 can hold a significant amount of particles. As it is close to the reticle, it can have a big impact on the defectivity. The gas that is injected through the nozzle expands and interacts with the gas behind the nozzle. A more complex flow is expected there and a locally finer mesh is used to capture the important fluid dynamics. In Figure 3.2, the general base size of the cells is 5×10^{-4} m, in the black areas a finer mesh is used and the base size is

7.5×10^{-5} m. Close to the wall prism layers with a thickness of 3.5×10^{-4} and 25 layers are used to get a smooth transition to very thin cells close to the wall.

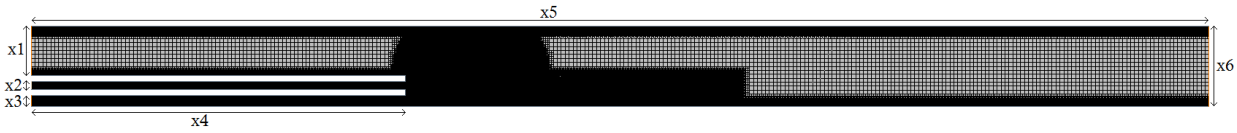

Figure 3.2: *The geometry and mesh that is used. This is a simplified part of Figure 3.1, with* $x1 = 6.185$, $x2 = 1$, $x3 = 1.4$, $x4 = 47.63$, $x5 = 150$, *and* $x6 = 10.085$ mm. *On the left hand side we see three boundaries, the top and bottom one are pressure outlets, and the middle one is a mass flow boundary (nozzle). On the right hand side a pressure outlet is chosen as well. All other boundaries are walls. The dark areas are areas with a finer mesh, in total the mesh is consisting of almost 7 million cells*

3.2 Simulations and analysis

Figure 3.3 shows a simple sketch of the proposed flush sequence. The flowrate (f_{low}) and pressure (p_{low}) are low before a pulse. Then a valve is opened in 0.1 seconds and from there the gas has to travel through some piping before reaching the nozzle. This results in a continuous increase from f_{low} to $f_{high} = 5 \cdot f_{low}$ in a very short time. To get an insight in the maximum effects of this increase, the switch will be simulated as an instantaneous event. This higher flowrate will increase the pressure in the total vacuum slowly until the pressure reaches p_{high}. Then the flowrate will be decreased (back to f_{low}) and consequently the pressure slowly drops to the low-

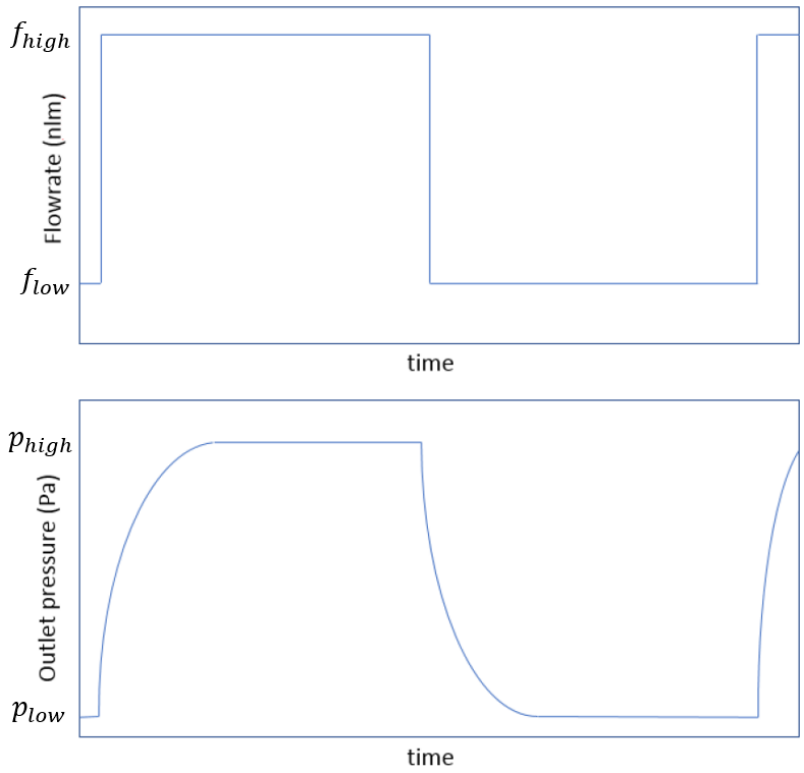

Figure 3.3: *Sketch of flush sequence. Upper graph: flowrate development. Lower graph: outlet pressure development. Almost instantaneous flow rate increase, while pressure increases slowly (in order of minutes).*

pressure limit (p_{low}). The duration of this sequence is in order of minutes. First simulations were showing, that the development of the flow in the simplified geometry is developed in order of milliseconds. This can be used as an argument that the sequence can be divided in four parts, in which only the flowrate or background pressure will be changed. The first step in the sequence that has to be simulated, is the increase in flowrate from f_{low} to f_{high} at constant pressure p_{low}, this is simulated for 0.001 s. In the second part, the flowrate is kept constant (f_{high}) and the pressure will be increased linearly from p_{low} to p_{high} in 0.01 s. Then the background pressure is kept constant (p_{high}) and the flowrate is decreased from f_{high} to f_{low}, and this is simulated for 0.001 s. In the final step the background pressure is linearly decreased from p_{high} to p_{low} in 0.01 s and the flowrate stays at f_{low}. Making these assumptions, the sequence that is originally computational very heavy and not feasible can now be simulated much faster to get insight in the physical behavior during a flush.

To analyze the behavior of the drag force along the contaminated surface the quantities in (2.35) should be extracted. These are the dynamic viscosity (μ), the pressure (P), the wall velocity (U_W), and the temperature (T). This is only done in a very thin layer just above the contaminated surface. Only the cells that are within 5×10^{-6} m distance form the contaminated surface are extracted. Using the information per position on this surface the drag force per position can be calculated. For these transient simulations a graph can be made per timestep, and maximum values will be studied.

The next step in this report is analyzing the flush effectiveness for different pressures. The background pressures that are tested in combination with the flowrate f_{high} are: 10, 500, 800, 1500, 2500, 3500, and 5000 Pa. These cases are tested using transient laminar simulations of 0.001 s. Then the averaged fields are analyzed to get a drag force curve as function of the position on the contaminated surface. Furthermore are the maximum values per position analyzed. For the $k-\epsilon$, and the SST (Menter) $k-\omega$ steady simulations the same type of curves are calculated. To give one value of drag force along the contaminated surface per pressure per model, the area under the graphs is summed. So the drag force value per position is multiplied by the width of the cell and summed all together. Since the values under the nozzle are not interesting these are not taken into account in the summation. The values at the end of the domain are highly influences by the constant pressure boundary at the right, so the results of the simulations in the last 0.5 cm are ignored in the summations as well.

3.3 Models

3.3.1 Laminar

As is described in section 3.2 the transient behavior of the flush sequence will be simulated with StarCCM+. To analyze this flush sequence the following models are used in StarCCM+:

- Two Dimensional
- Gas
- Coupled Flow
- Gradients
- Ideal Gas
- Coupled Energy
- Laminar
- Maxwell Slip

Some initial and final states in the four parts of the sequence, described in section 3.2 are steady solutions. The Steady model is used to calculate these solutions. To simulate the transient

behavior the Steady model is replaced by the Implicit Unsteady model, together with the Convective CFL Time-Step Control model. During these simulations the time step is 2×10^{-7} s. To simulate the compressible behavior of the gas, incompressible should be deselected in the Ideal Gas model. In the Gas model N_2 is selected, and for some material properties are non-default models or constants chosen. These material properties, combined with the chosen models or constants are:

- Dynamic Viscosity: Chapman-Enskog
- Specific Heat: Gas Kinetic
- Thermal Conductivity: Kinetic Theory
- Momentum Accommodation Factor: 0.9

The value of the Momentum Accommodation Factor is widely used within ASML, and it is close to the value found in Hermadri et al. (2018).

Since the mesh, as is shown in Figure 3.2 is consisting of a lot of cells, it can be efficient to run the simulations on multiple cores. It has been determined that the use of 6 cores resulted in the fastest simulations. Unfortunately, transient simulations can not run very efficient in parallel, since every new time step needs the information of the time step before. The simulations of 0.001 s, will take around one or two days and thus the 0.01 s simulations will take more than a week. The time step can be increased to make the simulations faster. But than the length of the time step times the velocity becomes larger than a grid cell, which result in wrong simulations. This is well described by the Courant number. Furthermore, a mesh optimization can increase the speed without losing to much detail.

3.3.2 Turbulent

After the flush sequence, as described in section 3.2, is simulated using the Laminar model, different constant pressures will be simulated individually. These pressures are stated in section 3.2 and they will be tested with laminar transient simulations (to simulate the instabilities) using the models as described in subsection 3.3.1. The high pressure cases can result in turbulent flows and turbulent models preform probably better. So two steady turbulent models will be used. Unfortunately the Maxwell Slip model cannot be used in combination with turbulence models, so the wall velocities should be calculated manually using (2.24). The material property models are chosen the same as in subsection 3.3.1. Of course the Momentum Accommodation Factor is not possible to choose since the Maxwell Slip cannot be chosen. The general models that should be selected to do the turbulent simulations are:

- Two Dimensional
- Gas
- Coupled Flow
- Gradients
- Ideal Gas
- Coupled Energy
- Steady
- Turbulent
- Reynolds-Averaged Navier-Stokes

The $k - \epsilon$ turbulence model is the first turbulence model that is used. To perform these $k - \epsilon$ simulations the following additional models should be chosen:

- K-Epsilon Turbulence
- Realizable K-Epsilon Two-Layer
- Exact Wall Distance
- Two-Layer All y+ Wall treatment

The second turbulence model is the SST (Menter) $k - \omega$ model. The additional models that should be selected to perform simulations using this model are:

- K-Omega Turbulence
- SST (Menter) K-Omega
- Exact Wall Distance
- All y+ Wall treatment
- Gamma Transition

Chapter 4

Results

In this chapter the results of the simulations that are done with StarCCM+ will be shown. In section 4.1, the flush sequence as is proposed in section 3.2 will be studied. The general flow behavior will be discussed, of special interest are the resulting velocities and drag forces along the contaminated surface. The main conclusion is that the background pressure should be optimized to get the best flushing results. So the next step is to find the optimum pressure. This is discussed in section 4.2.

4.1 Flush sequence

4.1.1 Flow increase from f_{low} to f_{high}

In this part of the sequence the background pressure is kept constant at p_{low}. Instantaneously the flowrate will be increased from f_{low} to f_{high}. Both flowrates result at this low background pressure in a laminar steady solution, the velocity profiles are presented in Figure 4.1. The flow through the small nozzle results in a pressure build-up. When the ratio between the pressure in the nozzle and in the background becomes large enough (see section 2.5), a supersonic jet will be the result. These supersonic jets are characterized by a chain of shock cells, in which expansion and compression waves are reflected. In Figure 4.1a (and less clear in 4.1b) these cells are observed. These shock cells exist only in supersonic flows, where the Mach number is larger than one, which we are dealing with according to Figure 4.2b. In section 4.2 a short analysis on the length and widths of these shock cells will be done.

A higher flowrate results in a higher pressure at the end of the nozzle causing a larger expansion, as can be seen in Figure 4.1b. Now the expansion is so wide that it is limited by the wall, resulting in a higher pressure just downstream the nozzle on the lower surface, see Figure 4.2a. This generates locally a second expansion. The interaction between the expansion wave behind

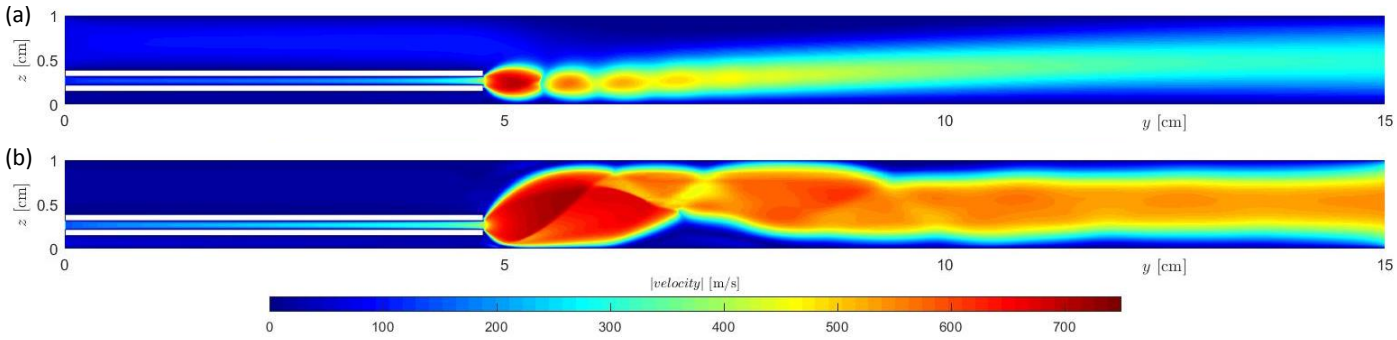

Figure 4.1: *Graphical representation of the spatial distribution of the absolute value of the velocity at p_{low} and flowrate f_{low} (a) and f_{high} (b).*

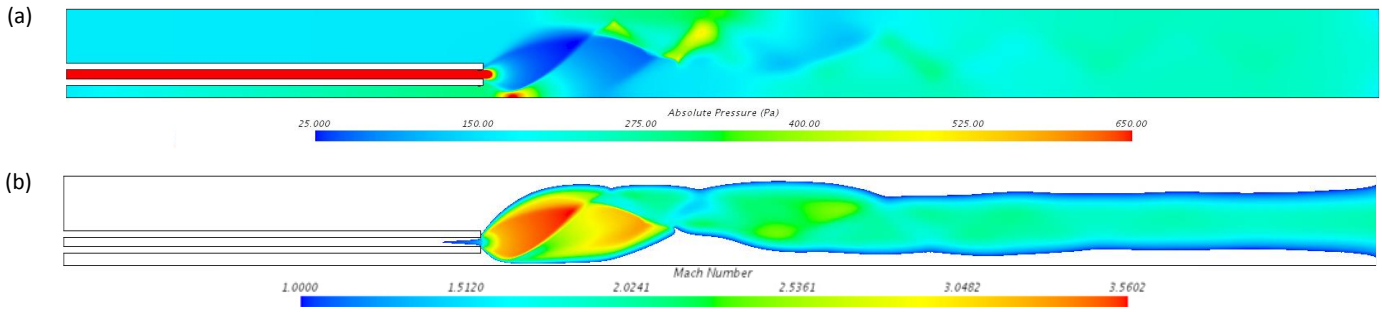

Figure 4.2: *Graphical representation of the spatial distribution of the absolute pressure (a) and the Mach number (b) at flowrate: f_{high} and background pressure: p_{low}.*

the nozzle and the reflections at the walls results in the quite complex, but steady flow field, as is shown in Figure 4.1b.

Particles should be released from the lower surface in the geometry. To calculate the drag force on small particles on this surface, (2.35) is used. The pressure, dynamic viscosity, and the temperature can be be extracted straightforwardly from the simulations. For the wall velocities, the cell layers that are the closest to the contaminated surface are used (see section 3.2). For every position on this wall, a linear fit of velocity versus wall distance is made, from which the wall velocity can be extracted. The velocity as function of position on the contaminated surface is plotted in Figure 4.3a. Using (2.35) the drag force on small particles along this surface is plotted in Figure 4.3b. In both figures the first part of the flushing sequence is plotted with three lines, i.e. the end and begin solutions, and the maximum values during the transition. Increasing the flowrate results in a local high peak in wall velocity just behind the nozzle. Since the pressure in the whole regime is very low at the beginning the highest values in wall velocity are reached during the flow development as result of the increased flowrate. The drag force as derived in (2.35) is dependent on the pressure, so this very high wall velocity does not result in the highest drag force. The drag force peak just downstream of the nozzle reaches the highest value at the end of this part of the sequence. Further downstream the drag force during the transition is significant higher than the two steady state solutions, which is the result of the developing flow. This is suggesting

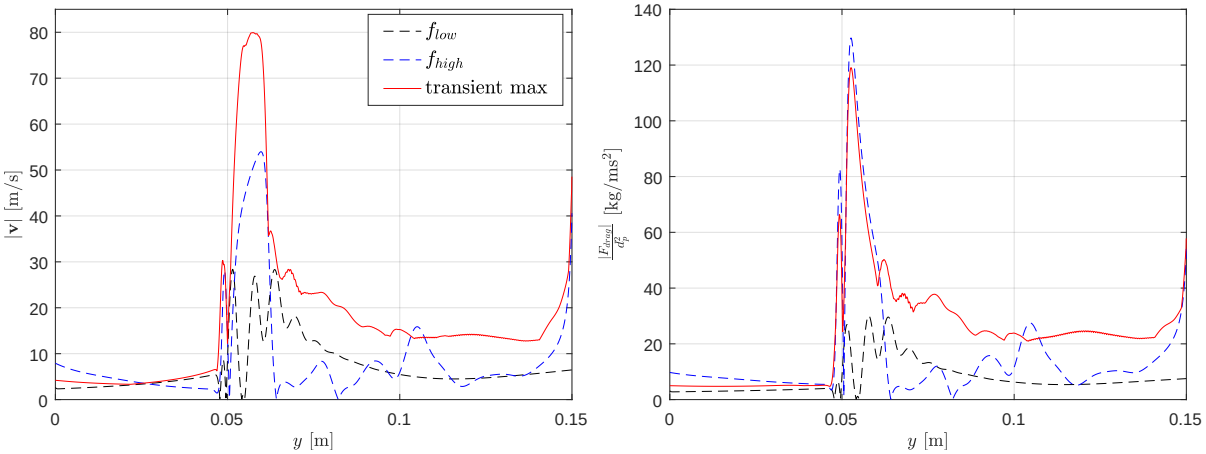

(a) **(b)**

Figure 4.3: *Wall velocity (a) and drag force on small spheres (b) along the contaminated surface for f_{low} (black dashed line), f_{high} (blue dashed line) and the maximum values during the transition (red solid line). The background pressure is taken constant at p_{low}.*

that pulsating flushes can improve the efficiency. However, this part of the sequence seems not very efficient, since the big expansion only results locally in high drag values. The expansion is also the cause that the flow and so the momentum is distributed over the whole width of the channel, resulting in low drag forces along the contaminated surface further downstream.

4.1.2 Pressure increase from p_{low} to p_{high}

The flowrate is kept constant at f_{high} in the second part of the sequence while the background pressure is linearly increased from p_{low} to p_{high}. The large expansion at p_{low} (Figure 4.1b) becomes smaller in size, because of the higher pressure. A supersonic jet consisting of a chain of shock cells as shown in Figure 4.5 is the result (Buchmann et al., 2013). Furthermore, the steady solution at p_{low} becomes unsteady at high pressure. Unsteady features are observed when the background pressure is around 500 Pa and they become larger in size at higher pressures.

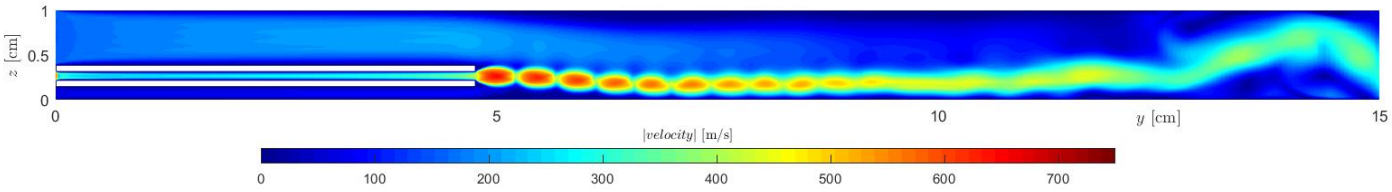

Figure 4.5: *Graphical representation of the spatial distribution of the absolute value of the velocity at p_{high} and a flowrate of f_{high} at a random timestep.*

Since the pressure becomes higher the mean free path and thus the slip along the contaminated surface becomes smaller (see (2.24)). On the other hand the higher pressure results in a more focused jet depicted in Figure 4.5. This jet is covering less vertical area than for the p_{low} case, so the momentum is more focused along the contaminated surface. Consequently large velocity gradients close to the wall are found, resulting in high values of wall velocity (see (2.24)). In Figure 4.4a the x-velocities on the contaminated surface are shown. Indeed a decrease in wall velocity for the higher pressure flow is seen. However, there is still a wide range where a wall velocity as a result of the steep gradient is found. This velocity combined with the higher background pressure

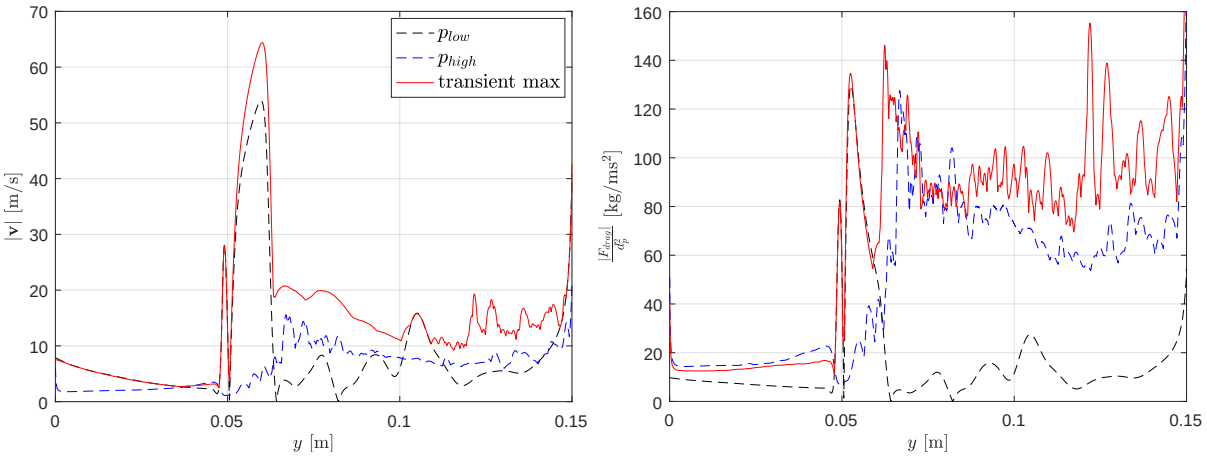

(a) **(b)**

Figure 4.4: *Wall velocity (a) and drag force on small spheres (b) along the contaminated surface for p_{low} (black dashed line), p_{high} (blue dashed line) and the maximum values during the transition (red solid line). The flowrate is taken constant at f_{high}.*

results in a high drag force in a wide range, as can be seen in Figure 4.4b. It should be noted that the blue dotted line in Figure 4.4 are the maximum values that are found during a transient simulation of 0.01 s. Where f_{high} at p_{low} resulted in a very local peak with high drag, high drag values are found in a wide range for f_{high} at p_{high}. The higher background pressure forces the jet to develop over a smaller area, combined with the unsteady behavior results in a more effective way of flushing. Increasing the pressure more results in even less slip, and finally the slip will completely disappear. This suggest that there should be an optimum pressure. Figure 4.4b suggests that this optimum is located between p_{low} and p_{high}, since the transient maximum value is higher than both solutions. This can also be the result of the fast linear increase in pressure, so the flow is not completely developed for every pressure, in reality the pressure is increased much slower, but this is computational not feasible. In section 4.2 several pressures will be simulated, to determine an optimum pressure for f_{high}.

4.1.3 Flow decrease from f_{high} to f_{low}

In the third part of the flushing sequence the background pressure is kept constant at p_{high}, while the flowrate is decreased instantaneously from f_{high} to f_{low}. During the transition the unsteady flow in Figure 4.5 becomes steady again, which is shown in Figure 4.6. Since the flowrate is lower, there is a smaller pressure build-up in the nozzle. The difference between the background pressure and the pressure at the end of nozzle is not big enough to get an supersonic jet. A narrow jet that grows slowly in width is the result. An interesting feature, that is also visible in Figure 4.5 and 4.1, but even more clear in Figure 4.6, is that the jet is pulled to the closest wall. This is a result of the limited entrainment of gas on the bottom side of the jet by the closer lower wall. Locally a lower pressure area just below the nozzle is the result, pulling the jet to the wall, this effect is known as the Coanda effect (Wille and Fernholz, 1965).

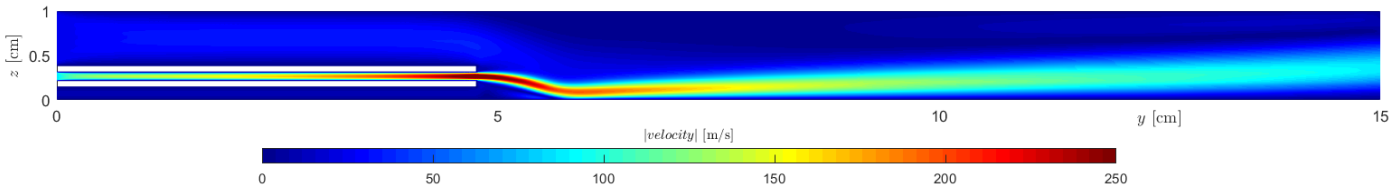

Figure 4.6: *Graphical representation of the spatial distribution of the absolute value of the velocity at p_{high} and flowrate f_{low}.*

Flushing wise this step is not interesting, since the lower flowrate will result in less momentum that can hit the particles. In Figure 4.7 is shown that the wall velocity and drag force becomes much lower for the lower flowrate. The highest peak seems to scale with the flowrate scaling (scaling f_{high}/f_{low}=5), but further downstream the p_{high} case results in even higher drag forces than a factor 5 difference with the f_{low} case which can be related to instabilities.

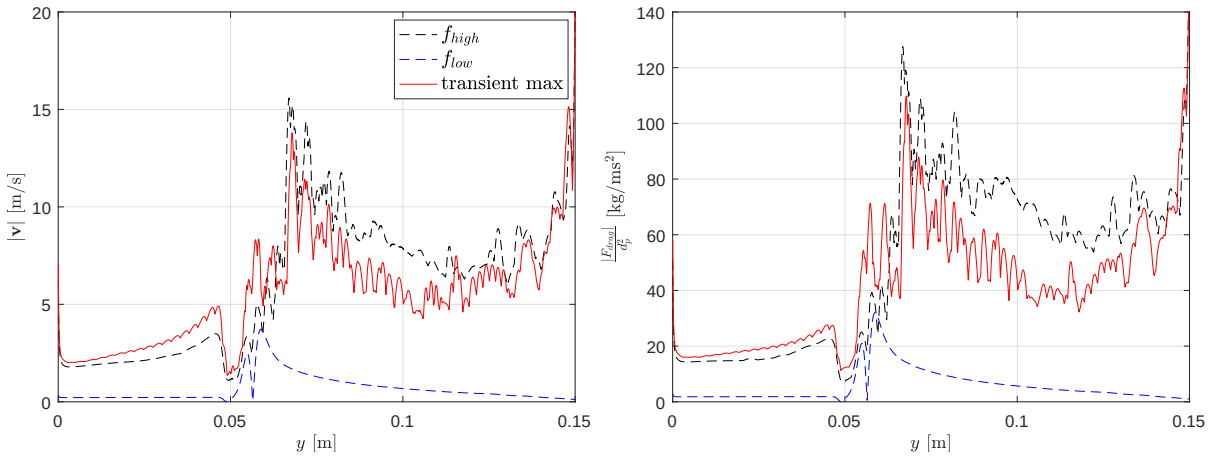

(a) **(b)**

Figure 4.7: *Wall velocity (a) and drag force on small spheres (b) along the contaminated surface for f_{high} (black dashed line), f_{low} (blue dashed line) and the maximum values during the transition (red solid line). The background pressure is constant at p_{high}.*

4.1.4 Pressure decrease from p_{high} to p_{low}

To close the sequence the background pressure is decreased linearly to p_{low}, keeping the flowrate at f_{low}. The flow profile as is shown in Figure 4.1 is the result. The lower background pressure increases the pressure difference between the end of the nozzle and the environment, resulting in the small shock cells. Figure 4.8a shows that the wall velocity increases because of the lower pressure and thus the larger mean free path. When the drag is compared in Figure 4.8b, it can be seen that the shape is different because of the expansion waves, but the magnitudes are comparable. For f_{high} there was a huge difference between the initial and final pressure. So only increasing the pressure is not the only criterion to get better flushing results. It seems that the flow behind the nozzle should not expand to much, because a more focused jet cleans the surface more efficient. Furthermore a unsteady flow can induce very high gradients and thus large drag forces in a wide range.

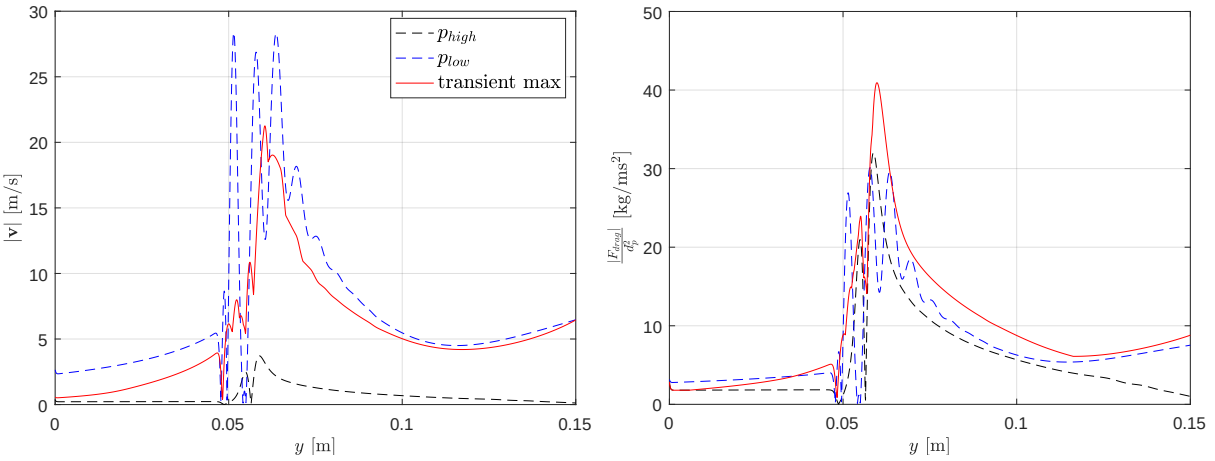

(a) **(b)**

Figure 4.8: *Wall velocity (a) and drag force on small spheres (b) along the contaminated surface for p_{high} (black dashed line), p_{low} (blue dashed line) and the maximum values during the transition (red solid line). The flowrate is taken constant at f_{low}.*

4.2 Optimum pressure

4.2.1 General analysis

In section 4.1 a complete flush sequence is analyzed using the results of a laminar solver. In this section different pressures (and flowrate f_{high}) are tested to find an optimum pressure for flushing the contaminated surface. The fluctuating flow features that are seen for p_{high} and f_{high} are suggesting that turbulence may play an important role. Calculating a Reynolds number is not straight forward, since the critical length dimension is hard to determine. However, in Figure 7.7 (Appendix) a local value is calculated using the width of the channel for p_{high}. In this figure high Reynolds values are shown, suggesting that turbulence will be present. To find the optimum pressure, higher pressures will be tested, which will increase the level of turbulence even more. To perform a correct analysis turbulence models should be tested as well. Subsections 2.1.3 and 2.1.4 described the $k-\epsilon$ and SST $k-\omega$ models, and these will be tested here. For laminar transient simulations the mean and maximum drag values are analyzed. As is described in subsection 3.2, the area under the drag force curve is summed as value for flush efficiency. The result of this analysis is shown in Figure 4.9. In this figure a general optimum pressure is found at 2500 Pa. The turbulence models and the averaged values are of course time averaged. This is the cause of the big difference between the maximum laminar curve and the other ones.

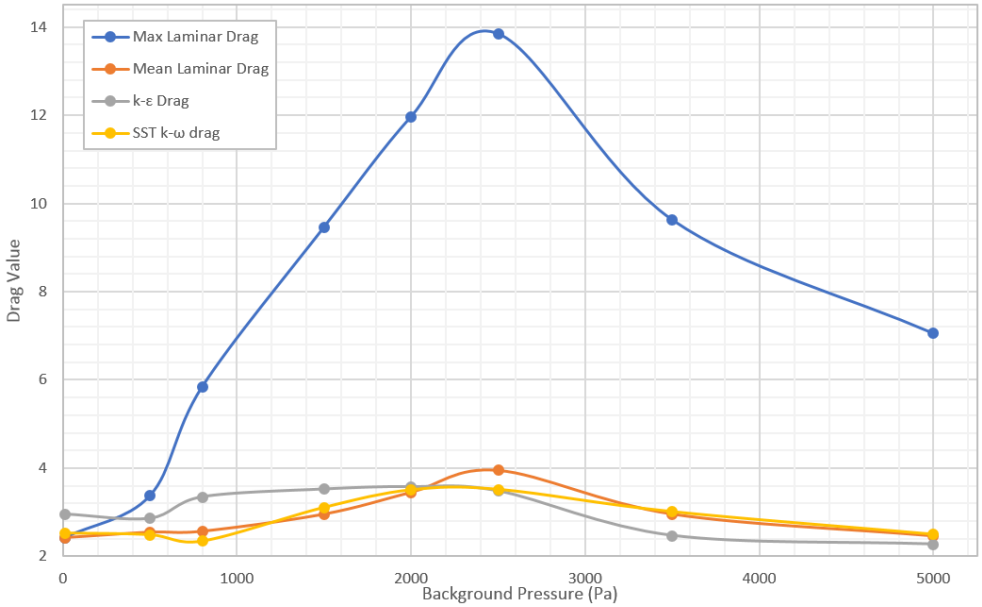

Figure 4.9: *The summed area under the drag force curves (Drag Value) versus different pressures for different models.*

All models are showing the same maximum, this suggests that this is the optimum background pressure for particle release. However, these models will perform not well for all investigated pressures. A closer look at the results is needed to determine if this maximum value can be implemented as the real optimum. At low background pressures the Reynolds value is low (Figure 7.6 (Appendix)), and the laminar flow simulation can be assumed as correct. If the background pressure is increased, higher Reynolds numbers are found. The $k-\epsilon$ turbulence model, is one of the most used models for turbulence modeling. This model can assumed as correct for confined flows, with low-pressure gradients. This is the case for 5000 Pa, and as can be seen in Figure 7.8 (Appendix), the Reynolds values are quite high in a large regime. As is described in subsection 2.1.4 the SST $k-\omega$ model should perform the best. This is qualitatively tested using the p_{low} laminar and 5000 Pa $k-\epsilon$ result. In Figures 7.9, 7.10, and 7.11 (Appendix) the simulated velocity

fields for p_{low}, 800, and 5000 Pa for different models are shown. These figures are indeed showing that the $k-\omega$ model is the best model for this research.

4.2.2 SST $k-\omega$ revisited

In subsection 4.2.1 it was discussed that the $k-\epsilon$ model has problems for high pressure gradients. On the contrary, the SST $k-\omega$ model handles high pressure gradients better as it is based on specific turbulent kinetic dissipation. In this subsection the results of the SST $k-\omega$ model are discussed in more detail.

The transient laminar simulations result in large fluctuations, that are translated in the high drag values, as can be seen in Figure 4.9. These fluctuations are of course questionable. They can be the result of numerical issues, like reflective boundaries. However, fluctuations for higher Reynolds numbers are expected, and can have a positive effect on the drag value. The SST $k-\omega$ results are hard to evaluate in terms of fluctuations since time averaged flow fields are simulated, while the fluctuations are critical for optimal particle release. From the results of the SST $k-\omega$ simulations in StarCCM+ a local turbulence intensity can be extracted. As is described in Basse (2017) a root-mean-square of the fluctuations with respect to the mean can be calculated using the turbulence intensity (I). The relation is given by

$$I = \frac{u_{RMS}}{u_{mean}}. \tag{4.1}$$

This u_{RMS} can be seen as a standard deviation of the fluctuations (σ). For the laminar simulations, 1000 velocity fields of different time steps are simulated, so a mean and a standard deviation using (4.1) can be be calculated. This makes it possible to compare the results of the laminar and SST $k-\omega$ model in order of fluctuations.

The results are shown in Figure 4.10. This figure shows that the fluctuations are less for low background pressures. For the SST $k-\omega$ results the fluctuations become significant large for pressures around 1500 Pa and above. Interesting to see is that this occurs for pressures around 500 Pa and above for the laminar results. This is most likely the result of the transient simulations of the chain with shock cells. In the ideal case these shock cells are steady and will not move. However, because of the transient simulations, these will move slightly by numerical inconsistencies. Since these chains of shocks result in a sinusoidal drag profile on the contaminated surface, this can lead to big differences in wall velocity at one position during time. In Figure 7.16 (Appendix) an example for 800 Pa is given. As can be seen in this figure, is that the sinusoidal profile (when it moves slightly), result in a more flatten average, while the maximum values are quite high. For the ideal case that is studied here the SST $k-\omega$ model is probably resulting in a better representation. However, in reality the system is not perfect and small distortions in the flow rate can result in the moving chain. Furthermore are the edges not perfectly sharp and the shock chain will be less present.

Furthermore, it can be seen that the laminar averaged values and the result of the SST $k-\omega$ are almost identic. Between the averages plus the standard deviations a large difference in magnitude is seen. In the paragraph above an explanation is given for the moving shock chain. For the higher pressure results another thing is remarkable, here large scale wavy flow features are observed. This can allready be seen in Figure 4.5, but in Figure 7.12 (Appendix) this is even more clear. These structures are resulting in high drag forces further downstream. The origin of these structures is questionable, this is most likely the result of the 2D approach. A major limitation of the 2D approach is that, the turbulence will be simulated in a 2D way if it is simulated with a laminar solver on a fine grid. 2D turbulence has typically a different energy cascade than 3D turbulence. In 3D turbulence the energy is tranfered from the large to the small scales, for 2D turbulence this is the opposite (see Boffetta and Ecke (2012)). These structures are likely an artifact of the simulation method and do not occur in reality.

From real tests before the trend of the number of particles that is found on a reticle after flushing versus maximum pressure is shown in Figure 7.17 (Appendix). In that study different pulsating flushes are done. As a result of the increased flowrate during these different pulse sequences the background pressure increased as well. Accidentally a linear trend of an increasing number of released particles for higher values of the maximum pressure is found. The result of the SST $k-\omega$ study in Figure 4.10 shows in this pressure range a same trend. This suggests that the analysis using the SST $k-\omega$ model is in agreement with the few test results that are present for higher pressures.

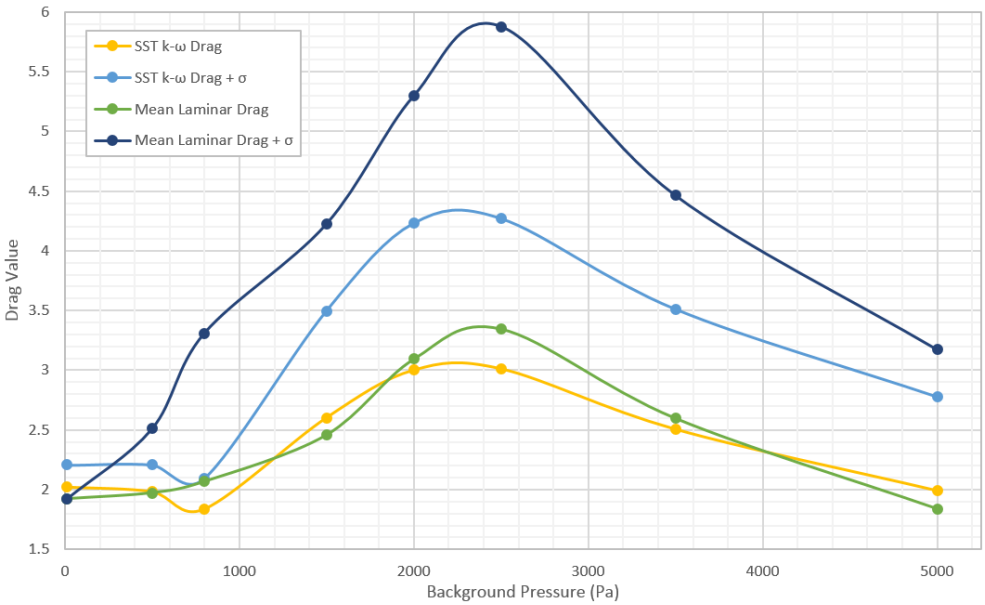

Figure 4.10: *The summed area under the drag force curves (Drag Value) versus different pressures for the laminar and SST $k-\omega$ model. The averages and the averages plus one standard deviation are plotted*

The main conclusion that can be drawn from Figure 4.10, is that the optimum background pressure for flushing this configuration is around 2250 Pa. It is important to find the cause of this optimum on a more fundamental level, such that it can also be applied to different geometries or other cases.

In section 4.1 is already discussed, that the higher pressure results in a more focused jet. In combination with the fluctuations as result of turbulence relatively high wall velocities are found, together with the high pressures this results in the high drag values. Increasing the pressure further will result in zero wall velocity and thus zero drag. This can be one argument why the Drag value is decreasing for higher pressures. The existence of a supersonic jet can play an important role in turbulence development as well. This will be discussed in more detail in subsection 4.2.3.

Two things that should be mentioned in order to see the limitations of the assumptions for the very low pressure flow, are the drag force and the wall slip. The drag force relation is derived

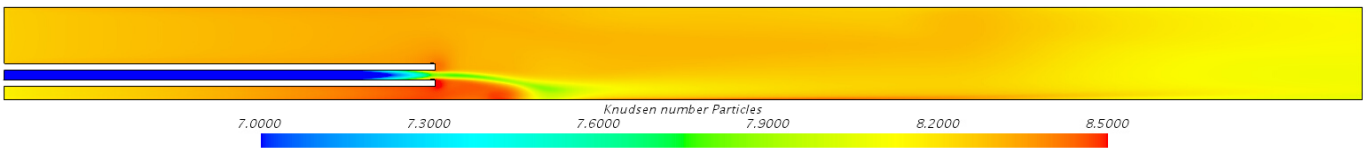

Figure 4.11: *Graphical representation of the spatial distribution of the particle Knudsen number for* 2000 nm *particles at* 5000 Pa. *Simulation is performed using the SST $k-\omega$ model.*

for very high particle Knudsen numbers. So is this assumption still correct for the 5000 Pa case? Typically particles with a diameter in the range 50-2000 nm are present in the scanner. For the 2000 nm particles the Knudsen number in the flow is plotted in Figure 4.11. In this figure is shown that the Knudsen numbers for the largest particles are relatively high on the contaminated surface. For smaller particles, that are the hardest to release, the Knudsen numbers are even higher. So the assumptions for the drag force relation are still valid, according to Figure 4.11 and 7.18 (Appendix).

Analyzing the slip assumptions, the general range where the Maxwell slip is correct is for $0.01 < Kn < 0.1$. For the Knudsen number a length scale is needed. Since the results are not typical channel flows, this is not straightforward the width of the channel. However, in Lockerby et al. (2005) the half of the width of the channel is used to calculated the Knudsen number. Using local properties of the SST $k-\omega$ simulations and the half of the width as length scale a Knudsen number can be calculated. In Figure 7.13 (Appendix) for different pressures the Knudsen number profiles are shown. For the low pressures the Maxwell slip condition is valid for sure. At 5000 Pa the Knudsen number is in principle too low to assume that the Maxwell slip condition is still completely valid. In this simulation wall velocities are still calculated using Maxwell slip, but these are probably overestimated. This does not change the optimum pressure, since the value is already much lower than the maximum. Around the optimum pressure, the Knudsen number is at the edge of the regime where the Maxwell slip condition is completely correct, but Hermadri et al. (2018) calculated the tangential accommodation factor also for lower values. So maybe the values are a slightly overestimated, but the general trend will still hold. A last interesting thing with respect to slip is that according to Figure 4.11 the mean free path is larger than the particles. Subsection 2.2 showed that the Maxwell slip condition is overestimating the actual slip that is used to derive a relation for drag force. This overestimation is the largest for the smallest particles and the largest mean free paths. In short, the Maxwell slip is probably not physical for the low channel Knudsen number, resulting in a overestimation. On the other hand is a very large particle Knudsen number resulting in an overestimation of the velocity that is hitting the particle. These overestimations are the largest for the lowest and highest pressures, which can make the optimum at 2500 Pa even clearer.

4.2.3 Supersonic jet analysis

This subsection will more closely examine the shock cells in the supersonic jet, and the effect of this jet with respect to turbulence formation. In section 2.5 a general explanation about a round supersonic jet in an inviscid gas is described. In that section a large reservoir with constant pressure in front of the nozzle is assumed. In the simulations that are done for this research the pressure build up in the nozzle can be used as a reservoir pressure. In this analysis the pressure (p_0) at 0.9 of the length of the nozzle is used, so this is almost at the end of the nozzle. (2.44) gives an expression for the length of the first shock cell for a round jet. In section 7.3 (Appendix) this relation is used to derive for a 2D plane jet that the length of the first shock cell is proportional to p_0/p_a.

p_a (Pa)	p_0 (Pa)	p_0/p_a	*Length* (m)	*width* (m)
500	4570	9.14	0.0123	0.0027
800	4940	6.18	0.0075	0.0017
1500	5253	3.50	0.0036	0.0009
2000	5350	2.68	0.0023	0.0006
2500	5390	2.16	0.0017	0.0005
3500	5144	1.47	-	-

Table 4.1: *Length and width of the first shock cell for different background pressure (p_a) and reservoir pressure (p_0).*

The lengths and widths of the first shock cells are presented in Table 4.1. The values for the two lowest pressures are not taken into account, since the walls influence the expansions too much. The two highest pressures have a ratio below 1.893, as is described in subsection 2.5 these simulations do not show shock cells. In Figure 4.12 the length and width of the shock cells are plotted versus the pressure ratio. Two linear relations are the result, and the corresponding equations are:

$$length = 0.0015\left(\frac{p_0}{p_a}\right) - 0.0018, \tag{4.2}$$

and

$$width = 0.0003\left(\frac{p_0}{p_a}\right) - 0.0002. \tag{4.3}$$

Using these equations a prediction of the length and width of the first shock cell can be made. If for example the critical surface in Figure 3.1 has to be cleaned, this will never happen at high background pressures for the analyzed configuration. For lower background pressures it is possible to create a large expansion that reaches the critical surface, and can clean it (of course not very effective).

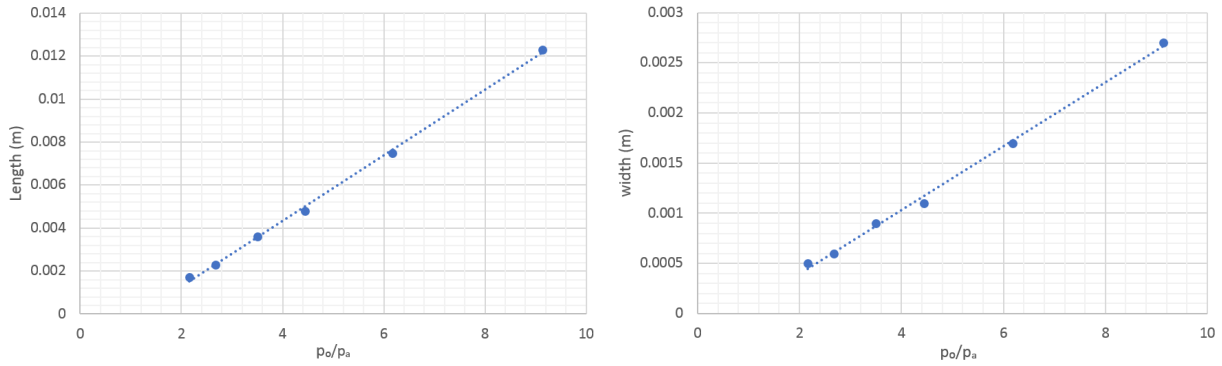

(a) **(b)**

Figure 4.12: *The length (a) and the width (b) of the first shock cell versus the pressure ratio. The dots are the simulation results and the dotted line is the best linear fit given by 4.2 and 4.3.*

As was already mentioned in subsection 4.2.2 the supersonic jet can play a role in the turbulence existence. Remarkable in Figure 4.10 is that the optimum pressure is found for a background pressure that is just low enough to get a supersonic jet. The core of the supersonic jet is relatively steady, and at the edges a large velocity jump is the result. These strong gradients result in velocity fields with a lot of shear, that produce turbulence. The balance between the strong velocity gradient as result of the supersonic jet and the higher density (higher pressure) results in a turbulence development on the lower side of the jet. This feature is captured in Figure 7.14 (Appendix). A hypothesis is that the jet is splitting up the channel in two areas, two Couette flows (Figure 4.13), so two local Reynolds numbers ($Re = \frac{\rho U_w h}{\mu}$), under and above the jet, are needed to say something about turbulence development (for more information see Bech et al. (1995)). At low pressure the velocity gradient (so wall speed in Figure 4.13) is high, but the density is too low to create turbulence below the jet. Above the jet the area of freedom is larger, and thus a larger critical length (h in Figure 4.13) results in a higher Reynolds number. This makes it possible to create turbulence above the jet (Figure 7.15a (Appendix)). Increasing the pressure in a way that a supersonic jet still exists (high gradients) result in more turbulence below the jet. This is only possible for the higher pressure, since this results in higher density that makes the Reynolds number higher, and turbulence can exist.

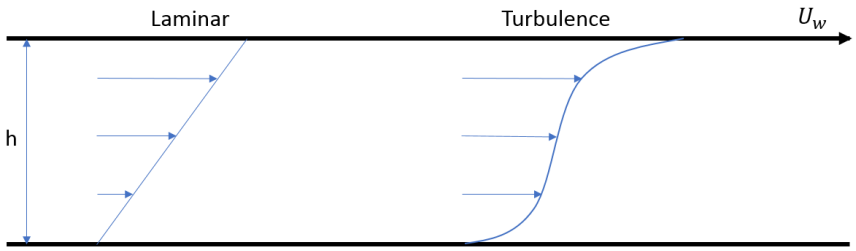

Figure 4.13: *Sketch of mean velocity profile for a laminar and a turbulent Couette flow. When Reynolds number ($Re = \frac{\rho U_w h}{\mu}$) becomes higher turbulence can occur.*

To get a more fundamental understanding of this feature, the Reynolds number as is described in Bech et al. (1995) is analyzed. The formula is given by

$$Re = \frac{\rho U_w h}{\mu} \sim \rho U_w. \tag{4.4}$$

If the area under the jet is analyzed, we can assume that the height (h) is constant, and the dynamic viscosity (μ) is dominated by the temperature, which can be assumed as constant as well. U_w is dependent on the mach value of the fully expanded gas, and the density is proportional to the background pressure, resulting in

$$Re \sim p_a Ma_{fe}, \tag{4.5}$$

where Ma_{fe} is given by (2.43). Substituting (2.43) in (4.5) results in

$$Re \sim p_a \left(\frac{2}{\gamma - 1}\right)^{\frac{1}{2}} \left(\left(\frac{p_0}{p_a}\right)^{\frac{\gamma-1}{\gamma}} - 1\right)^{\frac{1}{2}} \sim p_a \left(\left(\frac{p_0}{p_a}\right)^{\frac{\gamma-1}{\gamma}} - 1\right)^{\frac{1}{2}}. \tag{4.6}$$

Using the values from Table 4.1 the trend of the Reynolds number can be calculated. The trend is shown in Figure 4.14. For the very low background pressures the larger expansion decreases the height and the Reynolds number becomes even lower than is calculated. Interesting is to see that the same trend and optimum is found as for the total analysis of the simulations. When the pictures in Figure 7.14 (Appendix) are analyzed qualitatively the same optimum is found. This suggests that local turbulence development is playing a major role in flushing performance.

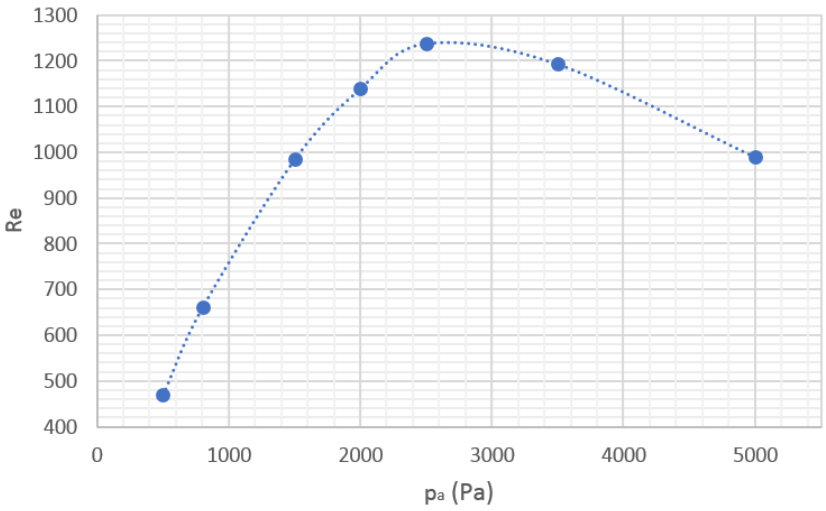

Figure 4.14: *Trend of Reynolds number versus background pressure, using the Couette flow assumption. The values form Table 4.1 are used*

In Figure 4.14, the pressure in the nozzle and the background pressure is used. Of course is the pressure in nozzle dependent of the flowrate and the background pressure. However, in the simulations the pressure build up in the nozzle is not straight forward, because for very low background pressure a supersonic jet is formed in the beginning of the nozzle. In principle is the pressure in the nozzle becoming higher for a higher background pressure. However, for now is focused on the fundamental relation 4.6, in which the pressures are used as inputs. In Figure 4.15 this relation is shown in a 3−dimensional plot. Figure 4.15a is showing that for a given nozzle pressure a optimum background pressure can be determined. To find this relation the partial derivative of Re with respect to p_a is set to zero,

$$\frac{\partial Re}{\partial p_a} = 0, \tag{4.7}$$

and this relation is solved for p_a. This derivation is done in section 7.4 (Appendix) and the result is

$$p_a = p_0 \left(\frac{\gamma + 1}{2\gamma} \right)^{\frac{\gamma}{\gamma - 1}}. \tag{4.8}$$

So using this relation for some nozzle pressure an optimum background pressure for the optimum flushing performance can be calculated. A side note with respect to Figure 4.15 is that (4.6) is plotted for all p_a and p_0 combinations. When the pressure ratio becomes higher, the width of the first shock cell in the supersonic jet (see (4.3)) will become larger and the Couette approach becomes less valid. For even higher values the shock cell will reach the lower surface and a different approach is needed. However, Figure 4.10 was showing that for large pressure differences (constant flowrate and low background pressure) the flow efficiency was not high for sure. So for large pressure differences the function (4.6) is not correct, although relation (4.8) is still valid.

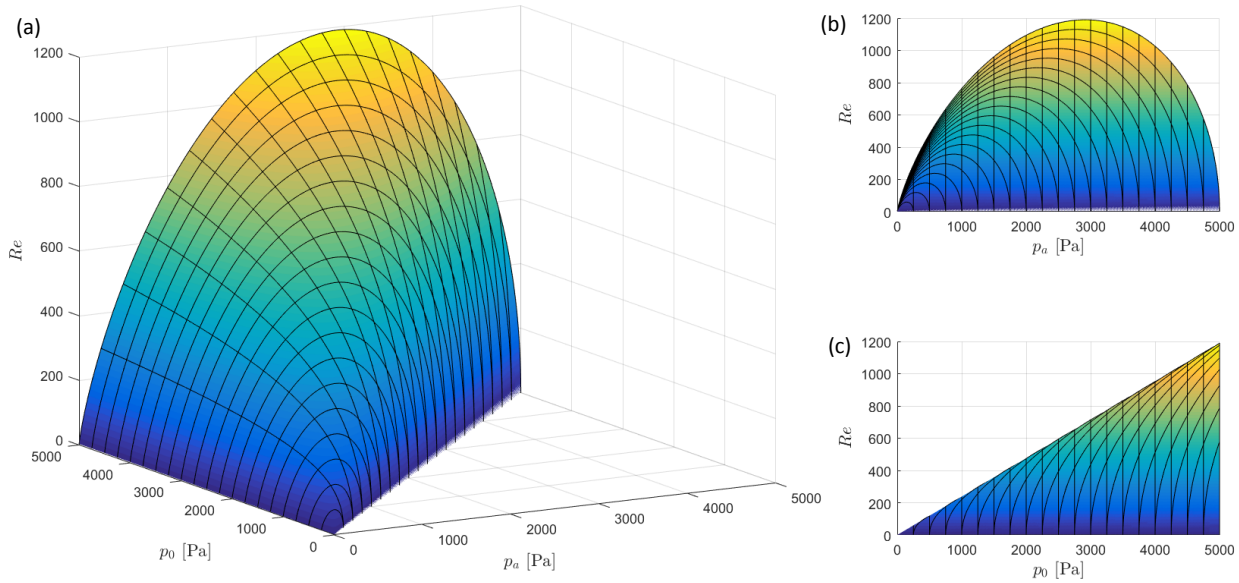

Figure 4.15: *(4.6) plotted in a 3−dimensional plot (a), together with two side views (b) and (c).*

Chapter 5

Conclusions

In this research the flowrate and background pressure are varied to study the flush efficiency of the contaminated surface using a parallel low-pressure jet. The particles on the surface that have to be released are very small and slip flow is required to get a significant drag force on these particles. This slip flow is achieved by flushing at low pressures. In this project the order of magnitude of the pressure is $10^2 - 10^3$ Pa. At these low pressures the Maxwell slip relation (2.24) is used to calculate the wall slip at the surfaces, and for the small particles the Stokes drag, corrected with the Cunningham correction factor (2.35) is used to calculate the particle drag force.

Firstly, the flush sequence as presented in section 3.2 is analyzed. The results show that a pulsating flow can have positive effects on flushing performance. However, the turbulent fluctuations as a result of the higher background pressure are playing a more dominant role. Another advantage of the higher pressure is a more focused jet that is attracted to the surface as a result of the Coanda effect.

In the next step, different pressures for a constant flowrate f_{high} are analyzed. The main conclusion is that for this particular flowrate the optimum background pressure is around 2500 Pa. The origin of the optimum is a result of multiple effects. For low pressures there is no focused jet and no turbulence, while at high pressures the wall slip will disappear and the large velocity gradients in the jet, which generate turbulence, will decrease.

In most simulations supersonic jets are formed as a result of a large expansion at the end of the nozzle. For every simulation the lengths and widths of the first shock cells are measured. Furthermore, the pressure ratio of the nozzle pressure (p_0) (result of flowrate and background pressure) and the background pressure (p_a) is calculated. It turns out that the lengths and widths of the shock cells are related linearly to the pressure ratios.

The simulations with large pressure differences result in large expansions that will only result in a very local high drag force. If the expansions become smaller, a Couette flow assumption is used to determine a Reynolds number in the area below the jet. The higher this value is, the more turbulent the flow will become. This local turbulence close to the contaminated surface results in a better flushing performance. The Reynolds number is related to the nozzle pressure and background pressure as $Re \sim p_a((\frac{p_0}{p_a})^{\frac{\gamma-1}{\gamma}} - 1)^{\frac{1}{2}}$. Using the values for the different background pressures and the corresponding simulated nozzle pressures a same trend is found as for the general flushing performance results. This shows that this Reynolds number (measure of the turbulence below the jet) is good a indicator for the flush efficiency.

When the Couette Reynolds number is analyzed it can be seen that: increasing p_0 results in higher values for Re, and for a certain value p_0 an optimum background pressure can be found. This value is given by $p_a = p_0(\frac{\gamma+1}{2\gamma})^{\frac{\gamma}{\gamma-1}}$.

In short, the most important result of this research is that the proposed pulsating way of flushing is likely not the most efficient. The assumption that most particles will be released at the lowest pressures does not seem to be correct. Of course slip flow as a result of low pressure is essential, but local turbulence that occurs at higher pressures plays a dominant role in the most

efficient way of flushing. This makes a pulsating flush sequence not necessary and a constant flowrate in combination with the optimal pressure can be sufficient. An additional advantage of the wall turbulence and higher pressures is that the particle entrainment and transport becomes more efficient.

5.1 Recommendations

The main goal of this research is flushing the contaminated surface as good as possible. As described here above, flushing in a pulsating way at very low pressures is not the most effective. The existence of local turbulence in combination with a slip flow, is the key to a high flush efficiency. For flowrate f_{high}, the pressure in the vacuum chamber has to be set around 2500 Pa.

In this report the focus is on cleaning the contaminated surface. However, it can be interesting to clean the surface above the nozzle as well. In the configuration analyzed in this report the upper surface is not cleaned at the higher background pressures. For lower background pressures the shock cells will reach and clean the surface above the nozzle, but this is not very effective. Another possibility at higher pressure is changing the configuration by removing the contaminated surface, which can be done in the scanner. Now the Coanda effect could work in the other direction and additional flow from below could make the jet reach the top surface and clean this efficiently. This indicates that hardware configurations can influence the cleaning behaviour and it is therefore recommended to investigate this further using computational methods.

In this research perfect conditions and models are used to do the analysis. To check if the results of the simulations are representing the reality, experimental validation should be performed. The results can be checked using a test where particles are counted downstream. For that purpose a particle counter downstream should be installed. Now particles can be counted during the pressure increase. The flowrate is set to f_{high} and at pressure p_{high} is started. Some time is needed for the system to adjust and when the signal of the particle counter becomes constant, the pressure will be increased step-wise. At every new pressure new particles can be released, resulting in a higher particle counter signal. When the particle counter signal becomes constant, the pressure is further increased. So it can be determined if at the new pressure new particles are released. When the particle counter signal does not increase at a new pressure, the optimum is around the last tested pressure. It is expected that for flowrate f_{high} the optimum pressure is around 2500 Pa.

Another possibility is to recreate the analyzed geometry in a test setup. This can provide more freedom in test parameters but it will take a significantly higher effort to develop. The highest benefit is that samples with a predetermined contamination could be used or contamination could be added on the sample within the setup. When this is done in a proper and consistent manner this can create more consistency and repeatability of the tests. Furthermore, it can give more insight in the adhesion force of the particles.

Chapter 6

References

Asproulias, I. (2014). *RANS Modelling for Compressible Turbulent Flows Involving Shock Wave Boundary Layer Interactions*. PhD thesis, School of Mechanical Aerospace and Civil Engineering, University of Manchester.

Bailey, C., Barber, R., Emerson, D., Lockerby, D., and Reese, J. (2005). A critical review of the drag force on a sphere in the transition flow regime. *AIP Conference Proceedings*, 762:743–748.

Basse, N. T. (2017). Turbulence intensity and the friction factor for smooth- and rough-wall pipe flow. *Fluids*, 2(2):30–42.

Bech, K., Tillmark, N., Alfredsson, H., and Andersson, H. (1995). An investigation of turbulent plane Couette flow at low Reynolds numbers. *Journal of Fluid Mechanics*, 286:291–325.

Boffetta, G. and Ecke, R. E. (2012). Two-dimensional turbulence. *Annual Review of Fluid Mechanics*, 44:427–451.

Brown, J. L. (2011). Shock wave impingement on boundary layers at hypersonic speeds: Computational analysis and uncertainty. In *42nd AIAA Thermophysics Conference, 27 - 30 June 2011, Honolulu, Hawaii*, June 2011. AIAA 2011-3143.

Buchmann, N. A., Atkinson, C., and Soria, J. (2013). Ultra-high-speed tomographic digital holographic velocimetry in supersonic particle-laden jet flows. *Measurement Science and Technology*, 24(2):024005.

Chaoui, M. and Feuillebois, F. (2003). Creeping flow around a sphere in a shear flow close to a wall. *The Quarterly Journal of Mechanics and Applied Mathematics*, 56(3):381–410.

Georgiadis, N. J., Yoder, D. A., and Engblom, W. B. (2006). Evaluation of modified two-equation turbulence models for jet flow predictions. *AIAA Journal*, 44(12):3107–3114.

Hamaker, H. C. (1937). The London-van der Waals attraction between spherical particles. *Physica*, 4(10):1058–1072.

Henry, C. and Minier, J.-P. (2014). Progress in particle resuspension from rough surfaces by turbulent flows. *Progress in Energy and Combustion Science*, 45:1–53.

Hermadri, V., Agrawal, A., and Bhandarkar, U. V. (2018). Determination of tangential momentum accommodation coefficient and slip coefficients for rarefied gas flow in a microchannel. *Sadhanda*, 43(10):164.

Israelachvili, J. N. (2011). *Intermolecular and Surface Forces*. Academic Press, 3 edition.

Kim, J. H., Mulholland, G. W., Kukuck, S. R., and Pui, D. Y. H. (2005). Slip correction measurements of certified psl nanoparticles using a nanometer differential mobility analyzer (nano-dma) for knudsen number from 0.5 to 83. *Journal of Research of the National Institute of Standards and Technology*, 110(1):31–54.

Kostić, O., Stefanović, Z., and Kostić, I. (2017). Comparative CFD analyses of a 2D supersonic nozzle flow with jet tab and jet vane. *Tehnički vjesnik*, 24(5):1335–1344.

LaMarche, C. Q., Leadley, S., Liu, P., Kellogg, K. M., and Hrenya, C. M. (2017). Method of quantifying surface roughness for accurate adhesive force predictions. *Chemical Engineering Science*, 158:140–153.

Launder, B. E. and Sharma, B. I. (1974). Application of the energy dissipation model of turbulence to the calculation of flow near a spinning disc. *Letters in Heat and Mass Transfer*, 1(2):131–138.

Lockerby, D. A., Reese, J. M., and Gallis, M. A. (2004). A wall-function approach to incorporating Knudsen-layer effects in gas micro flow simulations. In *Proceedings of the 24th International Symposium on Rarefied Gas Dynamics, Bari, Italy.*

Lockerby, D. A., Reese, J. M., and Gallis, M. A. (2005). The usefulness of higher-order constitutive relations for describing the Knudsen layer. *Physics of Fluids*, 17(10):100609.

Menter, F. (1993). Zonal two-equation $k - \omega$ turbulence model for aerodynamic flows. In *24th Fluid Dynamics Conference, 6 - 9 July 1993, Orlando, Florida*, July 1993, AIAA 93-2906.

Menter, F. (1994). Two-equation eddy-viscosity turbulence models for engineering applications. *AIAA Journal*, 32:1598–1605.

Nieuwstadt, F. (2016). *Turbulentie - theorie en toepassingen van turbulente stromingen.* Epsilon Uitgaven Amsterdam, 4th edition.

Powell, A. (1988). The sound-producing oscillations of round underexpanded jets impinging on normal plates. *The Journal of the Acoustical Society of America*, 83(2):515–533.

Prandtl, L. (1904). Über die stationären Wellen in einem Gasstrahl. *Zeitschrift für Physik*, 5:559–601.

Rabinovich, Y. I., Adler, J. J., Ata, A., Singh, R. K., and Moudgil, B. M. (2000a). Adhesion between nanoscale rough surfaces: I. role of asperity geometry. *Journal of Colloid and Interface Science*, 232(1):10–16.

Rabinovich, Y. I., Adler, J. J., Ata, A., Singh, R. K., and Moudgil, B. M. (2000b). Adhesion between nanoscale rough surfaces: II. measurement and comparison with theory. *Journal of Colloid and Interface Science*, 232(1):17–24.

Schlichting, H., Kestin, J., and Street, R. L. (1980). *Boundary-Layer Theory.* McGraw-Hill book company, 7th edition.

Tadmor, R. (2001). The London-van der Waals interaction energy between objects of various geometries. *Journal of Physics: Condensed Matter*, 13(9):195–202.

Wille, R. and Fernholz, H. (1965). Report on the first European Mechanics Colloquium, on the Coanda effect. *Journal of Fluid Mechanics*, 23(4):801–819.

Chapter 7

Appendix

7.1 Compressible turbulence

To simulate the mean flow fields for compressible turbulence, equations (2.1), (2.3), and (2.6) should be decomposed and time averaged. Two kinds of decompositions are used and the averaging rules will be discussed in the following subsection. These decompositions are used to derive the mean momentum, mean energy, and mean turbulent kinetic energy equations.

7.1.1 Reynolds and Favre averaging

The Reynolds decomposition of variable Φ is

$$\Phi = \overline{\Phi} + \Phi', \tag{7.1}$$

with $\overline{\Phi} = \frac{1}{T}\int_T \Phi(t)\mathrm{d}t$. The following relations are valid with respect of averaging

$$\overline{\Phi_1 + \Phi_2} = \overline{\Phi_1} + \overline{\Phi_2}, \tag{7.2a}$$

$$\overline{a\Phi} = a\overline{\Phi}, \text{ where } a = \text{constant}, \tag{7.2b}$$

$$\overline{\left(\frac{\partial\Phi}{\partial s}\right)} = \frac{\partial\overline{\Phi}}{\partial s}, \tag{7.2c}$$

$$\overline{\overline{\Phi}_1\overline{\Phi}_2} = \overline{\Phi}_1\overline{\Phi}_2, \tag{7.2d}$$

$$\overline{\Phi'} = 0, \tag{7.2e}$$

$$\overline{\left(\overline{\Phi}_1\Phi'_2\right)} = 0. \tag{7.2f}$$

The Favre decomposition of variable Φ is

$$\Phi = \widetilde{\Phi} + \Phi'', \tag{7.3}$$

with $\widetilde{\Phi} = \frac{\int_T \rho(t)\Phi(t)\mathrm{d}t}{\int_T \rho(t)\mathrm{d}t} = \frac{\overline{\rho\Phi}}{\overline{\rho}}$. (7.2a), (7.2b), (7.2c), and (7.2d) and the following relations are valid with respect of averaging

$$\overline{\rho\Phi''} = 0, \tag{7.4a}$$

$$\overline{\rho\widetilde{\Phi}} = \overline{\rho}\widetilde{\Phi} = \overline{\rho\Phi}. \tag{7.4b}$$

7.1.2 Momentum equation

The original conservation of momentum equation is

$$\frac{\partial(\rho u_i)}{\partial t} + \frac{\partial(\rho u_i u_j)}{\partial x_j} + \frac{\partial p}{\partial x_j} - \frac{\partial \tau_{ij}}{\partial x_j} = 0. \tag{7.5}$$

Now u, p, and τ_{ij} are decomposed, and the total equation is time-averaged, resulting in

$$\overline{\frac{\partial}{\partial t}(\rho(\widetilde{u_i} + u_i'')) + \frac{\partial}{\partial x_j}(\rho(\widetilde{u_i} + u_i'')(\widetilde{u_j} + u_j'')) + \frac{\partial(\overline{p} + p')}{\partial x_j} - \frac{\partial(\widetilde{\tau_{ij}} + \tau_{ij}'')}{\partial x_j}} = 0, \tag{7.6}$$

which can be rewritten as

$$\frac{\partial}{\partial t}(\overline{\rho\widetilde{u_i}} + \overline{\rho u_j''}) + \frac{\partial}{\partial x_j}(\overline{\rho\widetilde{u_j}\widetilde{u_i}} + \overline{\widetilde{u_j}\rho u_i''} + \overline{\widetilde{u_i}\rho u_j''} + \overline{\rho u_i'' u_j''}) = -\frac{\partial}{\partial x_j}(\overline{\overline{p}} + \overline{p'}) + \frac{\partial}{\partial x_j}(\overline{\widetilde{\tau_{ij}}} + \overline{\tau_{ij}''}) \tag{7.7}$$

Using the averaging relations of subsection 7.1.1, some terms will be zero and this equation can be written as

$$\frac{\partial(\overline{\rho}\widetilde{u_i})}{\partial t} + \frac{\partial(\overline{\rho}\widetilde{u_i}\widetilde{u_j})}{\partial x_j} + \frac{\partial(\overline{\rho u_i'' u_j''})}{\partial x_j} = -\frac{\partial \overline{p}}{\partial x_j} + \frac{\partial \widetilde{\tau_{ij}}}{\partial x_j} + \frac{\partial \overline{\tau_{ij}''}}{\partial x_j}. \tag{7.8}$$

7.1.3 Energy equation

Since the derivation is quite long the energy equation is subdivided in a couple of parts. The original energy equation is given by

$$\underbrace{\frac{\partial(\rho E)}{\partial t} + \frac{\partial(\rho u_j E)}{\partial x_j} + \frac{\partial(u_j p)}{\partial x_j}}_{1} \underbrace{- \frac{\partial(u_i \tau_{ij})}{\partial x_j}}_{2} \underbrace{+ \frac{\partial q_j}{\partial x_j}}_{3} = 0. \tag{7.9}$$

First part 1 is decomposed and time averaged. For E and u the Favre decomposition is used and for p the Reynolds decomposition. The result is

$$\overline{\frac{\partial(\rho(\widetilde{E} + E''))}{\partial t}} + \overline{\frac{\partial(\rho(\widetilde{u_j} + u_j'')(\widetilde{E} + E''))}{\partial x_j}} + \overline{\frac{\partial(\widetilde{u_j} + u_j'')(\overline{p} + p')}{\partial x_j}}. \tag{7.10}$$

This can be written as

$$\frac{\partial(\overline{\rho\widetilde{E}} + \overline{\rho E''})}{\partial t} + \frac{\partial(\overline{\rho\widetilde{u_j}\widetilde{E}} + \overline{\widetilde{u_j}\rho E''} + \overline{\rho u_j''\widetilde{E}} + \overline{\rho u_j'' E''})}{\partial x_j} + \frac{\partial(\overline{\widetilde{u_j}\overline{p}} + \overline{\widetilde{u_j}p'} + \overline{u_j''\overline{p}} + \overline{u_j''p'})}{\partial x_j}. \tag{7.11}$$

Using (7.2e), (7.4a), and (7.4b) it can be seen that many of the terms are zero. This results in

$$\frac{\partial(\overline{\rho}\widetilde{E})}{\partial t} + \frac{\partial(\overline{\rho}\widetilde{u_j}\widetilde{E})}{\partial x_j} + \frac{\partial(\widetilde{u_j}\overline{p})}{\partial x_j} + \frac{\partial(\overline{u_j''p} + \overline{\rho u_j'' E''})}{\partial x_j}. \tag{7.12}$$

The rightmost term between brackets ($\overline{u_j''p} + \overline{\rho u_j'' E''}$) can be rewritten by using the ideal gas law for the pressure ($p = \rho RT$). Furthermore, a closer look at E'' is needed. E is given by $E = C_v T + \frac{u_i^2}{2}$, and after the decompositions of T and u_i are substituted, this results in

$$E = C_v(\widetilde{T} + T'') + \frac{(\widetilde{u_i} + u_i'')(\widetilde{u_i} + u_i'')}{2} = C_v\widetilde{T} + C_v T'' + \frac{\widetilde{u_i}^2}{2} + \frac{u_i''^2}{2} + u_i''\widetilde{u_i}. \tag{7.13}$$

Favre averaging of the relations results in

$$\widetilde{E} = C_v\widetilde{T} + \frac{\widetilde{u_i}^2}{2} + \frac{\widetilde{u_i''u_i''}}{2}. \tag{7.14}$$

Now a relation for E'' can be derived:

$$E'' = E - \widetilde{E} = C_v T'' + u_i''\widetilde{u_i} + \frac{u_i''^2}{2} + \frac{\widetilde{u_i''u_i''}}{2}. \tag{7.15}$$

Putting this and the decomposition of the ideal gas law in $\overline{u_j''p} + \overline{\rho u_j''E''}$ results in

$$\begin{aligned}\overline{u_j''p} + \overline{\rho u_j''E''} &= \overline{u_j''\rho R(\widetilde{T} + T'')} + \overline{\rho u_j'' C_v T''} + \overline{\rho u_j'' u_i'' \widetilde{u_i}} + \overline{\rho u_j'' \frac{u_i''u_i''}{2}} + \overline{\rho u_j'' \frac{\widetilde{u_i''u_i''}}{2}} \\ &= R\overline{\rho u_j'' T''} + R\widetilde{T}\,\overline{\rho u_j''} + C_v\overline{\rho u_j'' T''} + \widetilde{u_i}\overline{\rho u_j'' u_i''} + \frac{\overline{\rho u_j'' u_i'' u_i''}}{2} + \frac{\widetilde{u_i''u_i''}}{2}\overline{\rho u_j''}.\end{aligned} \tag{7.16}$$

(7.4a) implies that some of the terms become zero. Using the relation $R = C_p - C_v$, (7.16) can be written as

$$C_p\overline{\rho u_j'' T''} + \widetilde{u_i}\overline{\rho u_j'' u_i''} + \frac{\overline{\rho u_j'' u_i'' u_i''}}{2}. \tag{7.17}$$

Now the time average of $u_i\tau_{ij}$ ($\overline{u_i\tau_{ij}}$) in term 2 of (7.9) can be rewritten using the decomposition in the following way

$$\begin{aligned}\overline{u_i\tau_{ij}} &= \overline{(\widetilde{u_i} + u'')(\widetilde{\tau_{ij}} + \tau_{ij}'')} \\ &= \overline{\widetilde{u_i}\widetilde{\tau_{ij}}} + \overline{\widetilde{u_i}\tau_{ij}''} + \overline{u_i''\widetilde{\tau_{ij}}} + \overline{u_i''\tau_{ij}''} \\ &= \widetilde{u_i}\widetilde{\tau_{ij}} + \widetilde{u_i}\overline{\tau_{ij}''} + \overline{u_i''(\widetilde{\tau_{ij}} + \tau_{ij}'')} \\ &= \widetilde{u_i}\widetilde{\tau_{ij}} + \widetilde{u_i}\overline{\tau_{ij}''} + \overline{u_i''\tau_{ij}}.\end{aligned} \tag{7.18}$$

Now $\overline{q_j}$ in term 3 in (7.9) can be rewritten using the decomposition in the following way

$$\overline{q_j} = -\overline{C_p\frac{\mu}{Pr}\frac{\partial T}{\partial x_j}} = -C_p\frac{\mu}{Pr}\frac{\partial\widetilde{T}}{\partial x_j} - C_p\frac{\mu}{Pr}\frac{\partial\overline{T''}}{\partial x_j}, \tag{7.19}$$

with Pr the Prandtl number. Putting (7.17), (7.18), and (7.19) into (7.9) results in

$$\begin{aligned}&\frac{\partial(\overline{\rho}\widetilde{E})}{\partial t} + \frac{\partial(\overline{\rho}\widetilde{u_j}\widetilde{E})}{\partial x_j} + \frac{\partial(\widetilde{u}_j\overline{p})}{\partial x_j} + \frac{\partial}{\partial x_j}\Bigg(\underbrace{C_p\overline{\rho u_j''T''}}_{4} + \widetilde{u_i}\overline{\rho u_j''u_i''} + \underbrace{\frac{\overline{\rho u_j''u_i''u_i''}}{2}}_{5}\Bigg) \\ &\quad + \frac{\partial}{\partial x_j}\Bigg(\underbrace{-C_p\frac{\mu}{Pr}\frac{\partial\widetilde{T}}{\partial x_j}}_{6}\underbrace{-C_p\frac{\mu}{Pr}\frac{\partial\overline{T''}}{\partial x_j}}_{7}\Bigg) - \frac{\partial}{\partial x_j}(\widetilde{u_i}\widetilde{\tau_{ij}} + \underbrace{\widetilde{u_i}\overline{\tau_{ij}''}}_{8} + \underbrace{\overline{\tau_{ij}u_i''}}_{9}) = 0.\end{aligned} \tag{7.20}$$

Terms 5 and 8 describe turbulent transport and molecular diffusion of turbulent energy. These terms can be neglected if the turbulent kinetic energy is small compared with the enthalpy ($C_p\widetilde{T}$), which is a good approximation for almost all flows below the hyper-sonic regime. Term 9 can be neglected as well when $|\widetilde{\tau}_{ij}| \gg |\overline{\tau_{ij}''}|$, which is normally correct. In general $|\frac{\partial^2\widetilde{T}}{\partial x_j^2}| \gg |\frac{\partial^2\overline{T''}}{\partial x_j^2}|$, so term 7 can also be neglected. Term 4 can be seen as the turbulent heat flux (q_{t_j}) and term 6 is the laminar heat flux (q_{l_j}). The total relation is

$$\frac{\partial(\overline{\rho}\widetilde{E})}{\partial t} + \frac{\partial(\overline{\rho}\widetilde{u_j}\widetilde{E})}{\partial x_j} + \frac{\partial(\widetilde{u}_j\overline{p})}{\partial x_j} + \frac{\partial}{\partial x_j}(q_{t_j} + q_{l_j}) + \frac{\partial}{\partial x_j}(\widetilde{u_i}\overline{\rho u_j''u_i''} - \widetilde{u_i}\widetilde{\tau_{ij}}) = 0. \tag{7.21}$$

7.1.4 Mean turbulent kinetic energy

In this section we consider the mean turbulent kinetic energy equation. Equations (2.1) and (2.3) form the starting point of the analysis. These equations are, the continuity equation:

$$\frac{\partial \rho}{\partial t} + \frac{\partial}{\partial x_j}(\rho u_j) = 0, \tag{7.22}$$

and the momentum equation:

$$\underbrace{\frac{\partial}{\partial t}(\rho u_i) + \frac{\partial}{\partial x_j}(\rho u_i u_j)}_{1} = \underbrace{-\frac{\partial p}{\partial x_j}}_{2} + \underbrace{\frac{\partial}{\partial x_j}\tau_{ij}}_{3}. \tag{7.23}$$

First, term 1 of (7.23) is rewritten as

$$\rho\frac{\partial u_i}{\partial t} + u_i\frac{\partial \rho}{\partial t} + \rho u_j\frac{\partial u_i}{\partial x_j} + u_i\frac{\partial(\rho u_j)}{\partial x_i} = \rho\frac{\partial u_i}{\partial t} + \rho u_j\frac{\partial u_i}{\partial x_j} + u_i\left(\frac{\partial \rho}{\partial t} + \frac{\partial(\rho u_j)}{\partial x_i}\right). \tag{7.24}$$

According to (7.22) the part between the brackets is equal to zero. The result is

$$\rho\frac{\partial u_i}{\partial t} + \rho u_j\frac{\partial u_i}{\partial x_j}. \tag{7.25}$$

Now u_i in (7.25) is decomposed using the Favre averaging and the result is multiplied with u_i'', resulting in

$$\rho u_i''\frac{\partial(\widetilde{u}_i + u_i'')}{\partial t} + \rho u_j u_i''\frac{\partial(\widetilde{u}_i + u_i'')}{\partial t} = \rho u_i''\frac{\partial \widetilde{u}_i}{\partial t} + \rho u_i''\frac{\partial u_i''}{\partial t} + \rho u_j u_i''\frac{\partial \widetilde{u}_i}{\partial x_j} + \rho u_j u_i''\frac{\partial u_i''}{\partial x_j}. \tag{7.26}$$

Using the mathematical relation, $\frac{1}{2}\frac{\partial u_i''^2}{\partial s} = u_i''\frac{\partial u_i''}{\partial s}$ (s can be t and x_j), the right hand side of (7.26) can be written as

$$\rho\frac{\partial\left(\frac{u_i''^2}{2}\right)}{\partial t} + \rho u_i''\frac{\partial \widetilde{u}_i}{\partial t} + \rho u_j u_i''\frac{\partial \widetilde{u}_i}{\partial x_j} + \rho u_j\frac{\partial\left(\frac{u_i''^2}{2}\right)}{\partial x_j}. \tag{7.27}$$

The next step is multiplying (7.22) with $\frac{u_i''^2}{2}$ and adding this to (7.27). This is equivalent to adding zero to (7.27); this seems a strange step, but it makes the final notation shorter. The result is

$$\underbrace{\rho\frac{\partial\left(\frac{u_i''^2}{2}\right)}{\partial t} + \frac{u_i''^2}{2}\frac{\partial \rho}{\partial t}}_{4} + \rho u_i''\frac{\partial \widetilde{u}_i}{\partial t} + \rho u_j u_i''\frac{\partial \widetilde{u}_i}{\partial x_j} + \underbrace{\rho u_j\frac{\partial\left(\frac{u_i''^2}{2}\right)}{\partial x_j} + \frac{u_i''^2}{2}\frac{\partial(\rho u_j)}{\partial x_j}}_{5}. \tag{7.28}$$

A mathematical procedure can be applied to terms 4 and 5 of (7.28). For term 4 this is

$$\frac{\partial\left(\rho\frac{u_i''^2}{2}\right)}{\partial t} = \rho\frac{\partial\left(\frac{u_i''^2}{2}\right)}{\partial t} + \frac{u_i''^2}{2}\frac{\partial \rho}{\partial t}. \tag{7.29}$$

When this is applied to terms 4 and 5, (7.28) can be written as

$$\frac{\partial\left(\rho\frac{u_i''^2}{2}\right)}{\partial t} + \rho u_i''\frac{\partial \widetilde{u}_i}{\partial t} + \rho u_j u_i''\frac{\partial \widetilde{u}_i}{\partial x_j} + \frac{\partial\left(\rho u_j\frac{u_i''^2}{2}\right)}{\partial x_j}. \tag{7.30}$$

Now u_j is decomposed using the Favre averaging, and the whole relation is time-averaged. This will be simplified using the relations of subsection 7.1.1. This results in

$$\overline{\frac{\partial\left(\rho\frac{u_i''^2}{2}\right)}{\partial t}+\rho u_i''\frac{\partial\widetilde{u}_i}{\partial t}+\rho(\widetilde{u}_j+u_j'')u_i''\frac{\partial\widetilde{u}_i}{\partial x_j}+\frac{\partial\left(\rho(\widetilde{u}_j+u_j'')\frac{u_i''^2}{2}\right)}{\partial x_j}}=$$

$$\frac{\partial\left(\overline{\rho\frac{u_i''^2}{2}}\right)}{\partial t}+\overline{\rho u_i''}\frac{\partial\widetilde{u}_i}{\partial t}+\widetilde{u}_j\overline{\rho u_i''}\frac{\partial\widetilde{u}_i}{\partial x_j}+\overline{\rho u_j''u_i''}\frac{\partial\widetilde{u}_i}{\partial x_j}+\frac{\partial\left(\widetilde{u}_j\overline{\rho\frac{u_i''^2}{2}}\right)}{\partial x_j}+\frac{\partial\left(\overline{\rho u_j''\frac{u_i''^2}{2}}\right)}{\partial x_j}=$$

$$\frac{\partial\left(\overline{\rho\frac{u_i''^2}{2}}\right)}{\partial t}+\overline{\rho u_j''u_i''}\frac{\partial\widetilde{u}_i}{\partial x_j}+\frac{\partial\left(\widetilde{u}_j\overline{\rho\frac{u_i''^2}{2}}\right)}{\partial x_j}+\frac{\partial\left(\overline{\rho u_j''\frac{u_i''^2}{2}}\right)}{\partial x_j}=$$

$$\frac{\partial(\overline{\rho}k)}{\partial t}+\frac{\partial(\overline{\rho}\widetilde{u}_jk)}{\partial x_j}+\overline{\rho u_j''u_i''}\frac{\partial\widetilde{u}_i}{\partial x_j}+\frac{\partial\left(\overline{\rho u_j''\frac{u_i''^2}{2}}\right)}{\partial x_j},\tag{7.31}$$

where $k=\frac{\overline{\rho u_i''u_i''}}{2\overline{\rho}}$ is the mean turbulent kinetic energy.

Now term 2 of (7.23) is analyzed. For p the Reynolds decomposition is substituted. This part should also be multiplied with u_i'' and time-averaged. The result is

$$\overline{-u_i''\frac{\partial(\overline{p}+p')}{\partial x_i}}=-\overline{u_i''}\frac{\partial\overline{p}}{\partial x_i}-\overline{u_i''\frac{\partial p'}{\partial x_i}}.\tag{7.32}$$

The last term on the right-hand side can be rewritten using relation (7.29), resulting in

$$-\overline{u_i''\frac{\partial p'}{\partial x_i}}=\overline{p'\frac{\partial u_i''}{\partial x_i}}-\frac{\partial(\overline{u_i''p'})}{\partial x_i}.\tag{7.33}$$

The last term that should be discussed is term 3 of (7.23). In this part τ_{ij} can be decomposed, but normally this is not done in literature, since the terms with τ_{ij} are modeled with other quantities (see subsection 2.1.2). However this term should be multiplied with u_i'' and time averaged, resulting in

$$\overline{u_i''\frac{\partial\tau_{ij}}{\partial x_j}}=\frac{\partial(\overline{\tau_{ij}u_i''})}{\partial x_j}-\overline{\tau_{ij}\frac{\partial u_i''}{\partial x_j}},\tag{7.34}$$

again relation (7.29) is used.

Putting the results of (7.31), (7.32), (7.33), and (7.34) together, results in the following equation for the mean turbulent kinetic energy

$$\begin{aligned}\frac{\partial}{\partial t}(\overline{\rho}k)+\frac{\partial}{\partial x_j}(\overline{\rho}\widetilde{u}_jk)=&-\overline{\rho u_i''u_j''}\frac{\partial\widetilde{u}_i}{\partial x_j}-\overline{\tau_{ij}\frac{\partial u_i''}{\partial x_j}}+\frac{\partial}{\partial x_j}(\overline{\tau_{ij}u_i''})\\&-\frac{\partial}{\partial x_j}\left(\overline{\rho u_j''\frac{1}{2}u_i''u_i''}+\overline{p'u_j''}\right)+\overline{p'\frac{\partial u_i''}{\partial x_i}}-\overline{u_i''}\frac{\partial\overline{p}}{\partial x_i}.\end{aligned}\tag{7.35}$$

7.2 $k-\epsilon$ in terms of ω

To describe the transport equation of the rate of dissipation in terms of specific turbulent kinetic dissipation, first (2.14) is presented again

$$\frac{\partial}{\partial t}(\overline{\rho}\epsilon)+\frac{\partial}{\partial x_j}(\overline{\rho}\widetilde{u_j}\epsilon)=-\overline{\rho u_i'' u_j''}C_{\epsilon 1}\frac{\epsilon}{k}\frac{\partial \widetilde{u_i}}{\partial x_j}-C_{\epsilon 2}\overline{\rho}\frac{\epsilon^2}{k}+\frac{\partial}{\partial x_j}\left(\left(\mu+\frac{\mu_t}{\sigma_\epsilon}\right)\frac{\partial \epsilon}{\partial x_j}\right). \tag{7.36}$$

Now $\epsilon=\beta^* k\omega$ is substituted in this relation. Firstly, the left hand side of (7.36) is analyzed and can be written as

$$\begin{aligned}\frac{\partial}{\partial t}(\overline{\rho}\beta^*k\omega)+\frac{\partial}{\partial x_j}(\overline{\rho}\widetilde{u_j}\beta^*k\omega)&=\beta^*\left(k\frac{\partial}{\partial t}(\overline{\rho}\omega)+\overline{\rho}\omega\frac{\partial k}{\partial t}+k\frac{\partial}{\partial x_j}(\overline{\rho}\widetilde{u_j}\omega)+\overline{\rho}\widetilde{u_j}\omega\frac{\partial k}{\partial x_j}\right)\\&=\beta^*\Bigg(k\frac{\partial}{\partial t}(\overline{\rho}\omega)+k\frac{\partial}{\partial x_j}(\overline{\rho}\widetilde{u_j}\omega)+\underbrace{\overline{\rho}\omega\frac{\partial k}{\partial t}+\overline{\rho}\widetilde{u_j}\omega\frac{\partial k}{\partial x_j}}_{1}\Bigg).\end{aligned} \tag{7.37}$$

Term 1 can be rewritten using the product rule as

$$\begin{aligned}\overline{\rho}\omega\frac{\partial k}{\partial t}+\overline{\rho}\widetilde{u_j}\omega\frac{\partial k}{\partial x_j}&=\omega\left(\overline{\rho}\frac{\partial k}{\partial t}+\overline{\rho}\widetilde{u_j}\frac{\partial k}{\partial x_j}\right)\\&=\omega\left(\frac{\partial}{\partial t}(\overline{\rho}k)-k\frac{\partial \overline{\rho}}{\partial t}+\frac{\partial}{\partial x_j}(\overline{\rho}\widetilde{u_j}k)-k\frac{\partial}{\partial x_j}(\overline{\rho}\widetilde{u_j})\right)\\&=\omega\Bigg(\frac{\partial}{\partial t}(\overline{\rho}k)+\frac{\partial}{\partial x_j}(\overline{\rho}\widetilde{u_j}k)-k\Bigg(\underbrace{\frac{\partial \overline{\rho}}{\partial t}+\frac{\partial}{\partial x_j}(\overline{\rho}\widetilde{u_j})}_{2}\Bigg)\Bigg),\end{aligned} \tag{7.38}$$

where term 2 is exactly (2.8) and thus zero. So when $\epsilon=\beta^*k\omega$ is substituted in (7.36) this results in

$$\begin{aligned}\beta^*\left(k\frac{\partial}{\partial t}(\overline{\rho}\omega)+k\frac{\partial}{\partial x_j}(\overline{\rho}\widetilde{u_j}\omega)+\omega\frac{\partial}{\partial t}(\overline{\rho}k)+\omega\frac{\partial}{\partial x_j}(\overline{\rho}\widetilde{u_j}k)\right)=&\\-\overline{\rho u_i'' u_j''}C_{\epsilon 1}\frac{\beta^*k\omega}{k}\frac{\partial \widetilde{u_i}}{\partial x_j}-C_{\epsilon 2}\overline{\rho}\frac{(\beta^*k\omega)^2}{k}+\frac{\partial}{\partial x_j}\left(\left(\mu+\frac{\mu_t}{\sigma_\epsilon}\right)\frac{\partial}{\partial x_j}(\beta^*k\omega)\right),&\end{aligned} \tag{7.39}$$

or

$$\begin{aligned}\frac{\partial}{\partial t}(\overline{\rho}\omega)+\frac{\partial}{\partial x_j}(\overline{\rho}\widetilde{u_j}\omega)+\frac{\omega}{k}\Bigg(\underbrace{\frac{\partial}{\partial t}(\overline{\rho}k)+\frac{\partial}{\partial x_j}(\overline{\rho}\widetilde{u_j}k)}_{3}\Bigg)=&\\-\overline{\rho u_i'' u_j''}C_{\epsilon 1}\frac{\omega}{k}\frac{\partial \widetilde{u_i}}{\partial x_j}-C_{\epsilon 2}\overline{\rho}\beta^*\omega^2+\frac{1}{k}\frac{\partial}{\partial x_j}\left(\left(\mu+\frac{\mu_t}{\sigma_\epsilon}\right)\left(k\frac{\partial \omega}{\partial x_j}+\omega\frac{\partial k}{\partial x_j}\right)\right).&\end{aligned} \tag{7.40}$$

(2.12) can be substituted for term 3, which results in

$$\begin{aligned}\frac{\partial}{\partial t}(\overline{\rho}\omega)+\frac{\partial}{\partial x_j}(\overline{\rho}\widetilde{u_j}\omega)+\frac{\omega}{k}\left(-\overline{\rho u_i'' u_j''}\frac{\partial \widetilde{u_i}}{\partial x_j}-\overline{\rho}\epsilon+\frac{\partial}{\partial x_j}\left(\mu+\frac{\mu_t}{\sigma_{k'}}\frac{\partial k}{\partial x_j}\right)\right)=&\\-\overline{\rho u_i'' u_j''}C_{\epsilon 1}\frac{\omega}{k}\frac{\partial \widetilde{u_i}}{\partial x_j}-C_{\epsilon 2}\overline{\rho}\beta^*\omega^2+\frac{1}{k}\frac{\partial}{\partial x_j}\left(\left(\mu+\frac{\mu_t}{\sigma_\epsilon}\right)\left(k\frac{\partial \omega}{\partial x_j}+\omega\frac{\partial k}{\partial x_j}\right)\right).&\end{aligned} \tag{7.41}$$

For ϵ is $\beta^* k\omega$ substituted, and this new expression can be rewritten, which is done in the following steps

$$
\begin{aligned}
&\frac{\partial}{\partial t}(\overline{\rho}\omega) + \frac{\partial}{\partial x_j}(\overline{\rho}\widetilde{u_j}\omega) \\
&\quad = -\overline{\rho u_i'' u_j''}\frac{\omega}{k}(C_{\epsilon 1}-1)\frac{\partial \widetilde{u_i}}{\partial x_j} + \frac{\overline{\rho}\beta^* k\omega^2}{k} - \frac{\omega}{k}\frac{\partial}{\partial x_j}\left(\left(\mu + \frac{\mu_t}{\sigma_{k'}}\right)\frac{\partial k}{\partial x_j}\right) - C_{\epsilon 2}\overline{\rho}\beta^*\omega^2 \\
&\qquad + \frac{1}{k}\frac{\partial}{\partial x_j}\left(\mu k\frac{\partial \omega}{\partial x_j} + \mu\omega\frac{\partial k}{\partial x_j} + \frac{\mu_t}{\sigma_\epsilon}k\frac{\partial \omega}{\partial x_j} + \frac{\mu_t}{\sigma_\epsilon}\omega\frac{\partial k}{\partial x_j}\right) \\
&\quad = -\overline{\rho u_i'' u_j''}\frac{\omega}{k}(C_{\epsilon 1}-1)\frac{\partial \widetilde{u_i}}{\partial x_j} + \overline{\rho}\beta^*\omega^2 - C_{\epsilon 2}\overline{\rho}\beta^*\omega^2 - \frac{\omega}{k}\frac{\partial}{\partial x_j}\left(\left(\mu + \frac{\mu_t}{\sigma_{k'}}\right)\frac{\partial k}{\partial x_j}\right) \\
&\qquad + \frac{1}{k}\frac{\partial}{\partial x_j}\left(\left(\mu + \frac{\mu_t}{\sigma_\epsilon}\right)\omega\frac{\partial k}{\partial x_j}\right) + \frac{1}{k}\frac{\partial}{\partial x_j}\left(\left(\mu + \frac{\mu_t}{\sigma_\epsilon}\right)k\frac{\partial \omega}{\partial x_j}\right) \\
&\quad = -\overline{\rho u_i'' u_j''}\frac{\omega}{k}(C_{\epsilon 1}-1)\frac{\partial \widetilde{u_i}}{\partial x_j} - (C_{\epsilon 2}-1)\beta^*\overline{\rho}\omega^2 - \frac{\omega}{k}\frac{\partial}{\partial x_j}\left(\left(\mu + \frac{\mu_t}{\sigma_{k'}}\right)\frac{\partial k}{\partial x_j}\right) \\
&\qquad + \frac{\omega}{k}\frac{\partial}{\partial x_j}\left(\left(\mu + \frac{\mu_t}{\sigma_\epsilon}\right)\frac{\partial k}{\partial x_j}\right) + \frac{1}{k}\left(\mu + \frac{\mu_t}{\sigma_\epsilon}\right)\frac{\partial \omega}{\partial x_j}\frac{\partial k}{\partial x_j} \\
&\qquad + \frac{k}{k}\frac{\partial}{\partial x_j}\left(\left(\mu + \frac{\mu_t}{\sigma_\epsilon}\right)\frac{\partial \omega}{\partial x_j}\right) + \frac{1}{k}\left(\mu + \frac{\mu_t}{\sigma_\epsilon}\right)\frac{\partial k}{\partial x_j}\frac{\partial \omega}{\partial x_j} \\
&\quad = -\overline{\rho u_i'' u_j''}\frac{\omega}{k}(C_{\epsilon 1}-1)\frac{\partial \widetilde{u_i}}{\partial x_j} - (C_{\epsilon 2}-1)\beta^*\overline{\rho}\omega^2 + \frac{\omega}{k}\frac{\partial}{\partial x_j}\left(\left(\frac{\mu_t}{\sigma_\epsilon} - \frac{\mu_t}{\sigma_{k'}}\right)\frac{\partial k}{\partial x_j}\right) \\
&\qquad + \frac{2}{k}\left(\mu + \frac{\mu_t}{\sigma_\epsilon}\right)\frac{\partial \omega}{\partial x_j}\frac{\partial k}{\partial x_j} + \frac{\partial}{\partial x_j}\left(\left(\mu + \frac{\mu_t}{\sigma_\epsilon}\right)\frac{\partial \omega}{\partial x_j}\right)
\end{aligned}
\tag{7.42}
$$

The relation for the eddy viscosity (2.15) is $\mu_t = C_\mu \overline{\rho}\frac{k^2}{\epsilon}$. When $\epsilon = \beta^* k\omega$ is substituted and C_μ is defined as β^*, $\mu_t = \frac{\overline{\rho}k}{\omega}$ can be derived. Furthermore, the following new constants are defined: $\sigma_{\omega 2} \equiv \frac{1}{\sigma_\epsilon}$; $\sigma_{k2} \equiv \frac{1}{\sigma_{k'}}$; $(C_{\epsilon 1}-1) \equiv \gamma_2$; and $(C_{\epsilon 2}-1)\beta^* \equiv \beta_2$. Putting everything together results in the following relation

$$
\begin{aligned}
\frac{\partial}{\partial t}(\overline{\rho}\omega) + \frac{\partial}{\partial x_j}(\overline{\rho}\widetilde{u_j}\omega) = &-\overline{\rho u_i'' u_j''}\gamma_2\frac{\omega}{k}\frac{\partial \widetilde{u_i}}{\partial x_j} - \beta_2\overline{\rho}\omega^2 + \frac{\partial}{\partial x_j}\left((\mu + \sigma_{\omega 2}\mu_t)\frac{\partial \omega}{\partial x_j}\right) \\
&+ \frac{2}{k}\left(\mu + \frac{\overline{\rho}k}{\omega}\sigma_{\omega 2}\right)\frac{\partial k}{\partial x_j}\frac{\partial \omega}{\partial x_j} + \frac{\omega}{k}\frac{\partial}{\partial x_j}\left((\sigma_{\omega 2} - \sigma_{k2})\mu_t\frac{\partial k}{\partial x_j}\right).
\end{aligned}
\tag{7.43}
$$

7.3 Length shock cells

The shock cells are a result of a very fast expansion of the gas. For that reason the size of a shock cell depends on the pressure ratio. For a round jet the length of the first shock cell is calculated using (see (2.44))

$$\Delta_1 = 1.2\sqrt{\frac{p_0}{p_a} - 1.9}. \tag{7.44}$$

This relation is derived for a 3−dimensional case, so the length of the first shock cell for a 3−dimensional jet is proportional to $\sqrt{\frac{p_0}{p_a}}$. At the edge of the shock cells, the pressure of the expanded gas is equal to the pressure in the environment. During an expansion the pressure will drop as a function of distance, this is shown in Figure 7.1. In this figure we have some pressure p_0, which pushes to the fictional surface with radius r_0. When it expands, the pressure will drop as the ratio of 1 divided by the area of this increasing fictional surface. In the 3−dimensional case this surface has a spherical shape and the surface area is $A_{3D} = 4\pi r^2$, and in 2−dimensions this is a circle with surface area $A_{2D} = 2\pi r$. So we can say that the pressure drops as:

$$p(r) = \frac{p_0}{A}. \tag{7.45}$$

For a certain radius the pressure p becomes equal to p_a, which is the pressure far away from the expansion. This radius is proportional to the length of the first shock cell. For the 3−dimensional expansion, this results in

$$\frac{p_a}{p_0} \sim \frac{1}{r^2} \sim \frac{1}{\Delta_{1_{3D}}^2}, \tag{7.46}$$

or

$$\Delta_{1_{3D}} \sim \sqrt{\frac{p_0}{p_a}}. \tag{7.47}$$

This is the same proportionality as in (7.44). For the 2−dimensional case this results in

$$\frac{p_a}{p_0} \sim \frac{1}{r} \sim \frac{1}{\Delta_{1_{2D}}}, \tag{7.48}$$

or

$$\Delta_{1_{2D}} \sim \frac{p_0}{p_a}. \tag{7.49}$$

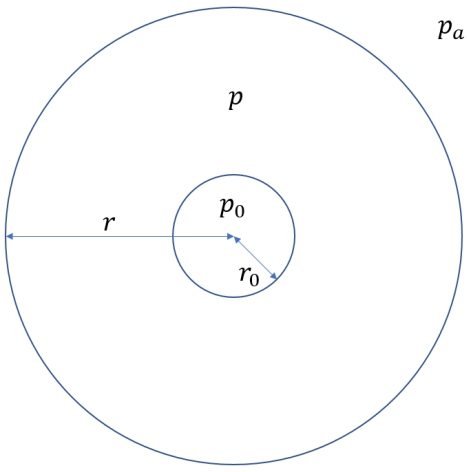

Figure 7.1: *Schematic of the pressure drop during the expansion of a gas from p_0 to p_a.*

7.4 Optimum pressure ratio

As derived in subsection 4.2.3, a Reynolds number that is proportional to the turbulence intensity can be expressed in terms of p_a, p_0, and γ. The relation was given by

$$Re \sim p_a \sqrt{\left(\frac{p_0}{p_a}\right)^{\frac{\gamma-1}{\gamma}} - 1}. \tag{7.50}$$

To find the value of p_a for a given value of p_0 that results in the maximum $Re-$number, the derivative of (7.50) with respect to p_a can be calculated and set equal to zero. The derivative is given by

$$\begin{aligned}\frac{\partial Re}{\partial p_a} &= \sqrt{\left(\frac{p_0}{p_a}\right)^{\frac{\gamma-1}{\gamma}} - 1} + \frac{1}{2} p_a \frac{1}{\sqrt{\left(\frac{p_0}{p_a}\right)^{\frac{\gamma-1}{\gamma}} - 1}} \left(\frac{\gamma-1}{\gamma}\right) \left(\frac{p_0}{p_a}\right)^{\left(\frac{\gamma-1}{\gamma}-1\right)} (-1) \frac{p_0}{p_a^2} \\ &= \sqrt{\left(\frac{p_0}{p_a}\right)^{\frac{\gamma-1}{\gamma}} - 1} - \frac{1}{2} \frac{\gamma-1}{\gamma} \left(\frac{p_0}{p_a}\right)^{\frac{\gamma-1}{\gamma}} \frac{1}{\sqrt{\left(\frac{p_0}{p_a}\right)^{\frac{\gamma-1}{\gamma}} - 1}}.\end{aligned} \tag{7.51}$$

When this expression is set to zero, the following derivation can be made

$$\begin{aligned}\sqrt{\left(\frac{p_0}{p_a}\right)^{\frac{\gamma-1}{\gamma}} - 1} &= \frac{1}{2} \frac{\gamma-1}{\gamma} \left(\frac{p_0}{p_a}\right)^{\frac{\gamma-1}{\gamma}} \frac{1}{\sqrt{\left(\frac{p_0}{p_a}\right)^{\frac{\gamma-1}{\gamma}} - 1}}, \\ \left(\frac{p_0}{p_a}\right)^{\frac{\gamma-1}{\gamma}} - 1 &= \frac{1}{2} \frac{\gamma-1}{\gamma} \left(\frac{p_0}{p_a}\right)^{\frac{\gamma-1}{\gamma}}, \\ \left(1 - \frac{1}{2} \frac{\gamma-1}{\gamma}\right) \left(\frac{p_0}{p_a}\right)^{\frac{\gamma-1}{\gamma}} &= 1, \\ \left(\frac{p_0}{p_a}\right)^{\frac{\gamma-1}{\gamma}} &= \frac{1}{1 - \frac{1}{2}\frac{\gamma-1}{\gamma}} = \frac{2\gamma}{\gamma+1}, \\ \frac{p_0}{p_a} &= \left(\frac{2\gamma}{\gamma+1}\right)^{\frac{\gamma}{\gamma-1}}, \\ p_a &= p_0 \left(\frac{\gamma+1}{2\gamma}\right)^{\frac{\gamma}{\gamma-1}}.\end{aligned} \tag{7.52}$$

7.5 Flow between parallel plates

In the first place it was expected that when a jet is injected in a very low pressure channel, it will expand and develop as a laminar or turbulent channel flow. For these two cases the exact flow profiles are derived in the next two subsections. However, the first simulations showed that the expanding jets do not result in a developed channel flow, so the profiles are not useful and presented here.

7.5.1 Laminar flow

A flow that is completely developed without a component in the z-direction and without variation in the x direction is analyzed, so $\frac{\partial}{\partial x} = \frac{\partial}{\partial z} = 0$. Furthermore, the density is constant, and thus (2.1) results in $\frac{\partial v}{\partial y} = 0$. This suggests that v is a constant, that should be zero because the walls are impermeable. Since v and w are zero, there is only one component that remains from (2.3), resulting in

$$-\frac{1}{\rho_0}\frac{\partial p}{\partial x} + \frac{\mu}{\rho_0}\frac{\partial^2 u}{\partial y^2} = 0. \tag{7.53}$$

Integrating (7.53) twice gives

$$u(y) = \frac{1}{2\mu}\frac{\partial p}{\partial x}y^2 + C_1 y + C_2. \tag{7.54}$$

Because of the low pressure flow, slip along the surfaces is present (see Figure 7.2). When adopting Maxwell slip as boundary conditions, this can be written as

$$y = 0 \ , \ u(0) = \frac{2-\sigma_T}{\sigma_T}\lambda\frac{\partial u}{\partial y}\bigg|_{y=0}, \tag{7.55a}$$

and

$$y = D \ , \ u(D) = -\frac{2-\sigma_T}{\sigma_T}\lambda\frac{\partial u}{\partial y}\bigg|_{y=D}, \tag{7.55b}$$

with $\frac{2-\sigma_T}{\sigma_T}\lambda = \delta$ the slip length, σ_T the tangential momentum accommodation factor, and λ the mean free path. Putting these boundary conditions in (7.54) results in the following flow profile

$$u(y) = \frac{1}{2\mu}\frac{\partial p}{\partial x}(y^2 - Dy - \delta D). \tag{7.56}$$

Preferably, the flow profile is written in terms of the flowrate Q, since this is easier to use as input. Integration of (7.56) over the domain is used to express $\frac{\partial p}{\partial x}$ in terms of Q. The resulting equation for the flow field is

$$u(y) = -\frac{6Q}{D^2(D+6\delta)}(y^2 - Dy - \delta D). \tag{7.57}$$

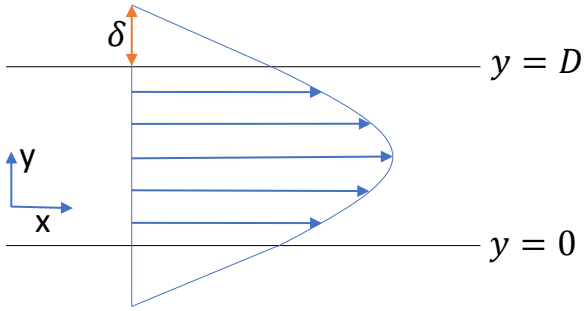

Figure 7.2: *Schematic picture of the flow profile of a flow between two plates with slip length δ, and a pressure gradient in the x-direction $\frac{\partial p}{\partial x}$.*

7.5.2 Turbulent flow

The flow between the parallel plates can be turbulent under specific conditions. In this subsection a homogeneous and completely developed turbulent flow is analyzed. First, a decomposed velocity and pressure field is introduced, according to $u_i = \overline{u_i} + u_i'$ and $p = \overline{p} + p'$, respectively. Here, the over-lined quantities are ensemble averages, while the primed quantities represent the fluctuations. Substituting these relations in (2.1) and (2.3), and keep the density constant, the averaged equations are

$$\overline{\frac{\partial(\overline{u_i} + u_i')}{\partial x_i}} = 0, \tag{7.58a}$$

and

$$\overline{\frac{\partial(\overline{u_i} + u_i')}{\partial t} + (\overline{u_j} + u_j')\frac{\partial(\overline{u_i} + u_i')}{\partial x_j}} = \overline{-\frac{1}{\rho_0}\frac{\partial(\overline{p} + p')}{\partial x_i} + \frac{\mu}{\rho_0}\frac{\partial^2(\overline{u_i} + u_i')}{\partial x_j^2}}. \tag{7.58b}$$

Using the Reynolds conditions as described in Nieuwstadt (2016), equation (7.58) can be simplified dramatically

$$\frac{\partial \overline{u_i}}{\partial x_i} = 0, \tag{7.59a}$$

and

$$\frac{\partial \overline{u_i}}{\partial t} + \overline{u_j}\frac{\partial \overline{u_i}}{\partial x_j} + \frac{\partial \overline{u_i' u_j'}}{\partial x_j} = -\frac{1}{\rho_0}\frac{\partial \overline{p}}{\partial x_i} + \frac{\mu}{\rho_0}\frac{\partial^2 \overline{u_i}}{\partial x_j^2}. \tag{7.59b}$$

The same assumptions as in section 7.5.1 are made for the averaged quantities. The $i = 1$ and $i = 2$ cases result in

$$0 = -\frac{1}{\rho_0}\frac{\partial \overline{p}}{\partial x} + \frac{\mu}{\rho_0}\frac{\partial^2 \overline{u}}{\partial y^2} - \frac{\partial \overline{u'v'}}{\partial y} = -\frac{1}{\rho_0}\frac{\partial \overline{p}}{\partial x} + \frac{\partial}{\partial y}\left(\nu\frac{\partial \overline{u}}{\partial y} - \overline{u'v'}\right), \tag{7.60a}$$

and

$$0 = -\frac{1}{\rho_0}\frac{\partial \overline{p}}{\partial y} - \frac{\partial \overline{v'^2}}{\partial y}, \tag{7.60b}$$

with ν the kinematic viscosity. (7.60b) shows that the pressure is only depended on x. The term between the curvy brackets in (7.60a) is called the shear stress τ_t. The boundary conditions for this situation are

$$y = 0 \ , \ \overline{u} = \delta\frac{\partial \overline{u}}{\partial y}\bigg|_{y=0}, \tag{7.61a}$$

and

$$y = \frac{D}{2} \ , \ \tau_t = 0. \tag{7.61b}$$

Solving (7.60a) for τ_t and using (7.61b) results in

$$\tau_t = \frac{1}{\rho_0}\frac{\partial \overline{p}}{\partial x}\left(y - \frac{D}{2}\right). \tag{7.62}$$

This will be rewritten using the friction velocity u_*, for which the following relations hold

$$u_*^2 = \frac{\tau_s}{\rho_0} = \tau_t(0) = -\frac{D}{2\rho_0}\frac{\partial \overline{p}}{\partial x}. \tag{7.63}$$

In other words, (7.60a) can be written as

$$\nu\frac{\partial \overline{u}}{\partial y} - \overline{u'v'} = u_*^2\left(1 - \frac{2y}{D}\right). \tag{7.64}$$

To solve this we need an expression for the second term on the left-hand side of (7.64). This is the so called closure problem. A solution of this problem was proposed by Joseph Valentin Boussinesq (see (Schlichting et al., 1980)) by adopting the assumption

$$-\overline{u'v'} = \nu_t\frac{\partial \overline{u}}{\partial y}. \tag{7.65}$$

Now three different regimes can be distinguished: the *core*, the *wall layer* and the *viscous layer*. For the *core* and the area relatively close to the surfaces, the viscous term (first term on left-hand side of (7.64)) can be neglected, since the Reynolds stress is dominant. In the *core* the eddy viscosity is proportional to the diameter of the channel, $\nu_t = \beta^2 D^2|\frac{\partial \overline{u}}{\partial y}|$ in which β is a constant. Solving (7.64) using this eddy viscosity gives

$$\overline{u}(y) = u_{cl} - \frac{1}{3}\frac{u_*}{\beta}\left(1 - \frac{2y}{R}\right)^{3/2}, \tag{7.66}$$

where u_{cl} is the averaged center line velocity. In the area closer to the surface the eddies are shrinking, and the eddy viscosity is described using the Von-Kármán constant κ and becomes $\nu_t = \kappa^2 y^2|\frac{\partial \overline{u}}{\partial y}|$ (see (Schlichting et al., 1980)). Since y becomes small the only term on the right-hand side of (7.64) that is important is u_*^2. Take all of this into account results in the following flow profile in the wall area

$$\overline{u}(y) = \frac{u_*}{\kappa}\ln\left(\frac{y}{y_0}\right), \tag{7.67}$$

where y_0 is a constant. Very close to the wall the viscous term of (7.64) is dominant over the Reynolds stress term. y is even smaller here, so on the right-hand side of (7.64) u_* is dominant again. Solving (7.64) for these assumptions results in

$$\overline{u}(y) = \frac{u_*^2}{\nu}y + C_3, \tag{7.68}$$

where C_3 can be determined using the slip condition on the wall (7.61a). The result can be rewritten in terms of a pressure gradient and yields

$$\overline{u}(y) = \frac{u_*^2}{\nu}(y + \delta) = -\frac{D}{2\mu}\frac{\partial \overline{p}}{\partial x}(y + \delta). \tag{7.69}$$

To link (7.69) with (7.67), it is found in literature (see Nieuwstadt (2016)) that we should couple them at $y = 11\frac{\nu}{u_*}$, so the following relation holds

$$\frac{u_*^2}{\nu}\left(11\frac{\nu}{u_*} + \delta\right) = \frac{u_*}{\kappa}\ln\left(\frac{11\nu}{u_* y_0}\right). \tag{7.70}$$

This can be solved for y_0 and the result is substituted in (7.67). Rewritten in terms of the pressure gradient, the result is

$$\overline{u} = \left(\frac{1}{2\kappa}\ln\left(-\frac{\rho_0 D}{2\kappa^2\mu^2}\frac{\partial \overline{p}}{\partial x}y^2\right) + 11\right)\sqrt{-\frac{D}{2\rho_0}\frac{\partial \overline{p}}{\partial x}} - \frac{\delta D}{2\mu}\frac{\partial \overline{p}}{\partial x}. \tag{7.71}$$

This profile should be matched somewhere with the core region. This is normally done at $y = \alpha D$, where α is a new constant. Solving the new relation will result in a large expression for u_{cl}, which contains two unknown constants. Since this report focuses on particle release from the surface it is not necessary to describe the core region. The important part is that we can describe the averaged flow profile for $y < 11\frac{\nu}{u_*}$ with (7.69) and for $y > 11\frac{\nu}{u_*}$ with (7.71).

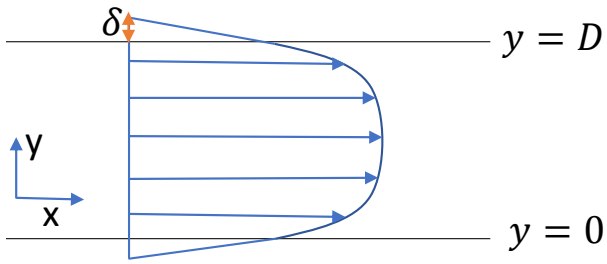

Figure 7.3: *Schematic averaged turbulent flow profile of a flow between two plates with slip length δ, and an average pressure gradient in the x-direction $\frac{\partial \overline{p}}{\partial x}$.*

7.6 Adhesion force simple cases

In the present study we are interested in the flushing process of very small particles in a dry environment. The adhesion will then be dominated by the inter-molecular forces. The particles do not carry any electrical charge, so the Van der Waals force is the dominant force. The Van der Waals potential between two atoms or small molecules at distance r is described by

$$E(r) = -\frac{C}{r^6}, \tag{7.72}$$

with C the London-Van der Waals constant.

To derive expressions for the adhesion force, two simple geometries are used, a sphere-wall interaction and a sphere-sphere interaction, combinations of these two cases can describe more complex geometries.

7.6.1 Sphere-wall interaction energy

In this subsection the interaction energy between a sphere and a wall (see figure 7.4) will be calculated. The wall is assumed to be an infinite half space. To start the analysis the influence of the wall at distance D from the wall will be calculated. The integral for the potential energy of a molecule at distance D from a half space is given by

$$E(D) = -2\pi C\rho_1 \int_{z=D}^{z=\infty}\int_{r=0}^{r=\infty} \frac{r}{(z^2+r^2)^3} dr dz = -\frac{\pi C\rho_1}{6D^3}, \tag{7.73}$$

with ρ_x the atom density of material x. This expression is used to integrate over the volume of the sphere, the sphere is divided into thin slices, one is shown in Figure 1.4b. This integration, in combination with the assumption that $D \ll R$, results in the following interaction energy between sphere and wall

$$E(D) = -\frac{\pi C\rho_1}{6}\int_0^{2R} \frac{\pi\rho_2 (r(2))^2 dz}{(D+z)^2} = -\frac{\pi^2 C\rho_1\rho_2 R}{6D}. \tag{7.74}$$

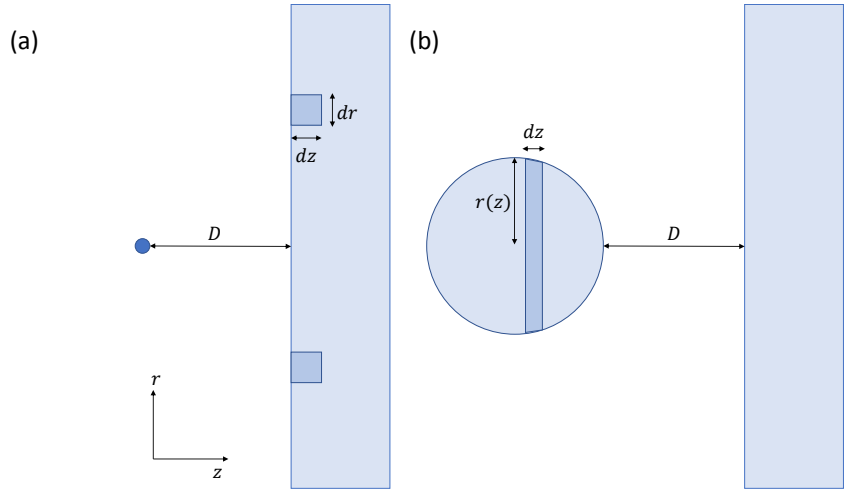

Figure 7.4: *Schematic drawings: (a) illustrates how the integration over the half space is performed; (b) illustrates the integration over the sphere.*

7.6.2 Sphere-sphere interaction energy

The same procedure as in subsection 7.6.1 can be carried out for the sphere-sphere interaction. First, the influence of the sphere at a point at distance L from the centre of the sphere with radius R_1 is calculated as

$$E(L) = -\int_{L-R_1}^{L+R_1} \frac{C\rho_1}{r^6} A(r)dr, \tag{7.75}$$

where $A(r)$ is the surface area at distance r from the point within the sphere. For more information on this analysis, the reader is referred to (Hamaker, 1937). This relation is used to perform the integration of sphere 2 with radius R_2 at closest distance d, resulting in

$$E(D) = \int_{d-R_2}^{d+R_2} E(L)\rho_2 B(L)dL = -\int_{d-R_2}^{d+R_2} \left(\int_{L-R_1}^{L+R_1} \frac{C\rho_1}{r^6} A(r)dr \right) \rho_2 B(L)dL, \tag{7.76}$$

where $B(l)$ is the area at distance L from the centre of sphere 1 inside sphere 2, and $d = R_1 + R_2 + D$. Assuming that the distance between the spheres is much smaller than their radii, the integral can be solved (see (Hamaker, 1937)) and the result is:

$$E(D) = -\frac{\pi^2 C\rho_1\rho_2}{6D} \left(\frac{R_1 R_2}{R_1 + R_2} \right). \tag{7.77}$$

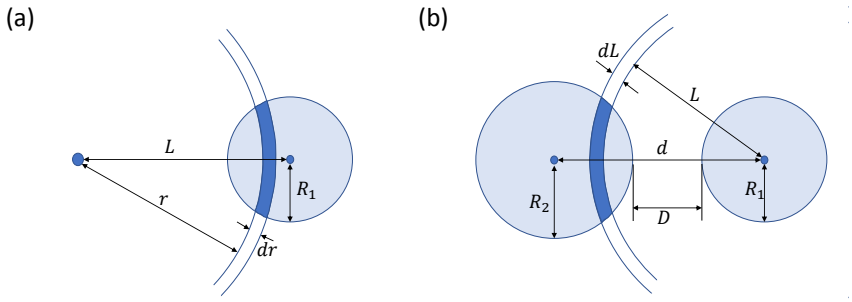

Figure 7.5: *Schematic drawing: (a) illustrates how the integration over the right sphere is carried out. (b) illustrates the integration over the left sphere.*

To derive an expression for the adhesion force, first an expression for the force is needed, which is

$$F = -\frac{dE}{dD}. \tag{7.78}$$

From (7.74) and (7.77), it then follows that

$$F_{sphere,wall}(D) = -\frac{\pi^2 C\rho_1\rho_2 R}{6D^2} = -\frac{AR}{6D^2}, \tag{7.79}$$

and

$$F_{sphere,sphere}(D) = -\frac{\pi^2 C\rho_1\rho_2}{6D^2} \left(\frac{R_1 R_2}{R_1 + R_2} \right) = -\frac{A}{6D^2} \left(\frac{R_1 R_2}{R_1 + R_2} \right), \tag{7.80}$$

where A is the Hamaker constant, which is constant for a specific sphere-wall combination, depending on the atom densities of these materials. The attractive behaviour of this force results in the minus sign in front of the relation. As the analysis concerns the adhesive force, the minus sign will be dropped.

7.7 Additional results

In the following subsections some additional results are presented that are used to make the explanations in chapter 4 more understandable. In subsection 7.7.1 the local Reynolds values are presented for three different simulations. In the captions of the figures the relevant parameters of the simulations are mentioned. In subsection 7.7.2 the comparison between the laminar, the $k-\epsilon$, and the $k-\omega$ simulations for three different cases is discussed. The specific cases are described in the captions. Subsections 7.7.3, 7.7.4, and 7.7.5 present the laminar flow fields on a certain timestep, the channel Knudsen number (Kn), and the turbulent kinetic energy. In the captions more information about the simulation results is presented. Note that in all figures below the flowrate is f_{high}.

7.7.1 Reynolds value

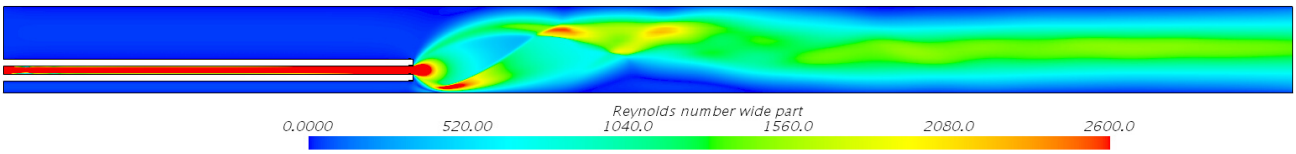

Figure 7.6: *Graphical representation of the local Reynolds value for p_{low} and f_{high} (Laminar model). This Re-value is calculated using local quantities and the width of the channel.*

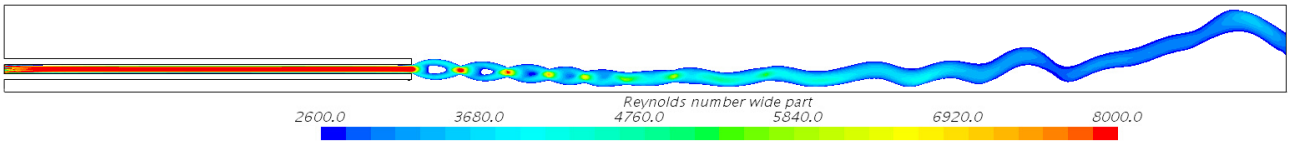

Figure 7.7: *Graphical representation of the local Reynolds value for p_{high} and f_{high} (Laminar model). This Re-value is calculated using local quantities and the width of the channel.*

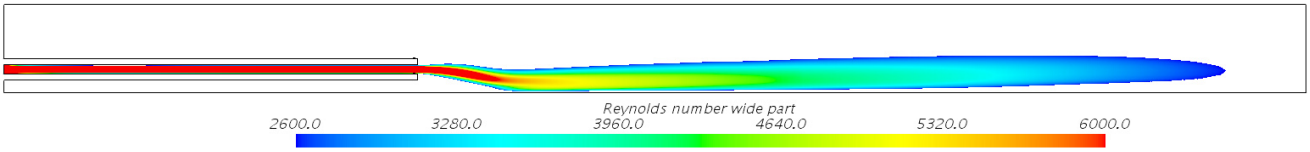

Figure 7.8: *Graphical representation of the local Reynolds value for* 5000 Pa *and f_{high} ($k-\epsilon$ model). This Re-value is calculated using local quantities and the width of the channel.*

7.7.2 Comparison models

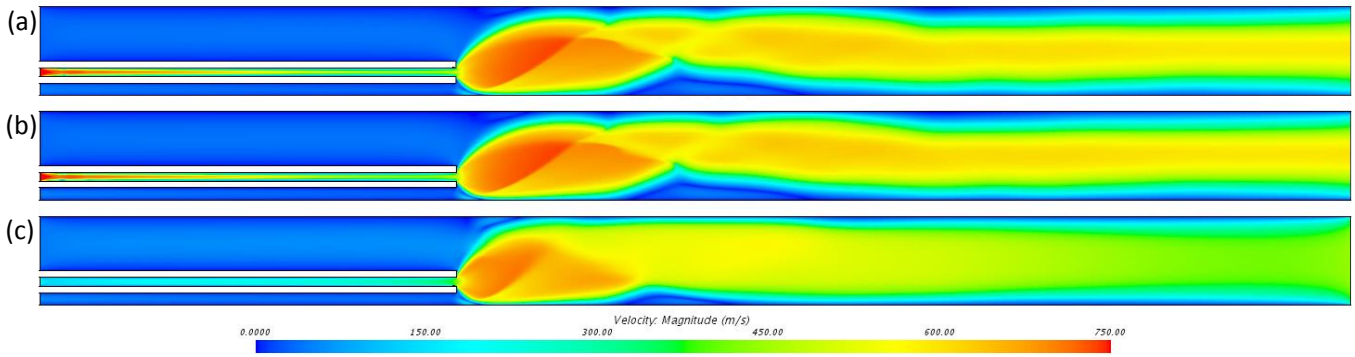

Figure 7.9: *Graphical representation of the spatial distribution of the absolute velocity magnitude for p_{low} simulated with: steady laminar model (a), $k-\omega$ model (b), and $k-\epsilon$ model (c).*

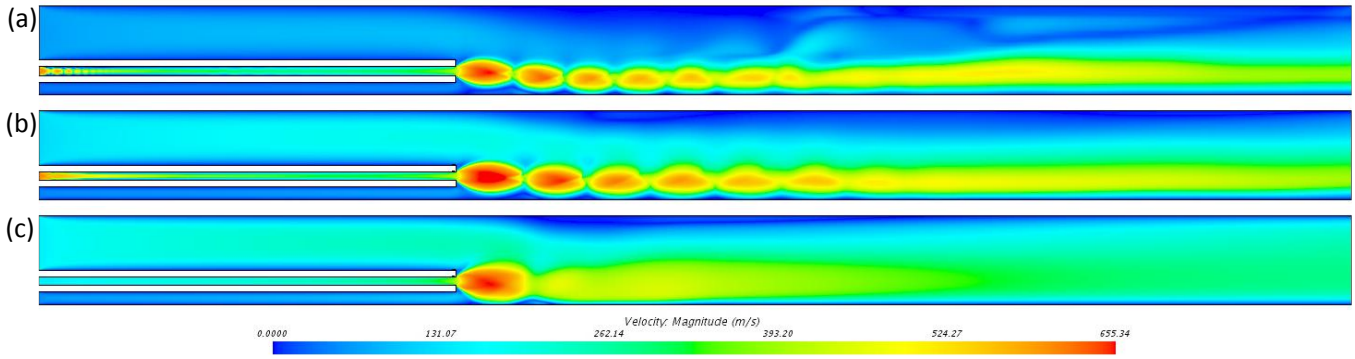

Figure 7.10: *Graphical representation of the spatial distribution of the absolute velocity magnitude for* 800 Pa *simulated with: steady laminar model (a), $k-\omega$ model (b), and $k-\epsilon$ model (c).*

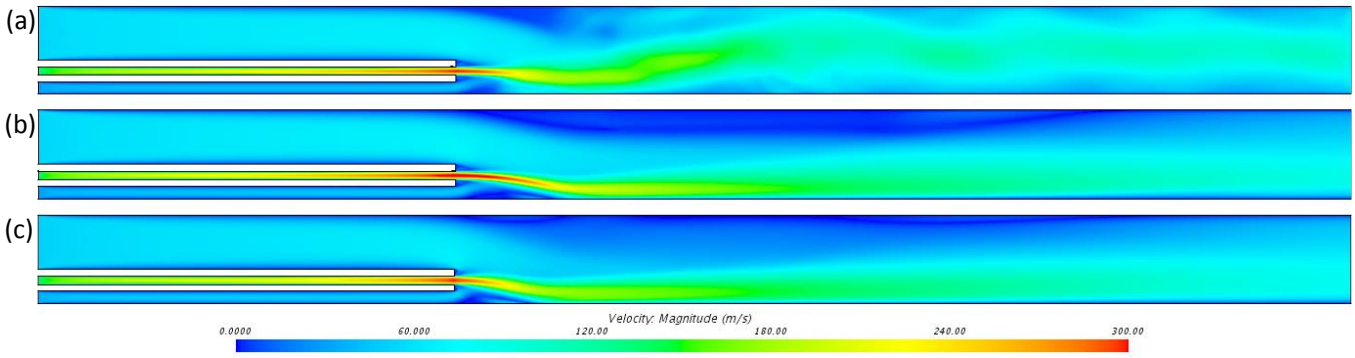

Figure 7.11: *Graphical representation of the spatial distribution of the absolute velocity magnitude for* 5000 Pa *simulated with: averaged transient laminar model (a), $k-\omega$ model (b), and $k-\epsilon$ model (c).*

7.7.3 Wavy velocity profile

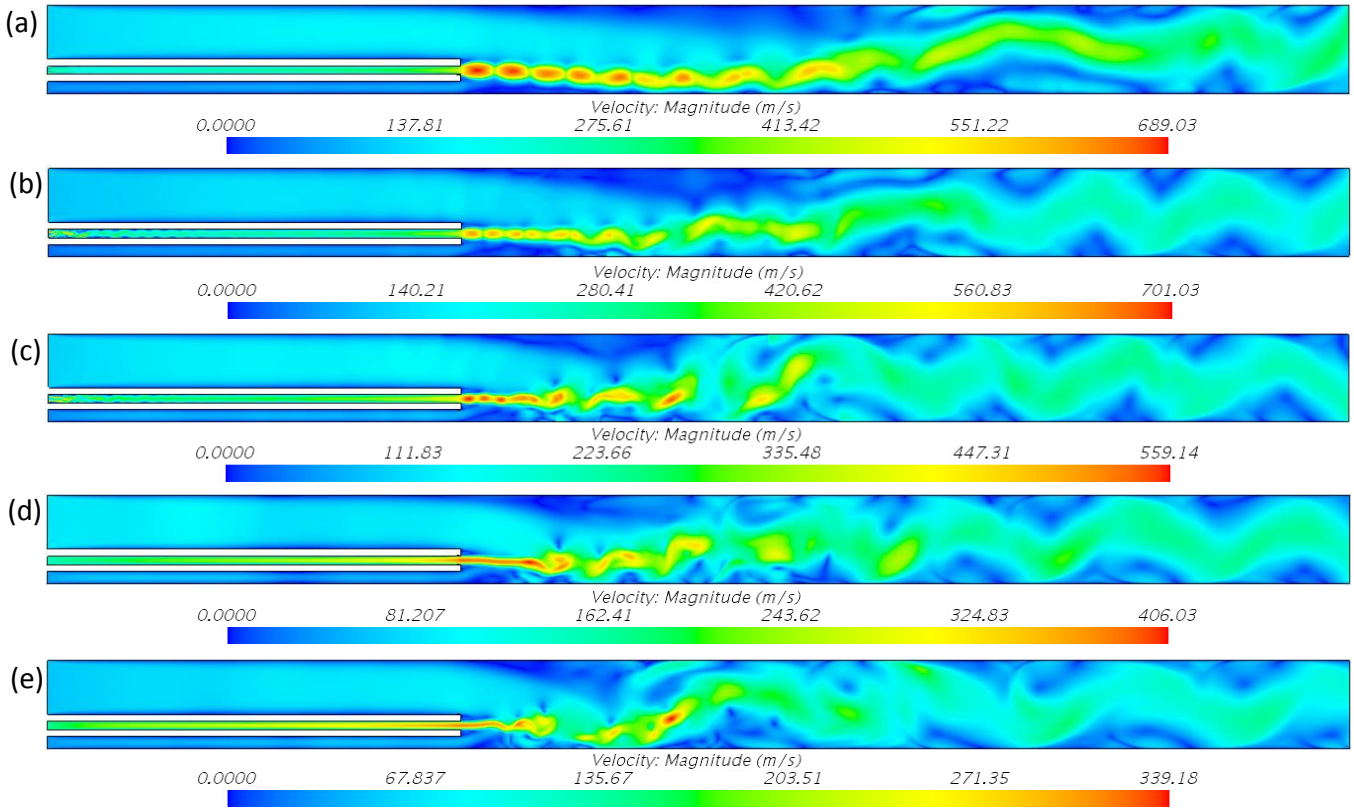

Figure 7.12: *Graphical representation of the spatial distribution of the absolute velocity magnitude at random time for laminar transient simulations. For* 1500 Pa *(a),* 2000 Pa *(b),* 2500 Pa *(c),* 3500 Pa *(d), and* 5000 Pa *(e).*

7.7.4 Channel Knudsen number

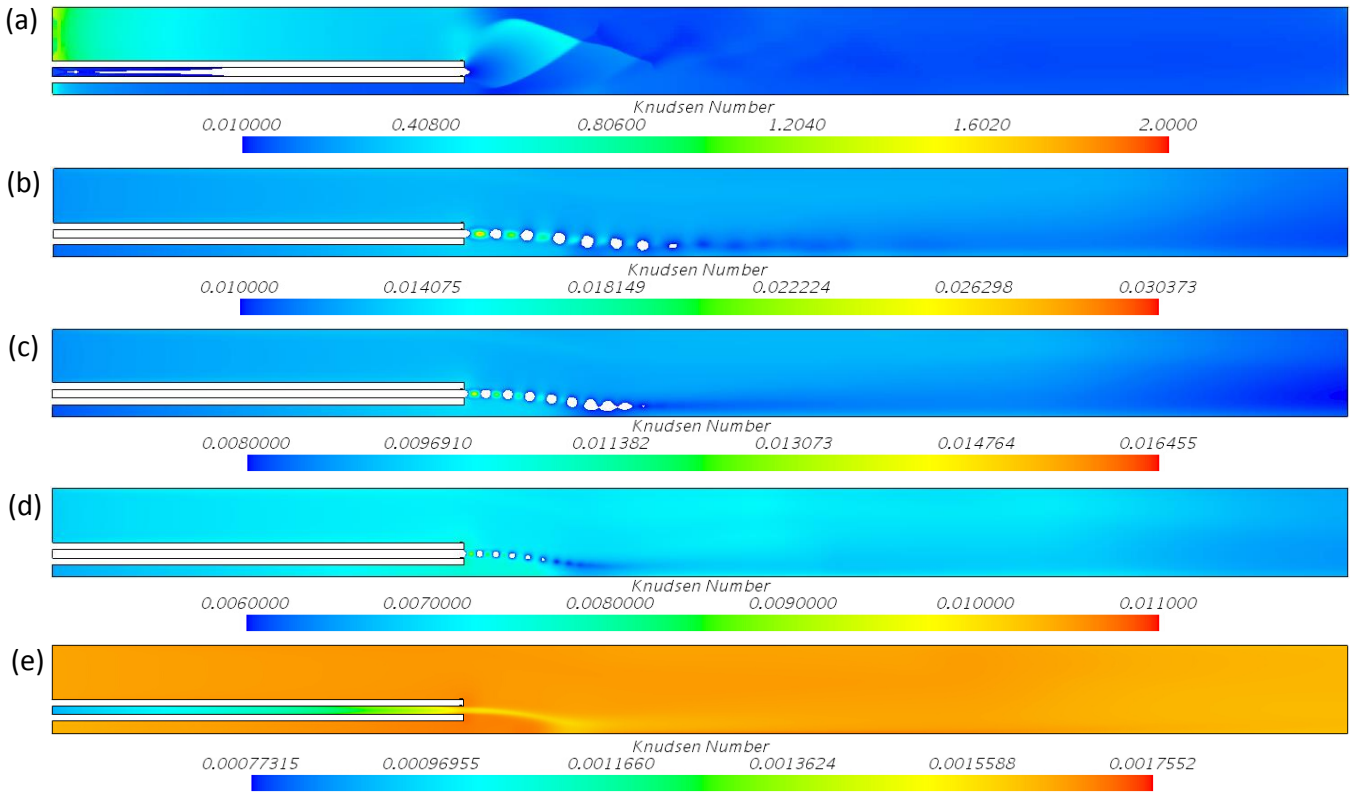

Figure 7.13: *Graphical representation of the spatial distribution of the Knudsen number calculated using the half of the channel width. Simulations were performed using the* $k-\omega$ *model for* 10 Pa *(a),* 1500 Pa *(b),* 2000 Pa *(c),* 2500 Pa *(d), and* 5000 Pa *(e).*

7.7.5 Turbulent kinetic energy

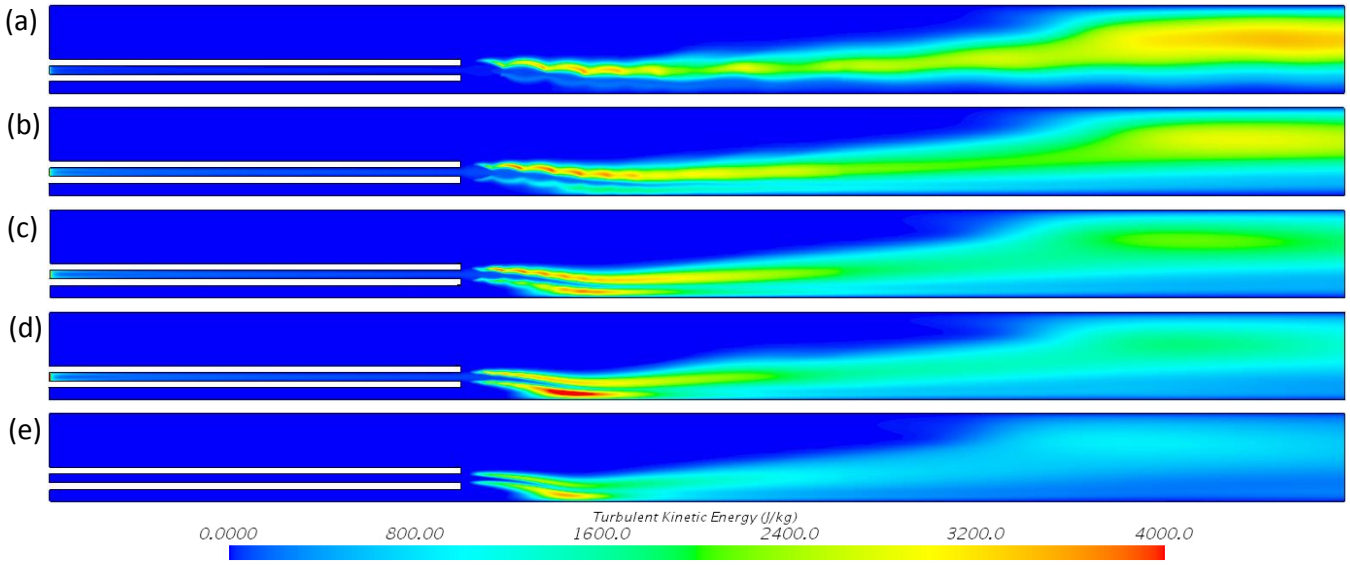

Figure 7.14: *Graphical representation of the spatial distribution of the turbulent kinetic energy. Simulations were performed using the* $k-\omega$ *model for* p_{high} *(a),* 1500 Pa *(b),* 2000 Pa *(c),* 2500 Pa *(d), and* 3500 Pa *(e).*

7.7.6 Additional figures

This subsection presents some additional figures. The results shown in Figure 7.15 provide support that a 2−dimensional approach is reasonable in the area of interest. Figure 7.16 shows an example of the drag forces found in a laminar simulation. This figure is used to explain the large fluctuations for the laminar lower background pressure simulations. Figure 7.17 presents an experimental result in terms of particles found during flushing experiments for different pressures. In this small pressure regime a same trend is found as in the simulations. Figure 7.18 shows the Cunningham correction factor as a function of the Knudsen number. Furthermore, this graph shows two simplifications.

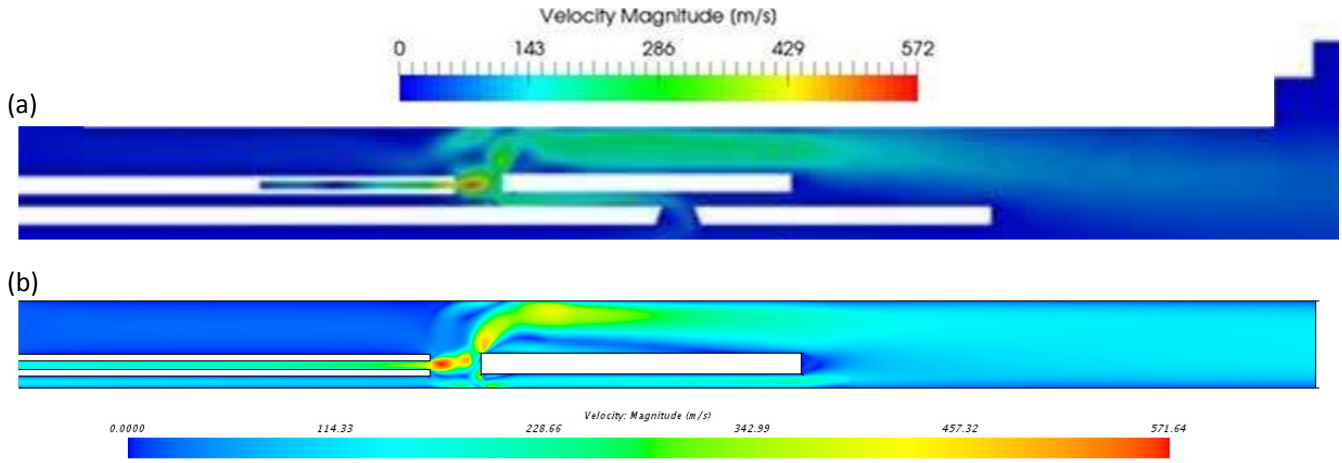

Figure 7.15: *Graphical representation of the spatial distribution of the velocity field for a flowrate of* f_{high} *and a background pressure of* p_{high}*, using: a three dimensional model in Fluent (a) and the two dimensional simplified model in StarCCM+ (b).*

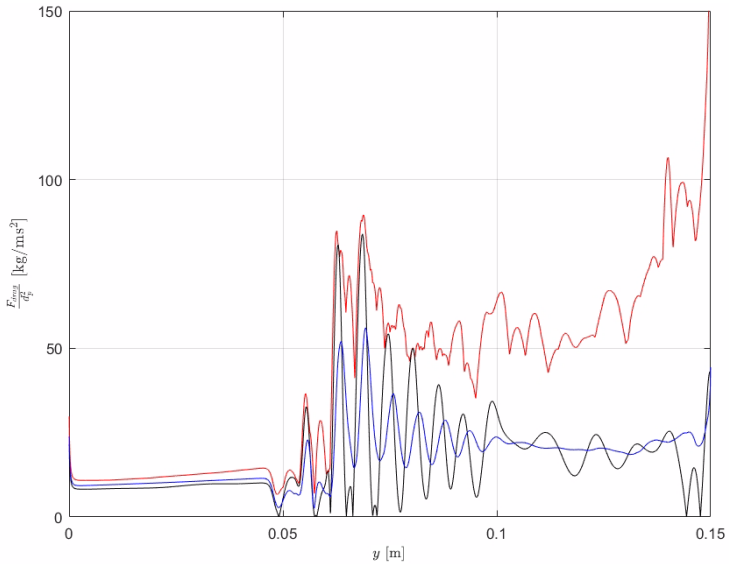

Figure 7.16: *Drag Force on contaminated surface calculated using laminar solver, for 800 Pa. The average (blue line), the maximum value (red), and the values on a certain time step (black)*

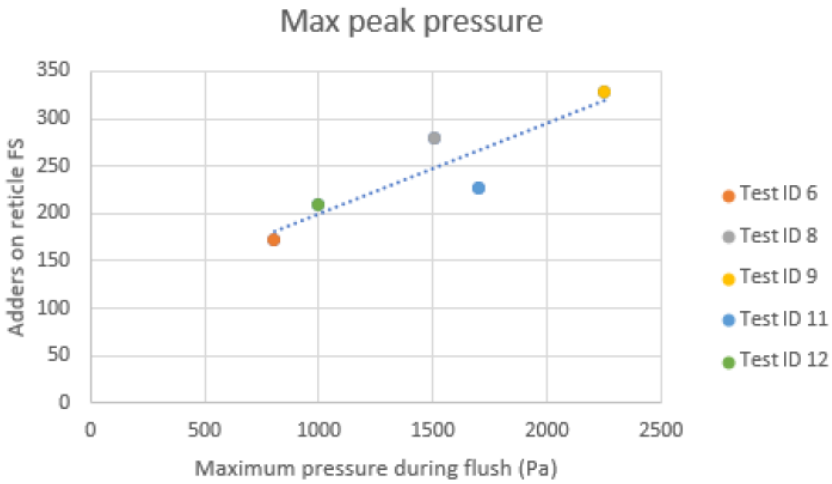

Figure 7.17: *Graph showing the amount of particles (adders) on the reticle after a flush (measure of flush performance) for different pressures.*

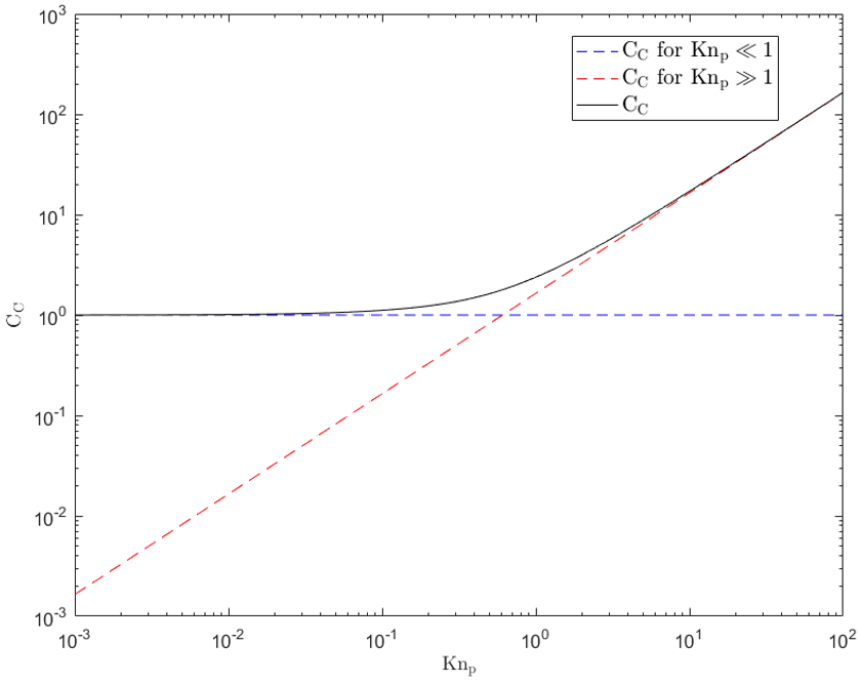

Figure 7.18: *Graph showing approximations of* $C_C = 1 + Kn_p(a + be^{\frac{c}{Kn_p}})$ *for the case that* $Kn_p \ll 1$*, resulting in* $C_C = 1$*, and* $Kn_p \gg 1$*, resulting in* $C_C = Kn_p(a + b)$*.*